Atomistic Simulations of Barium Titanate

Thesis by

Qingsong Zhang

In Partial Fulfillment of the Requirements

for the Degree of

Doctor of Philosophy

California Institute of Technology

Pasadena, California

2004

(Defended Sept. 30, 2004)

To Xin and Julia

Acknowledgements

First and foremost I wish to thank my adviser, William A. Goddard III. Bill combines the tremendous experience, insight and energy of an outstanding scientist with the wisdom and patience of a great adviser, and I have benefited enormously from his guidance. For that I am truly grateful.

I also wish to thank my colleagues in Materials and Processes Simulation Center at Caltech: Tahir Cagin for the discussion on this project and his help on molecular dynamics; Darryl L. Willick, who makes all my work possible by maintaining the computer system in perfect conditions; Shiang-Tai Lin for helpful discussion on the velocity autocorrelation method and helping me use his code; Mustafa Uludogan, who has supported my work with the *ab initio* calculations on $BaTiO_3$;...

I am indebted to some of my friends at Caltech: Yue Qi, who introduced me to this group; Guofeng Wang for giving me various suggestions when I started my study at Caltech; Weiqiao Deng for great scientific ideas; Qing Zhang for proofreading the manuscript; Jiao Lin, Jian Wu, Lan Yang and Tao Feng for friendship at Caltech.

I wish to extend warm thanks to my parents, Liangjin Zhang and Lingzhen Ke, for their support and encourage.

My warmest thanks to my wife, Xin Chen. Without her understanding and support, this endeavor would not be possible. To my lovely daughter, Julia, for bringing a lot of fun to my research.

Abstract

We present the Polarizable Charge Equilibration (P-QEq) force field to include self-consistent atomic polarization and charge transfer in molecular dynamics of materials. The short-range Pauli repulsion effects are described by two body potentials without exclusions. A linear self-consistent field solution to the charge transfer is proposed for charge transfer in large systems. The P-QEq is parameterized for $BaTiO_3$ based on quantum mechanics calculations (DFT with GGA) and applied to the study of the phase transitions, domain walls and oxygen vacancies.

Frozen phonon analysis reveals that the three high-temperature $BaTiO_3$ phases in the displacive model are unstable. Within their corresponding macroscopic phase symmetries, the smallest stable phase structures are achieved by antiferroelectric distortions from unstable phonons at the Brillouin zone boundaries. The antiferroelectric distortions soften phonons, reduce zero point energies and increase vibrational entropies. A correct $BaTiO_3$ phase transition sequence and comparable transition temperatures are obtained by free energy calculations. The inelastic coherent scattering functions of these phases agree with X-ray diffraction experiments.

$BaTiO_3$ 180° domain wall is Ba-centered with abrupt polarization switching across the wall. The center of $BaTiO_3$ 90° domain wall is close to its orthogonal phase. There are transition layers from the wall centers to the internal domains in the types of domain walls. Polarization variation in these transition layers induces polarization charge and free charge transfer. This effect causes a strong bipolar electric field in $BaTiO_3$ 90° domain wall.

Oxygen vacancies are frozen at room temperature, and mobile near the Curie temperature. In the tetragonal phase, the broken Ti-O chains are frozen, reducing switchable polarization. Due to charge redistribution and local relaxation, oxygen vacancy interaction is short-range and anisotropic. Two oxygen vacancies can form a stable pair state, where two broken $Ti - O$ chains are aligned parallel. Oxygen vacancy clusters can form dendritic structures as a result of local relaxation and charge interaction.

Contents

List of Figures

List of Tables

Chapter 1

Introduction

This thesis describes in detail the study of ferroelectrics I have pursued as a graduate student at California Institute of Technology. Since ferroelectrics phenomenon is related to small energy change (meV), large size (thousands to millions of atoms) and long correlation time, direct application of the first-principles calculations is not feasible. Hence, I first developed a quantum mechanics based force field (P-QEq), which has a self-consistent description of the electronic polarization and charge transfer while retaining a simple mathematical form. Then, I applied this P-QEq force field to study various phenomena in a well-known ferroelectric perovskite, $BaTiO_3$. In particular, I studied the phase structures and transitions, domain walls, and oxygen vacancies.

1.1 Ferroelectrics and $BaTiO_3$

Ferroelectricity is an example of cooperative phenomena. In a ferroelectric crystal, due to the inversion symmetry break there is an electric dipole moment even in the absence of an external electric field. Because of this spontaneous polarization and its coupling with stress and electric field, ferroelectrics has three main technological applications: data storage, transducers and capacitors.

Among them, barium titanate ($BaTiO_3$) is a well-known system. Because of its

high relative permittivity, this compound has become one of the most important materials in the electronics industry. Recently, it has been extensively studied particularly for its application as a capacitor material in dynamic random access memory (DRAM) devices. In addition to these technological aspects, $BaTiO_3$ has also attracted much attention from the standpoint of solid-state physics and chemistry. Since this compound has a simple common perovskite structure and shows successive phase transitions, the relationship between the crystal structure and ferroelectricity has become a major subject of research.

$BaTiO_3$ goes through a series of phase transitions with increasing temperature: rhombohedral (R, ferroelectric, Fig. 1.1a), orthorhombic (O, ferroelectric, Fig. 1.1b), tetragonal (T, ferroelectric, Fig. 1.1c) and cubic (C, paraelectric, Fig. 1.1d). The macroscopic polar axes of the three low-temperature ferroelectric phases align along the $\langle 111 \rangle$, $\langle 110 \rangle$ and $\langle 100 \rangle$ directions respectively. These transitions occur at 183 from R to O, 278K from O to T, and 393 K from T to C. Each transition is accompanied with small atomic displacements, latent heats and macroscopic strains. Experimental latent heats of these transitions [68] are 8 ± 2, 22 ± 4, and 55 ± 5 cal/mol, or 0.3, 0.9 and 2.2 meV.

1.2 Origin of Ferroelectrics

In the ferroelectric state, the inversion symmetry is broken. The origin of ferroelectrics is related to their electronic structures. A well-known reason for the distortion of a symmetric configuration of a system is the Jahn-Teller effect [39],

> any non-linear molecular system in a degenerate electronic state will be unstable and will undergo distortion to form a system of lower symmetry and lower energy thereby removing the degeneracy.

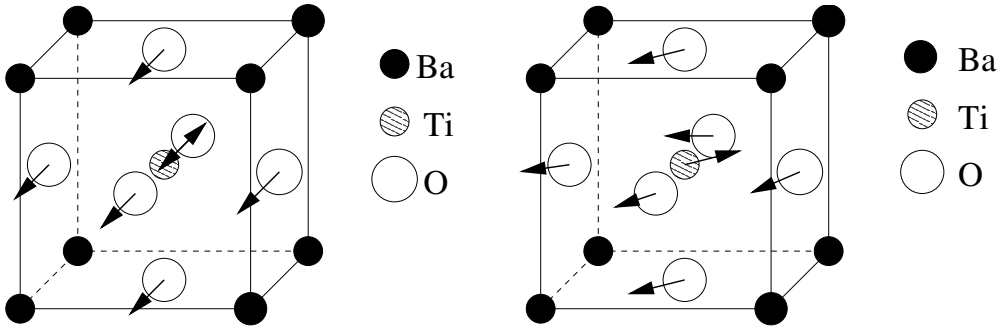

(a) Rhombohedral.

(b) orthorhombic.

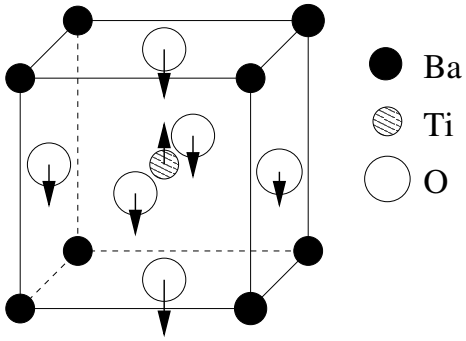

(c) tetragonal.

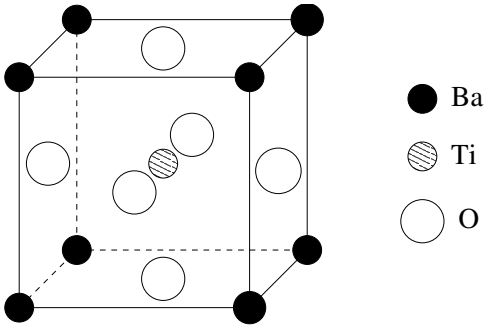

(d) cubic.

Figure 1.1: $BaTiO_3$ Phase structures in the displacive model.

In a crystal, such effects can give quite strong interactions between the filled and empty bands. A detailed theoretical explanation of instability of $BaTiO_3$ was given by Bersuker [4, 5] and a numeric calculation within density functional theory (DFT) with local density approximation (LDA) was given by Cohen [13].

Phase instability is related to unstable modes in the frozen phonon structure. The phonon structure of $BaTiO_3$ cubic phase was studied with DFT/LDA in the last decade. Among them, Zhong *et al.* [80] found giant LO-TO splitting in a series of ABO_3 cubic perovskite compounds. Lattice dynamics studies show a two-dimensional character in the Brillouin zone in the cubic phases of $BaTiO_3$ [27, 71] and $KNbO_3$ [79]. These calculations showed that there are unstable phonons in the $BaTiO_3$ cubic phase in the displacive model.

However a cubic phase structure with a stable phonon structure has not been reported. The arguments of displacive mechanism vs. order-disorder mechanism have lasted for decades.

In this thesis, a systematic study of the phonon structures of all the four phases is carried out. With the analysis of the phonon structures, the local structures within their corresponding macroscopic symmetries are obtained.

1.3 Charge Transfer and Electronic Polarization

To describe the ferroelectrics, two quantum mechanical effects must be considered in the atomistic methods: charge transfer and electronic polarization.

Charge transfer is based on the electronegativity equalization of all atoms in a system. The basic concept is that each element has an intrinsic electronegativity of its own state plus a term from atomic interaction. The electrostatic energy reaches its minimum when its first derivatives *w.r.t.* each charge variable (we call it electronegativity) equal to each other. There are two main schemes which have been used in

the literature for calculating charges in this way, the Electronegativity Equalization Method (EEM) [73] and the Charge Equilibration (QEq) [62] approach. The basic difference between the two schemes is that in EEM Coulomb interaction takes the unshielded $\frac{1}{r}$ form, whereas in QEq these terms are calculated as the integral over two s-type Slater orbitals.

The unshielded EEM gives too large interaction in crystals when atoms are too close. QEq is slower than EEM because of its Slater type orbital integration. In widely available codes, a simpler version of QEq is implemented. Namely, rigorous Slater type orbitals are used for charge calculation and then unshielded interaction of $\frac{1}{r}$ form is used to evaluated energy and its derivatives. The inconsistency makes errors which can not be used in ferroelectrics, because the phase energy difference is much smaller than such errors. Further, computations of original EEM and QEq scale as N^3, which are inefficient in large scale MD calculation.

Electronic polarization is usually described by a shell model in force field. In the shell model, each atom is partitioned into a positive point charge (core) and a negative point charge (shell). Electrical attraction within each atom is then replaced by a spring constant to avoid the collapse between the core and shell.

In this study a feasible self-consistent description of the charge transfer and electronic polarization effects is proposed and developed. The details are described in Chapter 2.

1.4 Displacive, Order-Disorder, or Something Else

There are two canonical models commonly used to describe the structural phase transitions observed in $BaTiO_3$, the displacive transition and the order-disorder transition (Fig. 1.2). In a displacive transition, the potential surface in which the atoms rest changes with increasing temperature. At low temperature, the atoms populate a po-

tential minimum which is displaced from a point of centrosymmety. At high temperature, the potential minimum is the center of a centrosymmetry. In the order-disorder model, the shape of the potential surface remains unchanged with temperature. As the temperature is raised, the hopping rate between adjacent minima in the potential surface increases, leading to a disordered structure. In the high temperature phase, the hopping rate is so high that the equivalent sites are equally populated.

For $BaTiO_3$, early research regards its transition as a displacive type [11]. This is supported by the observed soft mode in the cubic phase [51]. However, this soft mode is overdamped and does not vanish at the transition point. An eight-site model was first proposed by Bersuker [4, 5] with his electronic structure analysis. It was then reformed with the chain concept by Comes [15] to explain the diffuse X-ray diffraction pattern. However, Huller later [37] showed that a displacive model with dynamic phonon correlation in $BaTiO_3$ can also explain these scattering experiments.

Since then the arguments continue. But more and more experiments revealed that the local structure of $BaTiO_3$cubic phase is polar. Among them are infrared reflectivity measurements [26], X-ray absorption fine structure [63], and impulsive stimulated Raman scattering [20, 19].

In Chapter 3, a systematic study of the phonon structures of the four phases of $BaTiO_3$ is carried out. The three high-temperature phases in the displacive model are found unstable. Stable phase structures are achieved with antiferroelectric distortions. The phase transitions and dynamic structures are studied.

1.5 Domain Wall Structures

The domain switching in ferroelectric materials is accompanied by a small energy, which makes them promising material for data storage. However the domain wall structure is subject to long-term effects: electric fatigue, retention loss, imprint and

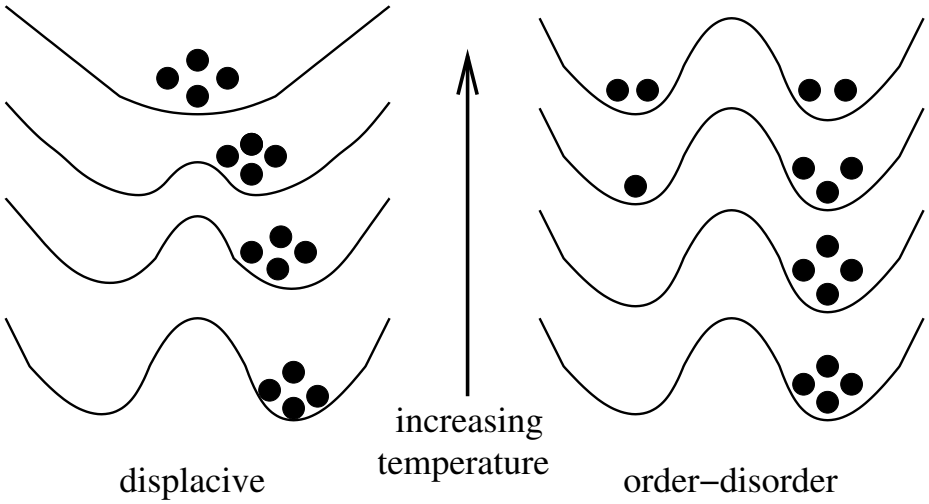

Figure 1.2: Displacive model vs. order-disorder model.

aging. It is argued that such long-term effects are related the heterogeneous structures, e.g., domain walls and oxygen vacancies.

Single domain structure is most stable with the short-circuit electric boundary condition and zero stresses. In practice, under the electric and stress fields ferroelectric materials develop multiple domains to reduce the free energy. In $BaTiO_3$ tetragonal phase, there are 6 equivalent polarization directions. The interfaces between these domains form the 180° walls and the 90° walls.

$BaTiO_3$ 180° domain wall was studied by Landau theory [55, 42, 43] and by an effective Hamiltonian method based on the first-principles calculations [58]. The former calculations lack atomistic resolution while the latter study is on a very small domain system. The detailed structure of the $BaTiO_3$ 90° domain wall has not been studied. Here P-QEq has the advantage to make prediction based on the first-principles approaches. In Chapter 4, the energies and structures of the two types of domain walls are analyzed.

1.6 Oxygen Vacancies

Oxygen vacancies are common defects in oxides. In ferroelectrics, these defects are closely related to polarization fatigue, which is a main problem in commercialization of ferroelectric memories. However a vacancy structure in these materials is not available in theory.

In Chapter 5, the structures and energies of single vacancies, vacancy pairs, and vacancy clusters are studied. The effects of oxygen vacancies on long-term behavior are discussed.

Chapter 2

Polarizable Charge Equilibration Force Field

2.1 Introduction

Ferroelectric (FE) materials have been utilized for many important applications ranging from sensors, actuators to memory devices [48]. Despite many years of research and development on these systems, there remain many questions, such as the domain wall energies for various planes and their migration, the role of defects and impurities on switching behavior and mechanical strength, the structure at surfaces and grain boundaries and their effect on the mechanical and electrical properties. These fundamental properties are needed to understand the hysteresis in the sequential response to fields and stresses involved in various applications. Attempts to understand these effects have been hindered by the large size of the domains and small size of the energy effects controlling the phenomena. Thus, there is a gap between our understanding of the atomic level phenomena and the properties of the macroscopic systems.

The basis for first-principles predictions about these systems is quantum mechanics (QM), and the practical methods available today for QM studies are based on density functional theory (DFT) [35, 44] as extended with generalized gradient approximations (GGA) [59]. With current software it is practical to solve the ground state wave function for periodic cell with 50 to 200 atoms, depending on the system.

But, for FE, it is essential to examine the dynamics of systems large enough to contain domain walls and normal concentrations of defects and to study these systems for time scales of picoseconds and temperatures up to 400K. This is not practical for the current QM methods today. However, we need to base our simulations on QM because the information available from experiment is inadequate to include sufficient empirical data into the simulations. Thus our approach is to develop a force field (FF) with the flexibility needed to describe FE, with parameters can be determined using QM.

The ferroelectric behavior in oxides with the perovskite structure and the nature of ferroelectric phase transitions have been the subject of extensive research for several decades. Earlier density functional computations on $BaTiO_3$ were carried out by Weyrich [76] in 1985. Since that time, *ab initio* calculations have contributed greatly to our understanding of the origins of structural transitions in ferroelectrics [28, 25, 38]. However, direct application of such *ab initio* methods to dynamical behavior at finite temperatures is not feasible.

An alternative approach to studying phase transitions in ferroelectrics is based on constructing the effective Hamiltonians from *ab initio* calculations [82, 81, 83, 29]. This approach includes only the dynamical variables appropriate to the transitions of interest, with parameters fitted to reproduce *ab initio* results in a given material. The four phases of $BaTiO_3$ have been studied in this way. The transition temperatures calculated using this method are considerably lower than experimentally observed. Since increasing the volume favors instabilities, this failure may be ascribed to the lack of thermal expansion within this approach.

Another approach that has been widely applied to the study of dynamical properties of ferroelectrics is based on atomistic models. Modeling inter-atomic forces allows us to study properties related to departures from perfect crystallinity. Atomic-level simulation methods involving force fields with shell model have long been used, with

varied degrees of success, to describe the finite temperature and defect properties of ionic systems as well as the ferroelectrics. For instance, the calculations reported by Lewis and Catlow [46] reproduce the lattice spacing, elastic and dielectric properties for $BaTiO_3$ from molecular mechanics. More recently, Khatib *et al.* [41] proposed an anisotropic shell model with a fourth order correction to describe the perovskites. Tinte *et al.* [71] refined the anisotropic shell model to study phase transitions in $BaTiO_3$ and predicted the correct phase transition sequence, but the transition temperatures were significantly lower than those experimentally observed. Sepliarsky *et al.* [66] have used shell model in molecular dynamics simulations to study various ferroelectrics.

For describing FE, a fundamental requirement is that the FF allows the charges to polarize and transfer, because the local distortions in the symmetry lead to local electric moments that result in the observed macroscopic fields. In this paper, we presented a general and consistent way to treat both of these effects.

This chapter is organized as follows: in Section 2.2, we present the the total energy expression and each term contributing the total energy: electrostatic and Van der Waals terms. Here, we especially focus on the electrostatic energy. We describe the charge equilibration method for the model. In Section 2.3, we derive the expressions for polarizability, dielectric constants and effective Born charges. In Section 2.4, we present the force field parameters for $BaTiO_3$ using *ab initio* results only. In Section 2.5, we summarize the applicability of the force field.

2.2 Polarizable Charge Equilibration Force Field

We consider an ionic system of N atoms. Each atom i has a core charge q_{ic} at position $\mathbf{r}_{ic}$ (i.e., $\mathbf{r}_i$), and a shell charge q_{is} at position $\mathbf{r}_{is}$. The total charge of atom i, q_i, is the sum of q_{ic} and q_{is}. The displacement of shell i *w.r.t.* its core, $\mathbf{r}_{is,ic}$, is $\mathbf{r}_{is} - \mathbf{r}_{ic}$.

The charge densities of the cores and shells are Gaussian functions characterized by range parameters α_{ic} and α_{is}:

$$\rho_{ic}(\mathbf{r}) = \left(\frac{\alpha_{ic}}{\pi}\right)^{\frac{3}{2}} q_{ic} \exp\left(-\alpha_{ic} |\mathbf{r} - \mathbf{r}_{ic}|^2\right), \quad (2.1)$$

$$\rho_{is}(\mathbf{r}) = \left(\frac{\alpha_{is}}{\pi}\right)^{\frac{3}{2}} q_{is} \exp\left(-\alpha_{is} |\mathbf{r} - \mathbf{r}_{is}|^2\right). \quad (2.2)$$

In conventional shell models, atomic polarizability is accounted for by defining a core and a shell for each ion which interact with each other through a harmonic spring (with a force constant that characterizes the ionic polarizability) while interact with the cores and shells of other ions via Coulombic interactions.

In our model, the charge on each atom is partitioned into a Gaussian-shaped core with positive fixed charge (nucleus and inner electron) and a Gaussian-shaped shell with negative variable charge (valence electrons). Shell charges can flow from atom to atom based on the Charge Equilibration scheme [62]. The shells can be displaced from the cores, with the restoring force between a core and its shell given by the electrostatic interaction between the two charge distributions; no harmonic springs are required. Fig. 2.1 shows the partition of a two-atom system in this model, where there are C_4^2, i.e., 6 pairs of Coulombic interaction between all cores and shells.

2.2.1 Total Energy

The total potential energy of a system E^P is a function of atom coordinates. It consists of electrostatic energy, E^{ES}, and Van der Waals energy, E^{VDW}.

$$E^P(\{\mathbf{r}\}) = \min_{\{\mathbf{r_{ic}}=\mathbf{r}\}} E^{PO}(\{\mathbf{r}_{ic},\ \mathbf{r}_{is},\ q_{is}\}), \quad (2.3)$$

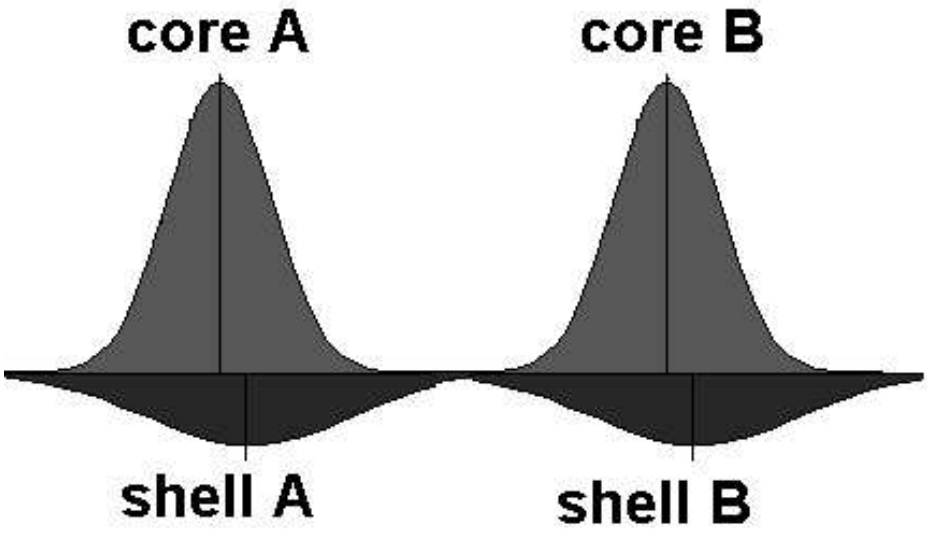

Figure 2.1: Partition of a two-atom system in the model.

where

$$E^{PO}\left(\{\mathbf{r}_{ic},\ \mathbf{r}_{is},\ q_{is}\}\right) = E^{ES}\left(\{\mathbf{r}_{ic},\ \mathbf{r}_{is},\ q_{is}\}\right) + E^{VDW}\left(\{\mathbf{r}_{is}\}\right), \tag{2.4}$$

2.2.2 Electrostatic Energy

For an isolated single atom system, the electronegativity χ_i^o and idempotential J_i^o are defined as

$$\chi_i^o \equiv \frac{\partial E_i^{ES}(\mathbf{r}_{is,ic},\ q_i)}{\partial q_{is}}|_{\mathbf{r}_{is,ic}=0,q_i=0}, \tag{2.5}$$

$$J_i^o \equiv \frac{\partial^2 E_i^{ES}(\mathbf{r}_{is,ic},\ q_i)}{\partial q_{is}^2}|_{\mathbf{r}_{is,ic}=0,q_i=0}. \tag{2.6}$$

The electrostatic interaction energy between two Gaussian-shaped charges [7] is $j_{ik,jl}(\mathbf{r}_{ik,jl})q_{ik}q_{jl}$, where $j_{ik,jl}$ is a basic coupling function,

$$j_{ik,jl}(\mathbf{r}) = \frac{1}{r}\mathrm{erf}\left(\sqrt{\frac{\alpha_{ik}\alpha_{jl}}{\alpha_{ik}+\alpha_{jl}}}r\right), \tag{2.7}$$

i and j represent the atoms, and k and l represent the core (c) and shell (s). In the case of $\mathbf{r}_{ik} = \mathbf{r}_{jl}$, $j_{ik,jl}$ takes the limit:

$$j^o_{ik,jl} \equiv \lim_{r\to 0} j_{ik,jl}(\mathbf{r}) = \frac{2}{\sqrt{\pi}}\sqrt{\frac{\alpha_{ik}\alpha_{jl}}{\alpha_{ik}+\alpha_{jl}}}. \tag{2.8}$$

Let us consider the form of $E^{ES}(\{\mathbf{r}_{ic},\ \mathbf{r}_{is},\ q_{is}\})$. The classic electrostatic energy for this system can be divided into two parts: within each atom and among atoms.

$$\begin{aligned} E^{ES}\left(\{\mathbf{r}_{ic},\ \mathbf{r}_{is},\ q_{is}\}\right) &= \sum_i^N E_i^{ES}(\mathbf{r}_{is,ic},\ q_i) \\ &\quad + \frac{1}{2}\sum_{i\neq j} j_{ik,jl}(\mathbf{r}_{ik,jl}) q_{ik} q_{jl}. \end{aligned} \tag{2.9}$$

The interaction within each atom, i.e., the first term on the right-hand side of Eq. (2.9), is a function of the atom's electronic polarization and total charge.

$$\begin{aligned} E_i^{ES}(\mathbf{r}_{is,ic},\ q_i) &= E_i^{ES}(0,\ q_i) \\ &\quad + \left(E_i^{ES}(\mathbf{r}_{is,ic},\ q_i) - E_i^{ES}(0,\ q_i)\right) \\ &= \left(E_i^o + \chi_i^o q_i + \frac{1}{2}J_i^o q_i^2 + O(q_i^3)\right) \\ &\quad + \left(j_{ic,is}(\mathbf{r}_{ic,is}) - j^o_{ic,is}\right) q_{ic} q_{is} \\ &\approx E_i^o + j^o_{ic,is} q_{ic}^2 + (\chi_i^o - j^o_{ic,is} q_{ic}) q_i \\ &\quad + \frac{1}{2}J_i^o q_i^2 + j_{ic,is}(\mathbf{r}_{ic,is}) q_{ic} q_{is}. \end{aligned} \tag{2.10}$$

$O(q_i^3)$ is ignored in the final step in Eq. (2.10). Substitute Eq. (2.10) into Eq. (2.9), we obtain the electrostatic energy of the system

$$\begin{aligned} E^{ES}\left(\{\mathbf{r}_{ic},\ \mathbf{r}_{is},\ q_{is}\}\ \right) &= \sum_i^N \left(E_i^o + j^o_{ic,is} q_{ic}^2 + \left(\chi_i^o - j^o_{ic,is} q_{ic}\right) q_i + \frac{1}{2}J_i^o q_i^2\right) \\ &\quad + \frac{1}{2}\sum_{ik\neq jl} j_{ik,jl}(\mathbf{r}_{ik,jl}) q_{ik} q_{jl}. \end{aligned} \tag{2.11}$$

The second term on the right-hand side of Eq. (2.11), $\frac{1}{2}\sum_{ik\neq jl} j_{ik,jl}(\mathbf{r}_{ik,jl})q_{ik}q_{jl}$, is the interaction energy between all cores and shells, E^{ES2}. In a periodic system, E^{ES2} can be summed as per Eq. (2.12), using the Ewald method [23].

$$\begin{aligned} E^{ES2} &= \frac{1}{2}\frac{4\pi}{V}\sum_{\mathbf{G}\neq 0} G^{-2}\sum_{ik} q_{ik}\exp(-\frac{G^2}{4\alpha_{ew}})\exp(i\mathbf{G}\cdot\mathbf{r}_{ik}) \\ &\quad \times\sum_{jl} q_{jl}\exp(-\frac{G^2}{4\alpha_{jl}})\exp(i\mathbf{G}\cdot\mathbf{r}_{ik}) \\ &\quad +\frac{1}{2}\sum_{ik}\sum_{jl}\sum_{\mathbf{L}} j_{ik,jl}(\mathbf{r}_{ik,jl}+\mathbf{L})q_{ik}q_{jl} \\ &\quad -\frac{1}{2}\sum_{ik}\sum_{jl}\sum_{\mathbf{L}} j_{ik,ew}(\mathbf{r}_{ik,jl}+\mathbf{L})q_{ik}q_{jl} \\ &\quad -\frac{1}{2}\sum_{ik}\sqrt{\frac{2\alpha_{ik}}{\pi}}q_{ik}^2. \end{aligned} \tag{2.12}$$

where $\mathbf{G}$, $\mathbf{L}$ are the reciprocal lattice vectors and real space vectors, and subscripts ew in α_{ew} and $j_{ik,ew}$ denote the Gaussian parameters included in the Ewald method.

Eq. (2.11) has a single general form for both non-periodic and 3D-periodic model systems,

$$\begin{aligned} E^{ES}\left(\{\mathbf{r}_{ic},\ \mathbf{r}_{is},\ q_{is}\}\right) &= \sum_{i}^{N}\left(E_i^o + j_{ic,is}^o q_{ic}^2 + \left(\chi_i^o - j_{ic,is}^o q_{ic}\right)q_i + \frac{1}{2}J_i^o q_i^2\right) \\ &\quad +\frac{1}{2}\sum_{ik,jl} J_{ik,jl}(\mathbf{r}_{ik,jl})q_{ik}q_{jl}. \end{aligned} \tag{2.13}$$

where

$$J_{ik,jl}(\mathbf{r}_{ik,jl}) = \begin{cases} j_{ik,jl}(\mathbf{r}_{ik,jl}), & ik\neq jl; \\ 0, & ik = jl \end{cases} \tag{2.14}$$

for non-periodic systems and

$$\begin{aligned} J_{ik,jl}(\mathbf{r}_{ik,jl}) &= \frac{4\pi}{V}\sum_{\mathbf{G}\neq 0} G^{-2}\exp(-\frac{G^2}{4\alpha_{ew}}-\frac{G_{jl}^2}{4\alpha_{jl}})\exp(i\mathbf{G}\cdot\mathbf{r}_{ik,jl}) \\ &+\sum_{\mathbf{L}}\left(j_{ik,jl}(\mathbf{r}_{ik,jl}+\mathbf{L})-j_{ik,ew}(\mathbf{r}_{ik,jl}+\mathbf{L})\right) \\ &+\frac{\pi}{2V}(\frac{1}{\alpha_{ik}}-\frac{1}{\alpha_{jl}}) \\ &-\delta_{ik,jl}\sqrt{\frac{2\alpha_{ik}}{\pi}} \end{aligned} \tag{2.15}$$

for periodic systems. In Eq. 2.15, α_{ew} is the range parameter of the Ewald screening charges, i.e.,

$$\rho_{ik}^{ew}(\mathbf{r}) = \left(\frac{\alpha_{ew}}{\pi}\right)^{\frac{3}{2}} q_{ik}\exp\left(-\alpha_{ew}\left|\mathbf{r}-\mathbf{r}_{ik}\right|^2\right)$$

and $j_{ik,ew}$ is the basic coupling function between two charges with range parameters α_{ik} and α_{ew}, i.e.,

$$j_{ik,ew}(\mathbf{r}) = \frac{1}{r}\mathrm{erf}\left(\sqrt{\frac{\alpha_{ik}\alpha_{ew}}{\alpha_{ik}+\alpha_{ew}}}r\right).$$

2.2.3 Charge Transfer

The charge flow from shell to shell is described by an extension of the Charge Equilibration Method of Rappe and Goddard [62]. In the following subsections, we only describe those features unique to the new polarizable charge model.

2.2.3.1 Exact Solution

The shell charges of the system transfer from shell to shell until the chemical potentials χ_i of all shells equal to each other. Let χ denote the equilibrium value. Then for

$i = 1 \cdots N$,

$$\begin{aligned} \chi_i &\equiv \frac{\partial E^{ES}}{\partial q_{is}} \\ &= \chi_i^o - j^o_{ic,is} q_{ic} + J_i^o q_i \\ &\quad + \sum_j (J_{is,jc} q_{jc} + J_{is,js} q_{js}), \end{aligned} \tag{2.16}$$

and

$$\chi_i = \chi. \tag{2.17}$$

Combining Eq. (2.16) and Eq. (2.17), we get

$$\sum_j (J_{is,js} + \delta_{ij} J_i^o) q_{js} - \chi = -\sum_j (J_{is,jc} + \delta_{ij} J_i^o) q_{jc} - \chi_i^o + j^o_{ic,is} q_{ic}, \tag{2.18}$$

where $j = 1 \cdots N$. Besides Eq. (2.18), we have the condition of charge conservation,

$$\sum_i -q_{is} = \sum_i q_{ic} - Q_{tot}, \tag{2.19}$$

where the total charge of the system Q_{tot} can be non-zero value for charged non-periodic systems but must be zero for 3D-periodic systems to converge the electrostatic energy. Eq. (2.18) and Eq. (2.19) can be solved by linear algebra,

$$C \begin{pmatrix} q_{1s} \\ q_{2s} \\ \cdots \\ q_{Ns} \\ \chi \end{pmatrix} = \begin{pmatrix} -\sum_j (J_{1s,jc} + \delta_{1j} J_1^o) q_{jc} - \chi_1^o + j^o_{1c,1s} q_{1c} \\ -\sum_j (J_{2s,jc} + \delta_{2j} J_2^o) q_{jc} - \chi_2^o + j^o_{2c,2s} q_{2c} \\ \cdots \\ -\sum_j (J_{Ns,jc} + \delta_{Nj} J_N^o) q_{jc} - \chi_N^o + j^o_{Nc,1s} q_{Nc} \\ \sum_j q_{jc} - Q_{tot} \end{pmatrix}, \tag{2.20}$$

where C is the electrostatic coupling matrix,

$$C \equiv \begin{pmatrix} J_{1s,1s}+J_1^o & J_{1s,2s} & \cdots & J_{1s,Ns} & -1 \\ J_{2s,1s} & J_{2s,2s}+J_2^o & \cdots & J_{2s,Ns} & -1 \\ \cdots & \cdots & \cdots & \cdots & \cdots. \\ J_{Ns,1s} & J_{Ns,2s} & \cdots & J_{Ns,Ns}+J_N^o & -1 \\ -1 & -1 & \cdots & -1 & 0 \end{pmatrix}. \tag{2.21}$$

2.2.3.2 Large System Solution

The exact method requires computation memory of $O(N^2)$ and computation time of $O(N^3)$. For conventional MD simulations today, N is about 1,000 to 1,000,000 and thus solving Eq. (2.20) is not feasible. Therefore for the large systems, we use the following self-consistent field method to reduce the computational cost. From Eq. (2.16) we can get the idempotential of atom i:

$$J_i \equiv \frac{\partial \chi_i}{\partial q_{is}} = J_i^o + J_{is,is}. \tag{2.22}$$

The chemical potential change of atom i is given by a Taylor expansion

$$\begin{aligned} d\chi_i &= \sum_j \frac{\partial \chi_i}{\partial q_{js}} dq_{js} + \sum_{j,k} \frac{\partial^2 \chi_i}{\partial q_{js} \partial q_{ks}} dq_{js} dq_{ks} + \cdots \\ &\approx J_i dq_{is}, \end{aligned} \tag{2.23}$$

where we ignored the second term and thereafter on the right-hand side of Eq. (2.23) and assumed $\frac{\partial \chi_i}{\partial q_{js}}$ is negligible for $i \neq j$. Since the total charge of the system conserves,

$$\sum_i dq_{is} = \sum_i \frac{d\chi_i}{J_i} = \sum_i \frac{\chi - \chi_i}{J_i} = 0, \tag{2.24}$$

the chemical potential of the system is

$$\chi = \frac{\sum_i \frac{\chi_i}{J_i}}{\sum_i \frac{1}{J_i}}. \tag{2.25}$$

From χ_i, J_i, J and q_i^j, we can predict

$$q_i^{j+1} = q_i^j + dq_i = q_i^j + \frac{\chi - \chi_i}{J_i}. \tag{2.26}$$

Starting from an initial guess of charge distribution $\{q_i^j\}$, we can obtain the atomic chemical potentials $\{\chi_i\}$, idempotentials $\{J_i\}$ and the system chemical potential χ from Eq. (2.16), Eq. (2.22) and Eq. (2.25). Then, the new charge distribution $\{q_i^{j+1}\}$ can be obtained by Eq. (2.26). The above steps are repeated until all charges converge, i.e., self consistency field is achieved

The self-consistent field method is both memory and speed efficient. Single step calculation is close to O(N). Further, χ_i and J_i can be evaluated with forces during MD and cause negligible computational overhead.

2.2.4 Shell Relaxation

According to Eq. (2.3), we need to relax the shell coordinates for each configuration of the core coordinates. We use the Steepest Decent Method or the Conjugate Gradient Method to perform shell relaxation based on the first derivatives and/or the second derivatives of energy *w.r.t.* the coordinates.

2.2.5 Derivatives of E^{ES}

For many applications, 1st and 2nd derivatives of the energy are required to describe the system: forces, stress, Hessian and elastic constants. Under the condition of charge equilibrium and shell relaxation, all these quantities have analytical forms.

See Appendix A.4 for details.

2.2.6 Fourth-Order Correction to Core-Shell Interaction

When a core and its shell are separated far away from each other during MD simulations, the restoring force between them from the purely electrostatic interaction is not sufficient to keep the shells bond to the core. Thus, for large polarization in ions, we need a quadratic energy term, $K_i \mathbf{r}_{is,ic}^4$, to correct the force.

2.2.7 Van der Waals Energy

The classic electrostatic model should be corrected for two quantum effects: Pauli repulsion due to the antisymmetry of the total electronic wave function and London dispersion due to electronic fluctuation. For the interaction between two cations or two anions, both effects can be ignored because electrostatic repulsion dominates. For the interaction between a cation and an anion, a term to correct the Pauli repulsion must be included. In this case, no London dispersion term is needed, as electrostatic attraction dominates. For simplicity, we describe Pauli repulsion between shells by an exponential potential

$$E^{VDW} = \sum_{i>j} E_{ij}^{VDW}(r_{is,js}) = \sum_{i>j} D_{ij} \exp(-\frac{r_{is,js}}{R_{ij}}), \tag{2.27}$$

where $\mathbf{r}_{is,js} = \mathbf{r}_{is} - \mathbf{r}_{js}$.

2.3 Dielectric Properties from Molecular Mechanics

2.3.1 Polarizability and Dielectric Constants

When the electric field frequency is very low, all cores and shells relax under the external field. In the case of a high frequency electric field, all cores are frozen while only shells relax under the the external field. These two polarizabilities are called static and optical, respectively, and can be written as

$$\begin{aligned}\alpha^0_{xy} &= \sum_{ik}\sum_{jl} q_{ik} H^{-1}_{ikx,jly} q_{jl} \\ &+ \sum_{jlz}\left(\sum_i r_{isx}\frac{\partial q_{is}}{\partial r_{jlz}}\right)\left(\sum_{mn} H^{-1}_{jlz,mny} q_{mn}\right) \\ &+ \sum_i r_{isx}\frac{\partial q_{is}}{\partial E_y} \end{aligned} \tag{2.28}$$

and

$$\begin{aligned}\alpha^\infty_{xy} &= \sum_{i}\sum_{j} q_{is} (H^{ss})^{-1}_{ix,jy} q_{js} \\ &+ \sum_{jz}\left(\sum_i r_{isx}\frac{\partial q_{is}}{\partial r_{jsz}}\right)\left(\sum_{m} (H^{ss})^{-1}_{jz,my} q_{ms}\right) \\ &+ \sum_i r_{isx}\frac{\partial q_{is}}{\partial E_y}, \end{aligned} \tag{2.29}$$

where H is the Hessian matrix for all cores and shells and H^{ss} is the Hessian matrix for all shells. Appendix A.6 gives Eq. (2.28) and Eq. (2.29), Appendix A.4 describe the electrostatic component of Hessian, and Appendix A.3 describes $\frac{\partial q_{is}}{\partial r_{jlz}}$ and $\frac{\partial q_{is}}{\partial E_y}$.

The corresponding dielectric constants are

$$\varepsilon^0_{xy} = \delta_{xy} + \frac{4\pi}{V}\alpha^s_{xy}, \tag{2.30}$$

$$\varepsilon^\infty_{xy} = \delta_{xy} + \frac{4\pi}{V}\alpha^o_{xy}. \tag{2.31}$$

2.3.2 Born Effective Charges

The Born effective charge for an atom characterizes the dynamic charge effects, and has the form of

$$q^*_{i,xy} \equiv \frac{\partial \mu_y}{\partial r_{icx}} \tag{2.32}$$

$$= \sum_j \left(q_{js} \frac{\partial r_{jsy}}{\partial r_{icx}} + \sum_{kz} \frac{\partial q_{js}}{\partial r_{ksz}} \frac{\partial r_{ksz}}{\partial r_{icx}} r_{jsy} \right) + \delta_{xy} q_{ic}, \tag{2.33}$$

where i represents the atom, x and y represent the directions, μ_y is the dipole moment in y direction, $\frac{\partial q_{js}}{\partial r_{icx}}$ is the derivative of the atom j shell charge *w.r.t.* the x-component of atom i core coordinates, and $\frac{\partial r_{jsy}}{\partial r_{icx}}$ is the derivative of the y-component of the atom j shell coordinates *w.r.t.* the x-component of the atom i core coordinates. The forms of these derivatives are given in Appendix A.3 and Appendix A.5.

2.4 Force Field Optimization and Verification for $BaTiO_3$

$BaTiO_3$ is, to date, the most extensively investigated ferroelectric material. Thus, we take it as a touchstone. We optimize the parameters of our force field from *ab initio* DFT calculations reported earlier [72] on different phases of $BaTiO_3$ and various molecular clusters [31]. The force field is optimized to reproduce static and dynamic charge properties as well as equation of state for different phases of $BaTiO_3$. The optimized electrostatic and Van der Waals parameters are summarized in Table 2.1 and Table 2.2.

The static charge properties include Mulliken charges (Table 2.3) and polarizations (Table 2.5). Mulliken charges account for the electron population on each atom, while polarizations characterize the displacements of the electrons from their nucleus.

Table 2.1: Parameters of the electrostatic terms for $BaTiO_3$.

i	χ_i^o [a] (V)	J_i^o ($V \cdot e^{-1}$)	q_{ic} (e)	$\frac{1}{2\sqrt{\alpha_{ic}}}$ [b] (Å)	$\frac{1}{2\sqrt{\alpha_{is}}}$ (Å)	K_i [c] ($eV \cdot Å^{-4}$)
Ba	-24.0033	18.9960	2.8780	0.3978	0.3978	100.0
Ti	-47.1251	30.5478	5.7730	0.2947	0.2947	100.0
O	18.5565	30.3158	2.0951	0.3571	0.3571	100.0
H	0.8232	21.5643	1.0000	0.0001	0.1500	100.0

[a] Negative for accurate description of electronegativity of Ba and Ti in $BaTiO_3$ where Mulliken charges of Ba and Ti are around 1.57 and 1.60, respectively

[b] Here we keep $\alpha_{ic} = \alpha_{is}$ except for H to reduce the degree of parameter freedom for simplicity. We expect better description if we release this constraint.

[c] K_i can be set in a broad range, from 50 to 400. Here we set all of them to be 100 for simplicity.

Table 2.2: Parameters of the Van der Waals terms for $BaTiO_3$.

ij	D_{ij} (eV)	R_{ij} (Å)
$Ba-O$	1.0667E+7	0.153630
$Ti-O$	2.8246E+3	0.247883

The dynamic charge properties included Born effective charges (Table 2.4) and optical dielectric constants (Table 2.5). Born effective charges describe the electron-nucleus coupling in the low frequency limit. Optical dielectric constants give the electron-nucleus coupling in the high frequency limit.

The lattice parameters(Table 2.5), phase energetics (Table 2.6), soft mode energies (Fig. 2.2) and bulk moduli (Table 2.5) are used to determine the equations of state.

2.5 Conclusions

We have developed an elaborate classical force field model for materials systems (in particular for ferroelectrics) that properly characterizes charge transfer and atomic polarization. This approach reproduces the correct phase transition sequence, transition temperatures, and spontaneous polarization in $BaTiO_3$. The method replaces

Table 2.3: Mulliken charges.

Molecule	Atom	q (QM) [a]	q (P-QEq)
$Ti(OH)_4$	Ti	+1.92	+2.35
	O	-0.89	-1.08
	H	+0.41	+0.48
$TiO(OH)_2$	Ti	+1.75	+2.28
	O1	-0.94	-1.09
	O2	-0.68	-0.97
	H	+0.40	+0.44
BaO	Ba	+0.90	+1.14
	O	-0.90	-1.14
$OBa_2(OH)_2$	Ba	+1.22	+1.49
	O1	-1.10	-1.16
	O2	-1.00	-1.13
	H	+0.33	+0.21
Ba_2O_2	Ba	+1.02	+1.24
	O	-1.02	-1.24
$BaO_2Ti(OH)_2$	Ba	+1.25	+1.57
	O1	-0.95	-1.14
	Ti	+1.81	+2.26
	O2	-0.96	-1.10
	H	+0.38	+0.32
$BaTiO_3$(periodic)	Ba	+1.57	+1.74
	Ti	+1.62	+2.16
	O	-1.06	-1.30

[a]Density functional theory calculation with PBE functional [59]by SeqQuest package

Table 2.4: $BaTiO_3$ Born effective charges.

atom	q^* (QM1) [80]	q^* (QM2) [28]	q^* (P-QEq)
Ba	+2.75	+2.77	+2.77
Ti	+7.16	+7.25	+4.83
$O_{\parallel}$	-2.11	-2.15	-1.42
$O_{\perp}$	-5.69	-5.71	-4.76

Table 2.5: Properties of $BaTiO_3$ phases.

Phase	Properties	EXP	QM [a]	P-QEq
cubic	a=b=c (Å)	4.012 [40]	4.007	4.0002
($Pm3m$)	B (GPa)		167.64	159
	ϵ^o	6.05 [b]		4.83
tetra.	a=b (Å)	3.99 [45]	3.9759	3.9997
($P4mm$)	c (Å)	4.03 [45]	4.1722	4.0469
	P_z (μC/cm^2)	$15-26$ [40, 52, 54, 77]		17.15
	B (GPa)		98.60	135
ortho.	a=b (Å)	4.02 [45]	4.0791	4.0363
($Amm2$)	c (Å)	3.98 [45]	3.9703	3.9988
	γ (degree)	89.82 [45]	89.61	89.42
	$P_x = P_y$ (μC/cm^2)	$15-31$ [40, 52, 54, 77]		14.66
	B (GPa)		97.54	120
rhomb.	a=b=c (Å)	4.00 [45]	4.0421	4.0286
($R3m$)	$\alpha = \beta = \gamma$ (degree)	89.84 [45]	89.77	89.56
	$P_x = P_y = P_z$ (μC/cm^2)	$14-33$ [40, 52, 54, 77]		12.97
	B (GPa)		97.54	120

[a] Density functional theory calculation with PW-91 functional by CASTEP [72]
[b] Based on $\epsilon^o = n^2$ for materials with low magnetic susceptibility, where n is the refractive index.

Table 2.6: Energetics for $BaTiO_3$ phases (eV/unit cell).

Phase1	Phase2	ΔE_{12} (QM) [a]	ΔE_{12} (P-QEq)
tetra	cubic	0.0427	0.0324
ortho	tetra	0.0100	0.0163
rhomb	ortho	0.0020	0.0093

[a] Density functional theory calculation using the PW91 functional and CASTEP

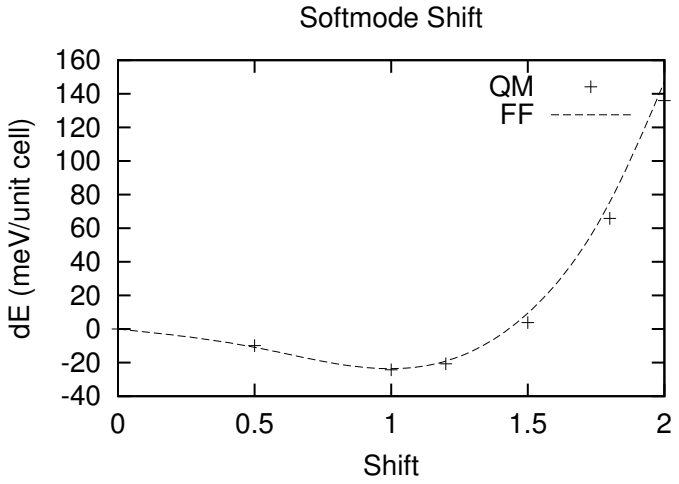

Figure 2.2: The energy change in cubic phase with soft mode shift in direction $\langle 001 \rangle$.

point charge based models with Gaussian distributions and allows charge transfer between shells by extending the widely used charge equilibration scheme from point charges to charge distributions. This P-QEq model allows us to describe variations of charges and polarization effect as a function of configuration of the ions, mimicking the quantum mechanical phenomena appropriately. As the distances or coordinations of atoms/ions change, so do the partial charges and atomic polarizations, enabling the model to reproduce the phase transformations correctly. The handling of electrostatic interactions through this method is general and applicable to ceramics, oxides, covalently bonded systems such as ferro electric polymers, and organic and biological systems with and without chemical reactions.

The P-QEq model is general; if the Gaussian shape parameters $\alpha \to \infty$ the model reduces to a point ion-shell model without harmonic springs. Hence, the force fields developed earlier by us for oxides such as MgO, SiO_2, and can also be handled by the P-QEq approach.

With the P-QEq model it should be practical to consider simulations of large unit cells to study domain boundaries, surface reconstruction, defects, and the effects of temperature, stress, and applied electric fields. When combined with valence terms,

the model could describe heterogeneous covalent systems. The P-QEq model is thus useful for developing improved materials and devices.

Chapter 3

Local Structures and Phase Transitions

3.1 Introduction

Ferroelectric materials have broad applications in the fields of data storage, transducers and capacitors. Among them, $BaTiO_3$ is one of the most studied system. However, even sixty years after its discovery, there are controversies between theories and experiments about this material. One remaining big puzzle is the transition type, whether it is displacive (microscopically nonpolar in paraelectric phase) or order-disorder (microscopically polar in paraelectric phase).

Early theoretical work took a displacive model. Cochran [10, 11] proposed that in the paraelectric phase, Ti atoms are located in cubic symmetry centers. During cooling, some modes around Γ point get soft and one mode freezes during each of the three consecutive phase transitions. These temperature-dependent lattice modes are usually called "soft modes". However, although soft modes are found in $BaTiO_3$, they are heavily overdamped [78, 33].

Bersuker [4] proposed an order-disorder eight-site model based on ligand field theory analysis. In this model, Ti atoms are located in one of its eight potential minima along the [111] directions. A similar model with chains was proposed by Comes *et al.* [15] to explain the diffuse scattering of X-rays [34, 16] and electrons [36].

However, Huller [37] later showed that a displacive model with dynamic phonon correlation in $BaTiO_3$ can also explain these scattering experiments.

Since then arguments between the two models continues. A lot of experiments can not be well explained by the displacive model. Among them are the strong unexpected Raman excitation observed in cubic phase [61], overdamped soft mode in tetragonal phase [20, 19] and local distorted structure for all phases [63]. The major difficulty of the order-disorder theory is the small latent transition heat during phase transition [68].

In this study, we resolve this problem with a first-principles approach. In Section 3.2, we summarize the calculation methods in this study. Then in Section 3.3, we study the phonon structures with the smallest unit cells for all four phases of $BaTiO_3$ with P-QEq. We analyze the unstable phonons and check anisotropy of phonon modes. In Section 3.4, we propose the FE-AFE local structures for the three high-temperature phases, and calculate their corresponding phonon structures. We calculate the thermodynamic functions of these FE-AFE phases and determine their transitions in Section 3.5. In Section 3.6, we analyze the diffuse diffraction. In Section 3.7, we discuss the FE-AFE structures with the Extended X-ray Absorption Fine Structure (EXAFS) and Raman experiments. Finally in Section 3.8, we give our conclusion on transition mechanism.

3.2 Calculation Methods

3.2.1 Dynamical Matrix

Long-wave (LO) modes in polar materials introduce depolarization field. The depolarization field results in a non-analytic term $\mathbf{D}^{na}$ in addition to the analytic term

$\mathbf{D}^{an}$ in the dynamic matrix and causes LO-TO splitting at Γ point [6, 12], i.e.,

$$\mathbf{D}(\mathbf{q}) = \begin{cases} \mathbf{D}^{an}(\mathbf{q}) + \mathbf{D}^{na}(\mathbf{q}), & \mathbf{q} \to \Gamma; \\ \mathbf{D}^{an}(\mathbf{q}), & \text{else.} \end{cases} \tag{3.1}$$

The analytic part of the dynamic matrix $\mathbf{D}^{an}$ [21] for phonon wave vector $\mathbf{q}$ is given by

$$\begin{aligned} \mathbf{D}^{an}(\mathbf{q}) &= \mathbf{D}^{cc}(\mathbf{q}) \\ &\quad -\mathbf{D}^{cs}(\mathbf{q}) \cdot \left(\mathbf{D}^{ss}(\mathbf{q})\right)^{-1} \cdot \left(\mathbf{D}^{cs}(\mathbf{q})\right)^{\dagger}. \end{aligned} \tag{3.2}$$

$\mathbf{D^{cc}}$, $\mathbf{D^{ss}}$ and $\mathbf{D^{cs}}$ are the core-core, shell-shell and core-shell dynamic matrices,

$$\begin{aligned} \mathbf{D}^{cc}_{i\alpha,j\beta}(\mathbf{q}) &= \frac{\sum_l \mathbf{H}^{cc}_{0i\alpha,lj\beta} \times \exp(i\mathbf{q} \cdot [\mathbf{r}^c_{lj} - \mathbf{r}^c_{0i}])}{(m_i m_j)^{1/2}}, \\ \mathbf{D}^{ss}_{i\alpha,j\beta}(\mathbf{q}) &= \sum_l \mathbf{H}^{ss}_{0i\alpha,lj\beta} \times \exp(i\mathbf{q} \cdot [\mathbf{r}^s_{lj} - \mathbf{r}^s_{0i}]), \\ \mathbf{D}^{cs}_{i\alpha,j\beta}(\mathbf{q}) &= \frac{\sum_l \mathbf{H}^{cs}_{0i\alpha,lj\beta} \times \exp(i\mathbf{q} \cdot [\mathbf{r}^s_{lj} - \mathbf{r}^c_{0i}])}{m_i^{1/2}}, \end{aligned} \tag{3.3}$$

where $\mathbf{H^{cc}}$, $\mathbf{H^{ss}}$ and $\mathbf{H^{cs}}$ are the core-core, shell-shell and core-shell Hessian matrices, l indexes the unit cell, i and j index atoms in a unit cell, α and β are the directions in Cartesian coordinates, and $\mathbf{r}^{c/s}_{lj}$ is the position vector of the core (c) or shell (s) of atom j in the l'th unit cell.

The non-analytic part of the dynamic matrix $\mathbf{D}^{na}$ [30] is given by

$$\mathbf{D}^{na}_{i\alpha,j\beta}(\mathbf{q}) = \frac{4\pi e^2}{V} \frac{(\mathbf{Z}^*_i \cdot \mathbf{q})_\alpha (\mathbf{Z}^*_j \cdot \mathbf{q})_\beta}{\mathbf{q}^T \cdot \epsilon^\infty \cdot \mathbf{q}}, \tag{3.4}$$

where $\mathbf{Z}^*$ is the Born Effective Charge, ϵ^∞ is the optical dielectric constants, e is the

electronic charge and V is unit cell volume.

The vibrational frequencies ω and polarization vectors $\mathbf{e}$ for wave vector $\mathbf{q}$ are obtained by solving the equation of motion,

$$\mathbf{D}(\mathbf{q}) \cdot \mathbf{e}(\mathbf{q}, v) = \omega^2(\mathbf{q}, v)\mathbf{e}(\mathbf{q}, v). \tag{3.5}$$

3.2.2 Thermodynamic Functions

Within the harmonic approximation, the thermodynamic functions are calculated from the vibration modes. From the Bose-Einstein statistics, we have

$$\begin{aligned}
ZPE &= \frac{1}{2}\sum_{\mathbf{q},v} \hbar\omega(\mathbf{q}, v), && (3.6)\\
E &= E_o + \frac{1}{2}\sum_{\mathbf{q},v} \hbar\omega(\mathbf{q}, v)\coth(\frac{\hbar\omega(\mathbf{q}, v)}{2k_BT}), && (3.7)\\
F &= E_o + k_BT\sum_{\mathbf{q},v} \ln[2\sinh(\frac{\hbar\omega(\mathbf{q}, v)}{2k_BT})], && (3.8)\\
S &= \frac{1}{2T}\sum_{\mathbf{q},v} \hbar\omega(\mathbf{q}, v)\coth(\frac{\hbar\omega(\mathbf{q}, v)}{2k_BT}) \\
&\quad -k_B\sum_{\mathbf{q},v} \ln[2\sinh(\frac{\hbar\omega(\mathbf{q}, v)}{2k_BT})]. && (3.9)
\end{aligned}$$

3.2.3 Scattering Function of Diffuse Diffraction

Let's consider the inelastic X-ray or neutron scattering function. Suppose an X-ray or neutron beam with incident wave vector $\mathbf{K}$ is scattered by a crystal of N unit cells. The scattered wave vector is $\mathbf{K'}$ and the scattering wave vector is $\mathbf{Q}$ ($=\mathbf{K} - \mathbf{K'}$). τ is a reciprocal lattice point of the crystal. $\overline{f_i}$ is the X-ray atomic scattering factor or neutron scattering length of atom i in the unit cell.

The partial differential cross section due to single-phonon scattering processes

is [21, 50]

$$\left(\frac{\partial^2\sigma}{\partial\Omega\partial\omega}\right)^{\pm} = N\frac{\mathbf{K}'}{\mathbf{K}}\sum_{\tau,v}\int d\mathbf{q}\frac{\hbar\left(n(\mathbf{q},v)+\frac{1}{2}\pm\frac{1}{2}\right)}{2\omega(\mathbf{q},v)} \times|F(\mathbf{Q},\mp\mathbf{q},v)|^2\delta\left(\omega\mp\omega(\mathbf{q},v)\right) \times\delta\left(\mathbf{Q}\mp\mathbf{q}-\tau\right). \tag{3.10}$$

$F(\mathbf{Q},\mathbf{q},v)$ is the dynamic structure factor,

$$F(\mathbf{Q},\mathbf{q},v) = \sum_i\frac{\overline{f_i}}{\sqrt{M_i}}\exp(-W_i(\mathbf{Q})+i\mathbf{Q}\cdot\mathbf{r}_i) \times(\mathbf{Q}\cdot\mathbf{e}_i(\mathbf{q},v)), \tag{3.11}$$

where $W_i(\mathbf{Q})$ is the Debye-Waller factor,

$$\begin{aligned} W_i(\mathbf{Q}) &= \frac{1}{2}\langle(\mathbf{Q}\cdot\mathbf{u}_i)^2\rangle \\ &= \frac{1}{2N_m}\sum_{\mathbf{q},v}\langle(\mathbf{Q}\cdot\mathbf{u}_i(\mathbf{q},v))^2\rangle \\ &= \frac{\hbar}{2M}\frac{1}{N_m}\sum_{\mathbf{q},v}\frac{\left(n(\mathbf{q},v)+\frac{1}{2}\right)\left(\mathbf{Q}\cdot\mathbf{e}_i(\mathbf{q},v)\right)^2}{\omega(\mathbf{q},v)}, \end{aligned} \tag{3.12}$$

and $n(\mathbf{Q},v)$ is the phonon excitation number given by Bose-Einstein statistics,

$$n(\mathbf{q},v) = \left(\exp(\frac{\hbar\omega(\mathbf{q},v)}{k_BT})-1\right)^{-1}. \tag{3.13}$$

Integrate Eq. (3.10) over all phonon frequencies and sum over the phonon absorption and emission processes, we obtain the differential cross section,

$$\left(\frac{\partial\sigma_1}{\partial\Omega}\right) = N\frac{\mathbf{K}'}{\mathbf{K}}\sum_v\frac{\hbar\left(n(\mathbf{Q},v)+\frac{1}{2}\right)}{\omega(\mathbf{Q},v)} \times|F_1(\mathbf{Q},-\mathbf{Q},v)|^2. \tag{3.14}$$

So the corresponding scattering function $S_1(\mathbf{Q})$ and dynamic structure factor $F_1'(\mathbf{Q}, v)$ are

$$S_1(\mathbf{Q}) = \sum_v \frac{\hbar\left(n(\mathbf{Q}, v) + \frac{1}{2}\right)}{\omega(\mathbf{Q}, v)} |F_1'(\mathbf{Q}, v)|^2$$

and

$$\begin{aligned} F_1'(\mathbf{Q}, v) &= \sum_i \frac{\overline{f_i}}{\sqrt{M_i}} \exp(-W_i(\mathbf{Q}) + i\mathbf{Q} \cdot \mathbf{r}_i) \\ &\quad \times (\mathbf{Q} \cdot \mathbf{e}_i^*(\mathbf{Q}, v)). \end{aligned} \tag{3.15}$$

3.3 Phonon Structure

$BaTiO_3$ phonon structure were studied by the first-principles approaches with the DFT/LDA approximation in the last decade. Among them, Zhong *et al.* [80] found giant LO-TO splitting in a series of ABO3 cubic perovskite compound. Lattice dynamics studies reveals two-dimensional character in the Brillouin zone in the cubic phases of $BaTiO_3$ [27, 71] as well as $KNbO_3$ [79]. These calculations showed that there are unstable phonons in the cubic phase of the displacive model. However direct first-principles phonon calculation is not feasible for larger systems. In this paper we calculated the phonon structure with PQEq field obtained from DFT/GGA calculations. The PQEq force field was developed to reproduce the energies and structures of the quantum calculation.

We study the phonon structures of the four phases using the smallest primitive cell. Subject to this constraint, the cubic, tetragonal, orthogonal and rhombohedral phases have the symmetry groups of $Pm3m$, $P4mm$,$Amm2$ and $R3m$, respectively.

phonon structures are closely related to phase stability. Generally speaking, if all phonon frequencies in the Brillouin zone are real, then the static structure is stable. Otherwise, the structure will transform to another symmetry by following the motion of some of its unstable phonons.

For $BaTiO_3$ $Pm3m$ phase, there are 12 optical phonon branches. At Γ point, symmetry analysis showed that there are 3 polar F_{1u} and 1 nonpolar F_{2u} modes, each of them triply degenerated.

In the frozen phonon structure of $Pm3m$ phase (Fig. 3.2), two F_{1u} modes are unstable along Γ-X direction. The modes at the Γ point give homogeneous ferroelectric distortions with in-phase motions between neighboring cells. These modes cause macroscopic polarization and break cubic symmetry. The modes at the Brillouin boundary give antiferroelectric distortions with out-phase motion in neighboring cells. These distortions give macroscopically non-polar but locally polar structure. The modes in the middle between zone center and zone boundary gives an structure with domains, cubic symmetry in each domain breaks and the lattice parameters of the resulting unit cells are larger than $2a$. So the distortions which can give a smallest stable cubic structure (with a larger unit cell) are from the phonon modes at zone boundaries. Further analysis shows that this structure can be achieved by the joint motions of the three TO modes at the side-centers of the first Brillouin zone, i.e., $(0\frac{1}{2}\frac{1}{2})$, $(\frac{1}{2}0\frac{1}{2})$ and $(\frac{1}{2}\frac{1}{2}0)$. The same structure can also be obtained by six TO modes at three face-centers. These antiferroelectric distortions result in a stable cubic structure with symmetry $I-43m$. In this structure, Ti atoms do occupy one of eight [111] sites as in the order-disorder model. However the occupation is always ordered in an antiferroelectric configuration. Thus there is no configuration entropy contribution from the dynamic disorder. This is consistent with the small latent heat during phase transition [68].

Phonon dispersion at the Γ point in $P4mm$ phase is highly anisotropic. Along the $\Gamma - X_3$ direction, we see two TO are unstable as in $P4mm$ phase. Thus, the antiferroelectric distortion can exist between each pair of neighboring unit cell in x or y direction. Along the $\Gamma - X_1$ direction, only one TO with y-polarization is unstable. Following the two unstable TO modes at X_3, the unstable $P4mm$ structure changed

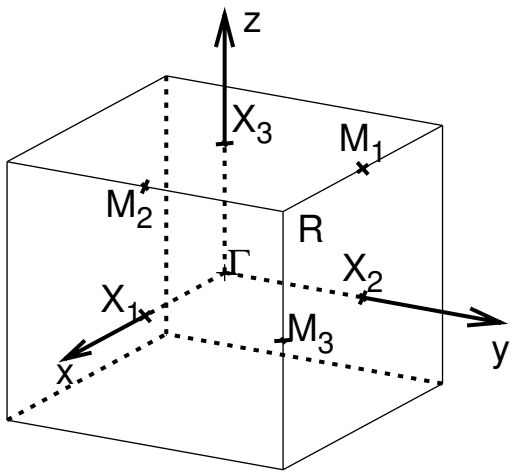

Figure 3.1: Dispersion points in Brillouin zone.

into stable $I4cm$.

Similarly, following the joint motion of the unstable phonon modes at M_1 and M_2, $Amm2$ phase will change into $Pmn21$ within its orthogonal symmetry.

In $R3m$ phases, all phonons are stable throughout the whole Brillouin zone and the local structure is stable.

3.4 Local Phase Structures

Sec. 3.3 shows that by the antiferroelectric distortions, the symmetry of the three high-temperature phase reduces and the number of atoms in prime cell increases. The result is summarized in Table 3.1. We refer these structures as FE-AFE phase structures.

An FE-AFE phase structure can be described by three sets of $-\mathrm{O}-\mathrm{Ti}-\mathrm{O}-$ chains. Each chain is polar and has two possible polarizations along the chain direc-

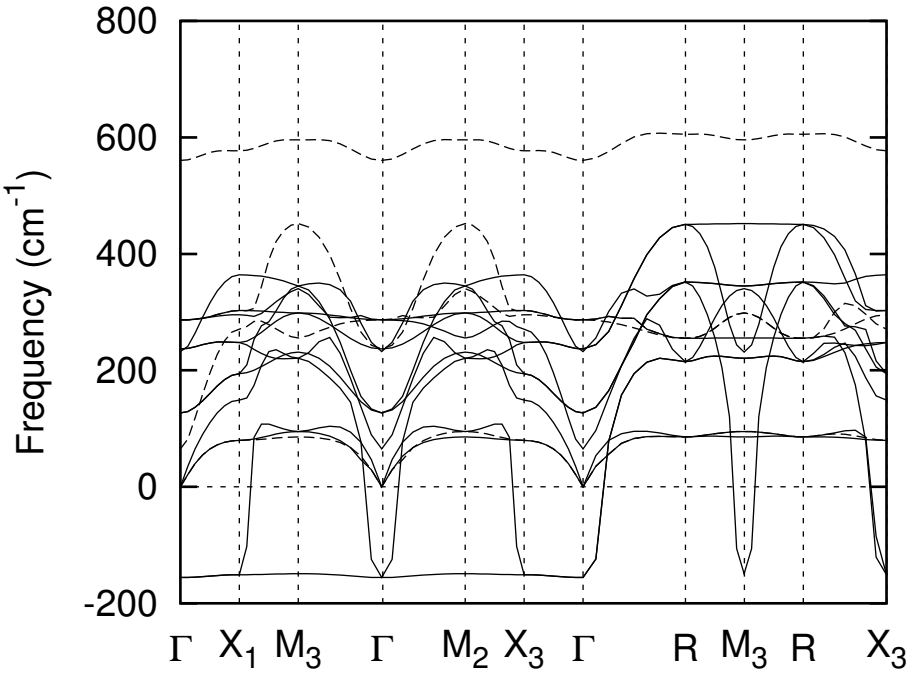

Figure 3.2: Frozen phonon structure of $BaTiO_3$ $Pm3m$ cubic phase.

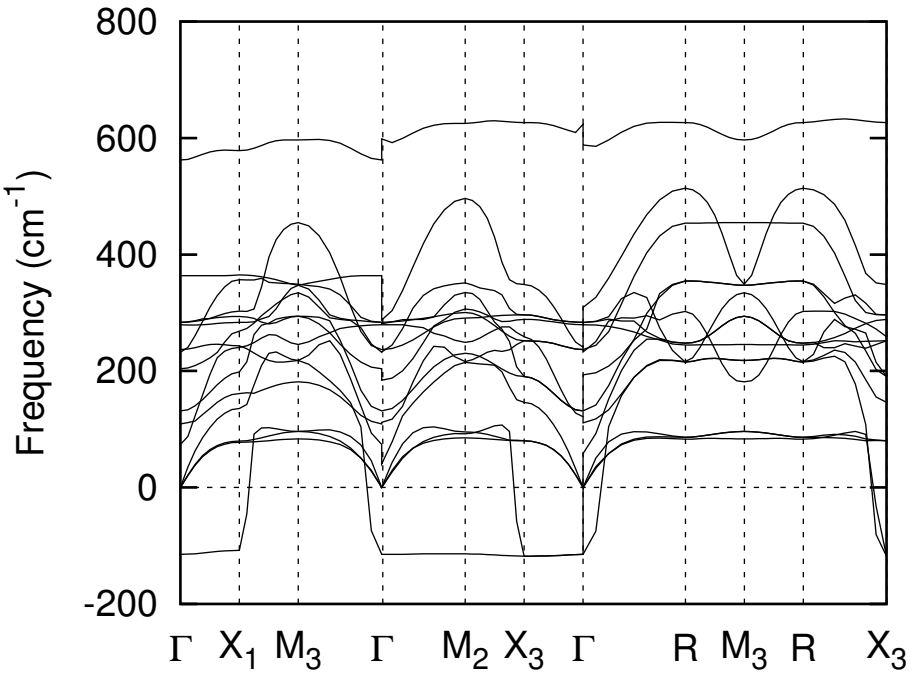

Figure 3.3: Frozen phonon structure of $BaTiO_3$ $P4mm$ tetragonal phase.

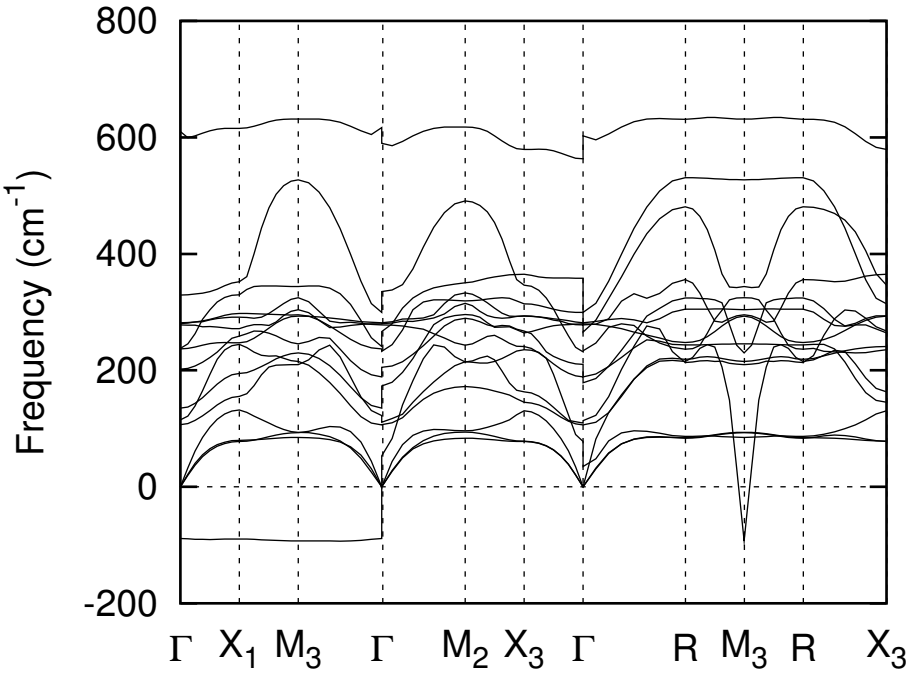

Figure 3.4: Frozen phonon structure of $BaTiO_3$ $Amm2$ orthorhombic phase.

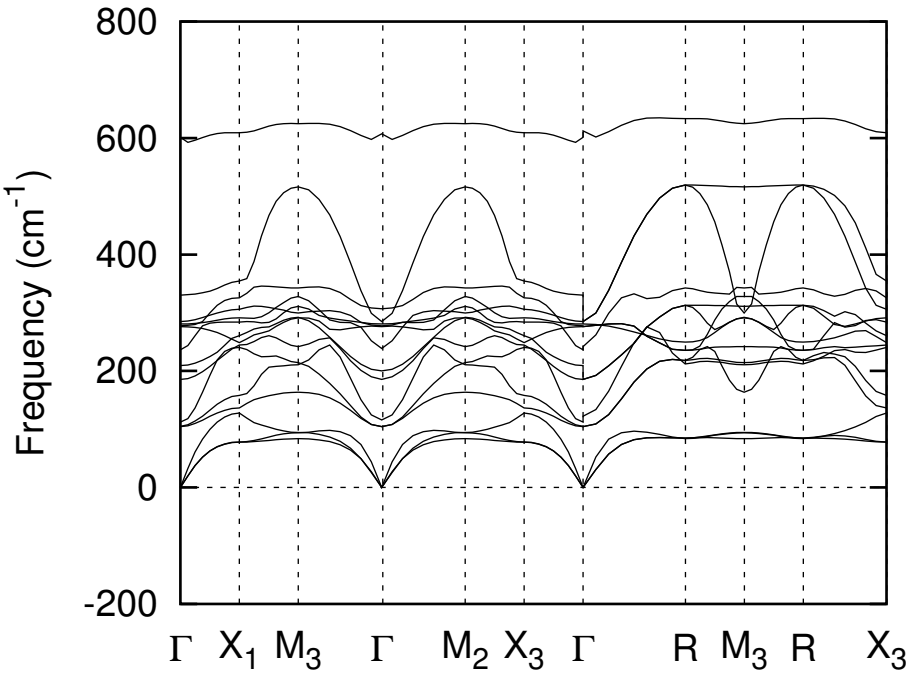

Figure 3.5: Static phonon structure of $BaTiO_3$ $R3m$ rhombohedral phase.

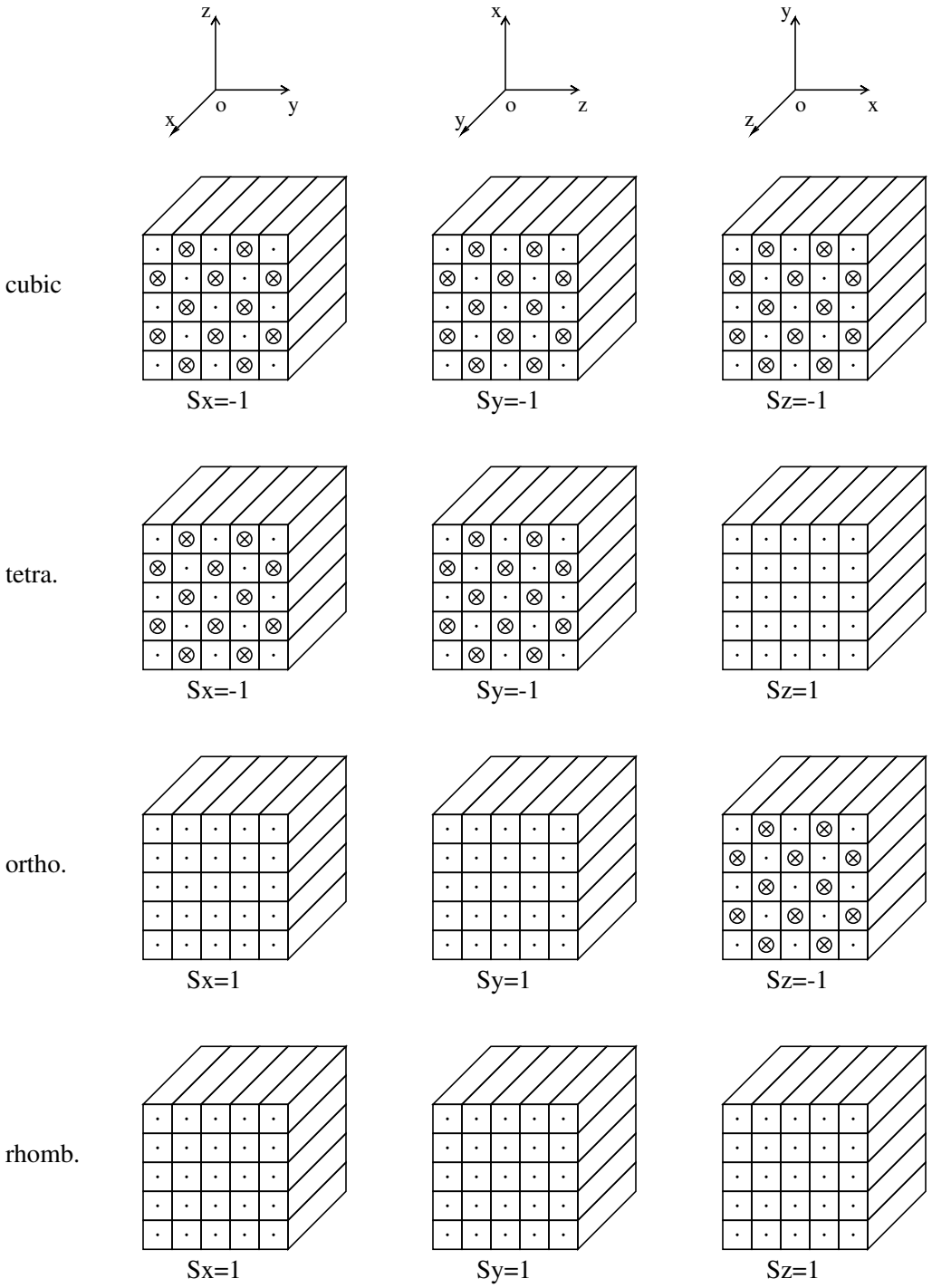

Figure 3.6: The chains in each direction can be ferroelectric or anti-ferroelectric.

Table 3.1: Symmetry and number of atoms in prime cell before and after the antiferroelectric distortion.

Phase	Symmetry 1	N_1	Symmetry 2	N_2
cubic	$Pm3m$	5	$I-43m$	40
tetra.	$P4mm$	5	$I4cm$	40
ortho.	$Amm2$	5	$Pmn21$	10
rhomb.	$R3m$	5	$R3m$	5

Table 3.2: Order Parameter S_x, S_y and S_z.

Phase	S_x	S_y	S_z
$I-43m$	-1	-1	-1
$I4cm$	-1	-1	1
$Pmn21$	1	1	-1
$R3m$	1	1	1

tion. Two neighboring chains can have parallel or antiparallel polarizations, corresponding to ferroelectric or antiferroelectric distortions. In Fig. 3.6, the cubic phase is described by three sets of antiparallel chains, and the rhombohedral phase is composed of three sets of parallel chains. In another word, the polarizations $(P_x,\ P_y,\ P_z)$ at two lattice sites, $(x,\ y,\ z)$ and $(x+dx,\ y+dy,\ z+dz)$, are related by,

$$P_x(x+dx,\ y+dy,\ z+dz) = (S_x)^{dy+dz} P_x(x,\ y,\ z) \tag{3.16a}$$

$$P_y(x+dx,\ y+dy,\ z+dz) = (S_y)^{dx+dz} P_y(x,\ y,\ z) \tag{3.16b}$$

$$P_z(x+dx,\ y+dy,\ z+dz) = (S_z)^{dx+dy} P_z(x,\ y,\ z), \tag{3.16c}$$

where S_x, S_y or S_z is 1 (ferroelectric) or -1 (antiferroelectric). The phase structure is described by $(S_x,\ S_y,\ S_z)$, which is tabulated in Table 3.2.

The chain itself is stable against a single site flip. This stability gives quite long chain correlation length. We performed constant temperature and constant pressure

molecular dynamics (NPT MD) simulations for each phase with super cell of $12 \times 12 \times 12$ at 100 K, 200 K, 300 K, 400 K and 500 K. Each phase keep their chain structures during the whole MD run of 40 ps. This indicates a large thermal hysteresis during phase transition.

If only the chain interaction between the first nearest neighbor is considered and the difference between an FE and AFE interactions is $\Delta F(T)$ per lattice parameter along chain direction, then for two neighboring chains with length of na, the ratio of probability of AFE vs. FE states are $\exp(-\frac{n\Delta F(T)}{k_B T})$. Unless the phase is close to a transition, $\Delta F(T)$ is in the order of meV (Fig. 3.8). $k_B T$ is about 10 to 40 meV. For $n \gg 100$, the free energies of two states are well separated, thus disorder between chains in the so-called order-disorder model is not dominant unless the structure is close to a phase transition.

3.5 Phase Transitions

The phase transitions are studied within the harmonic approximation. We minimize each FE-AFE phase structure and calculate its frozen phonon density of states (Fig. 3.7) with a mesh of $20 \times 20 \times 20$. Then zero point energy (ZPE) correction, energy, free energy and entropy are obtained by Eqs. (3.6), (3.7), (3.8) and (3.9).

The AFE configuration moves the DOS of frozen phonon to lower frequencies. This causes an lower ZPE and higher vibrational entropy than the FE configuration. Table 3.3 shows that the energy stability of FE state is canceled by half with ZPE at 0K. Further entropy effect cause AFE state more stable than FE state with increasing temperature, as show in Fig. 3.8.

The free energies of $BaTiO_3$ four phases are calculated according to Eq. (3.8) and are ploted as functions of temperature in Fig. 3.8, where the rhombohedral phase is take as the reference. From the free energies of the four phases, a correct phase

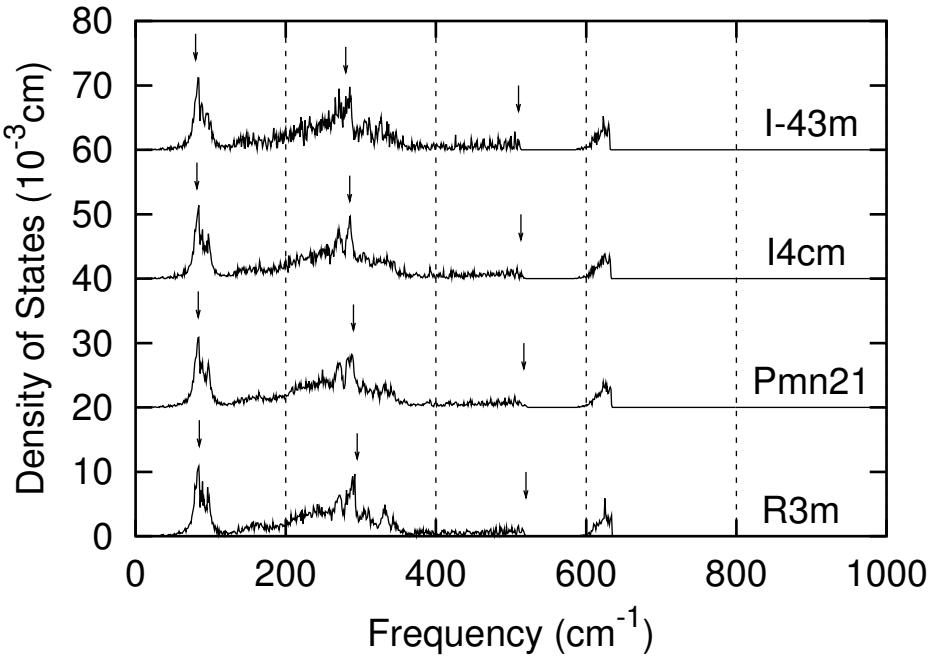

Figure 3.7: Frozen phonon DOS of $BaTiO_3$ FE-AFE phase structures.

transition sequence (R $\rightarrow$ O $\rightarrow$ T $\rightarrow$ C) is obtained and the corresponding phase transition temperatures are determined. Further, transition entropies are calculated from Eq. (3.9) and shown in Fig. 3.9. From these calculations, it is found that each $BaTiO_3$ phase transition is an ferroelectric to antiferroelectric transition in one crystal direction. The phase transition temperatures and entropy changes are summarized in Table 3.4. The phase transition temperatures are close to expemimental values. The first transition entropy is close to experiment. While the other two transition entropies are underestimated in our calculation comparing to experiments. This is partially due to an underestimated transition temperatures and ignoring the anharmonic effects.

3.6 Diffuse Scattering

An interesting property of $BaTiO_3$ is the presence of the diffuse lines along nonpolar direction observed in the inelastic X-ray [16] or neutron diffraction experiments.

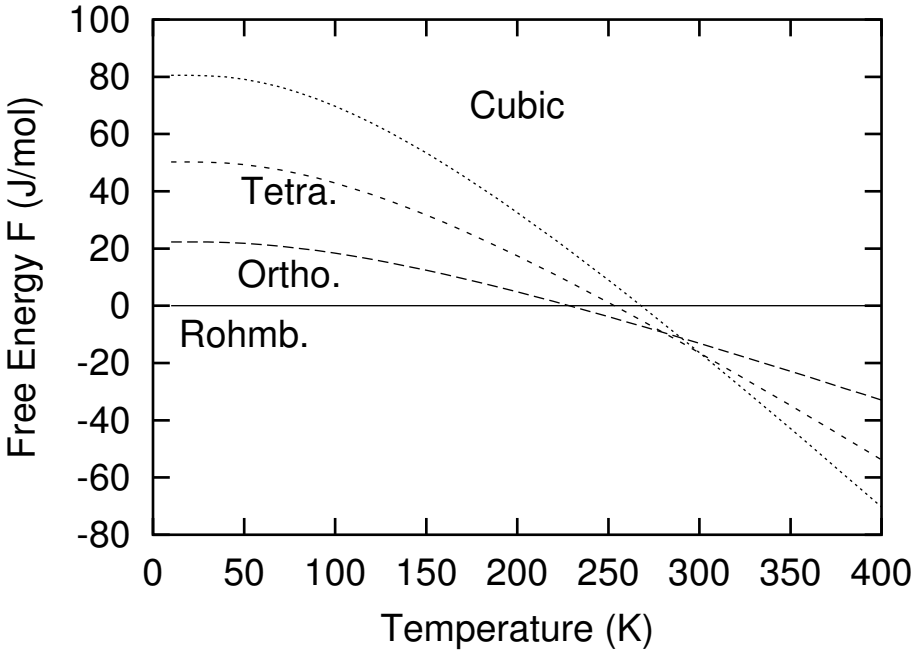

(a) Free energy from 0 K to 400 K

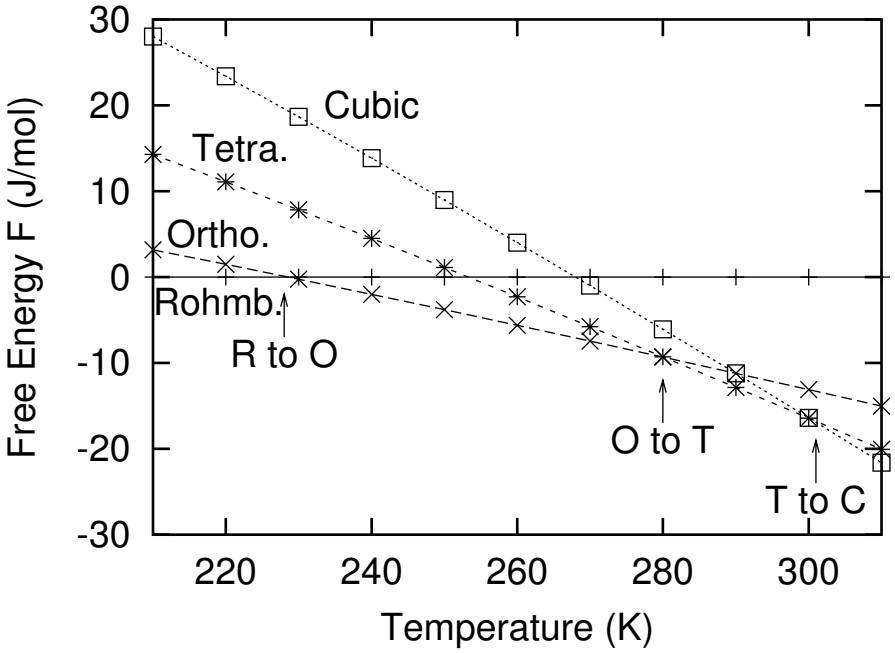

(b) Free energy from 210 K to 310 K

Figure 3.8: Free energies of $BaTiO_3$ calculated from the DOS within the harmonic approximation.

Table 3.3: 0 K energies and ZPE's of $BaTiO_3$ FE-AFE phases (kJ/mol).

Phase	E(0 K)	ZPE	E(0 K)+ZPE
Rhomb.	0	22.78106	22.78106
Ortho.	0.06508	22.73829	22.80337
Tetra.	0.13068	22.70065	22.83129
Cubic	0.19308	22.66848	22.86156

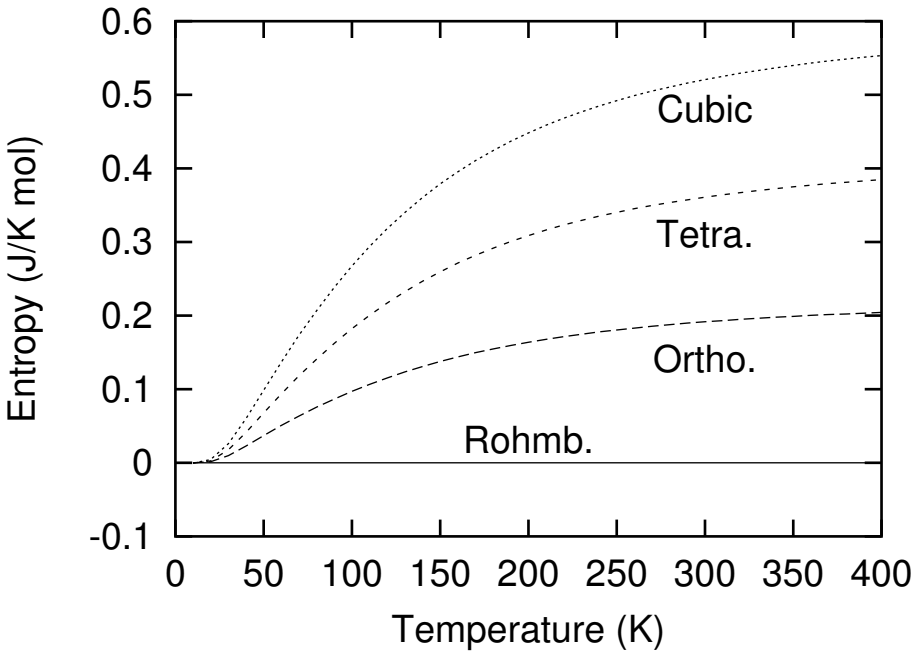

Figure 3.9: Entropies of $BaTiO_3$ calculated from the DOS within harmonic approximation.

Table 3.4: Transition temperature and entropy change of $BaTiO_3$.

Transition	Experiment [68]		This Study	
	T (K)	ΔS (J/mol)	T (K)	ΔS (J/mol)
R $\rightarrow$ O	183	0.17 $\pm$ 0.04	228	0.132
O $\rightarrow$ T	278	0.32 $\pm$ 0.06	280	0.138
T $\rightarrow$ C	393	0.52 $\pm$ 0.05	301	0.145

There are diffuse lines besides the normal Bragg spots in the X-ray diffraction pattern of $BaTiO_3$ cubic phase. Certain series of diffuse lines vanish when $BaTiO_3$ goes through consecutive phase transitions with decreasing temperature. In $BaTiO_3$ rhombohedral phase, such diffuse lines almost vanish. The relation between these diffuse lines and the phase structures attracts a lot of attention. Comes [15] proposed chain structures to explain these diffuse lines in $BaTiO_3$ and $KNbO_3$. He attributed such diffuse lines to the disorder of chains. But such explanation is not consistent with the fact that unexpected weak diffuse lines are observed in orthorhombic phase besides the expected strong diffuse lines. Later Huller [37] argued that these lines are from dynamic structures, i.e., phonon structures. He further proved that dynamic structures of a displacive model can also give such diffuse diffraction lines.

Here we show that such diffuse diffraction lines can come from the dynamic structure of an ordered AFE configuration with anisotropic phonon structures. We calculate the inelastic coherent scattering functions of the four phases as discussed in Section 3.2. For simplicity, we only consider the scattering by Ti atoms.

The scattering functions of all four phases agree well with the diffuse X-ray diffraction experiments [16]. In the (001) zone of $BaTiO_3$ cubic phase (Fig 3.10), two series of very strong diffuse lines along (100) and (010) are observed. These strong diffuse lines are caused by the soft phonons along the crystal axis around the Γ point. In the (010) zone of $BaTiO_3$ tetragonal phase, there are a series of strong diffuse lines along (001) and a series of weak diffuse lines along (100). However, for the orthorhombic phase, such intensity order is reversed. In the (001) zone of $BaTiO_3$rhombohedral phase, the diffuse lines almost vanish. The relative intensities of these diffuse lines in the tetragonal and orthorhombic phases show that the transverse phonons with phonon polarization vectors along the nonpolar directions are stronger than the polar directions. The study shows the phonon structure is highly anisotropic.

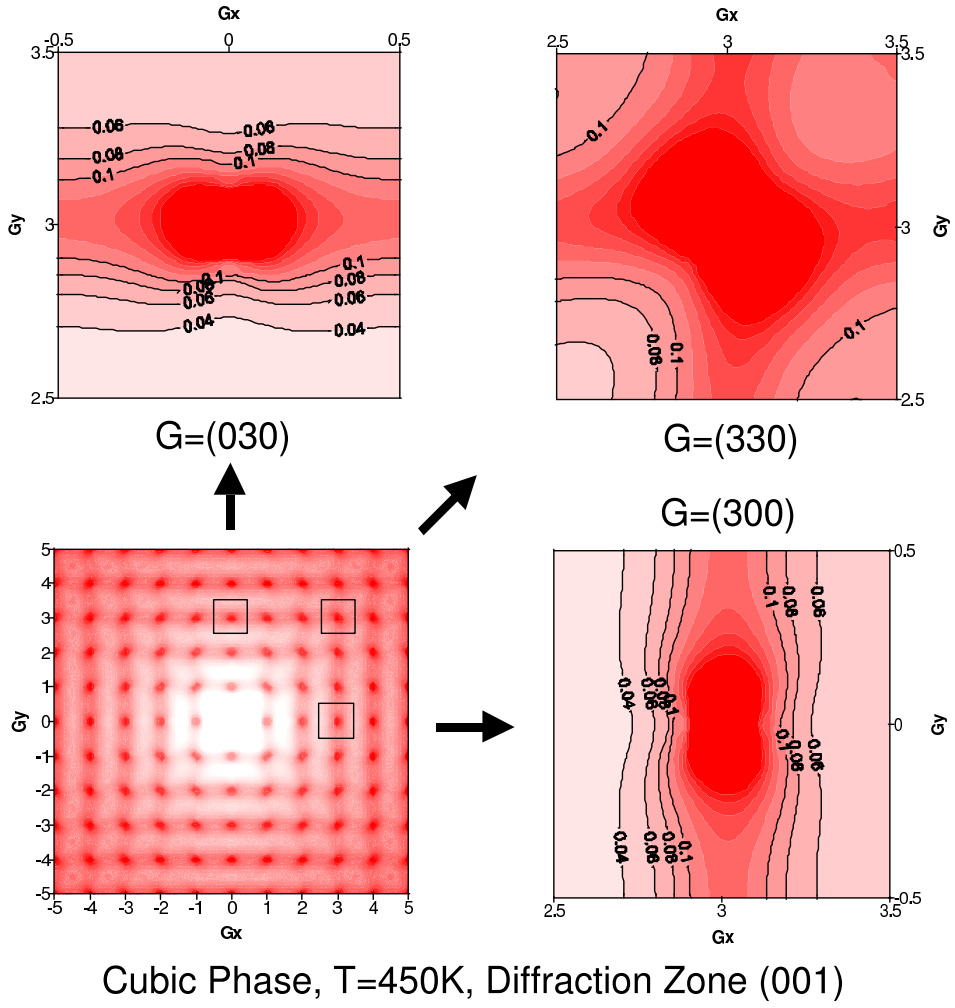

Figure 3.10: Coherent inelastic scattering function of $BaTiO_3$ cubic phase.

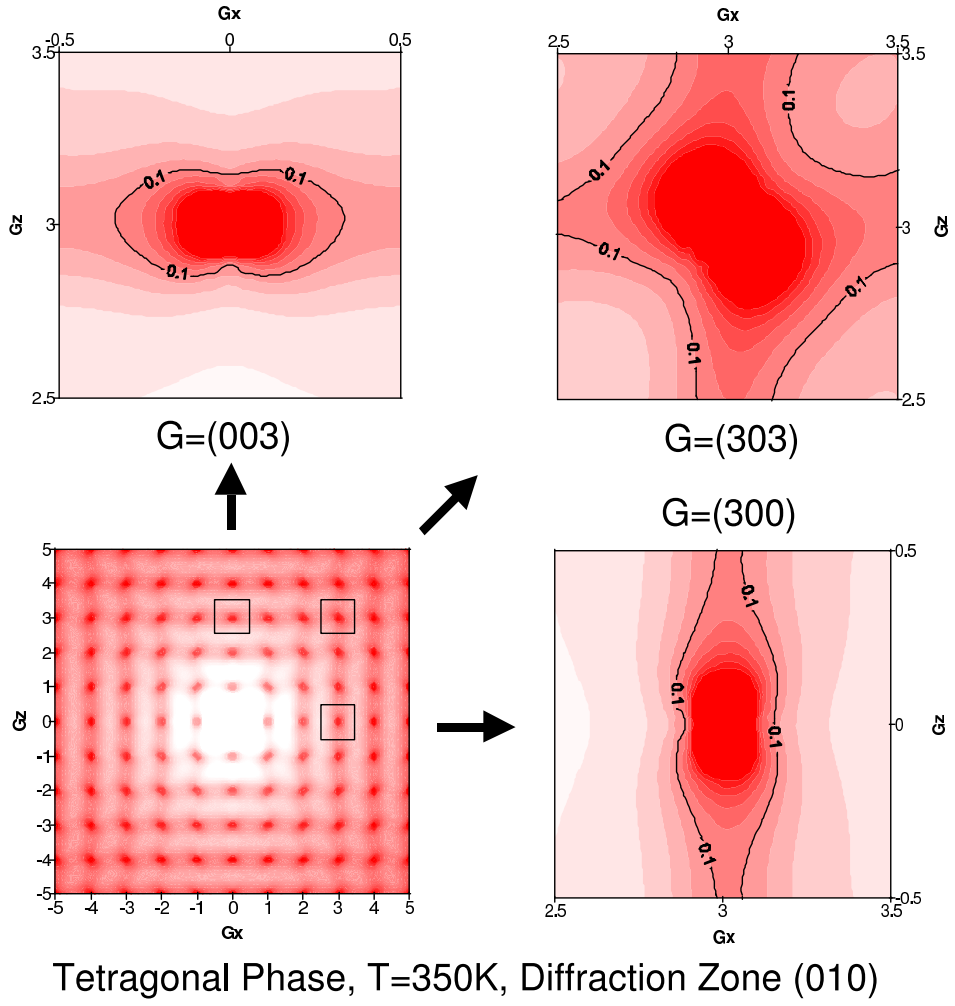

Figure 3.11: Coherent inelastic scattering function of $BaTiO_3$ tetragonal phase.

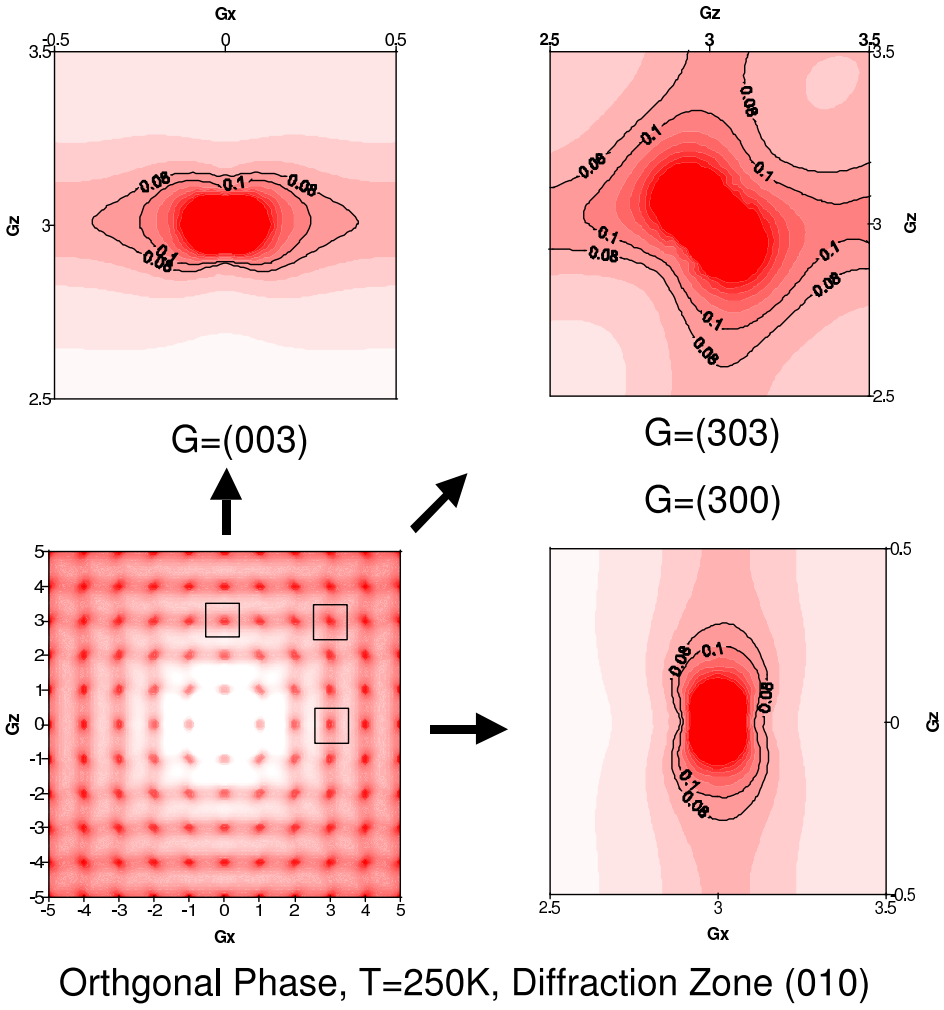

Figure 3.12: Coherent inelastic scattering function of $BaTiO_3$ orthogonal phase.

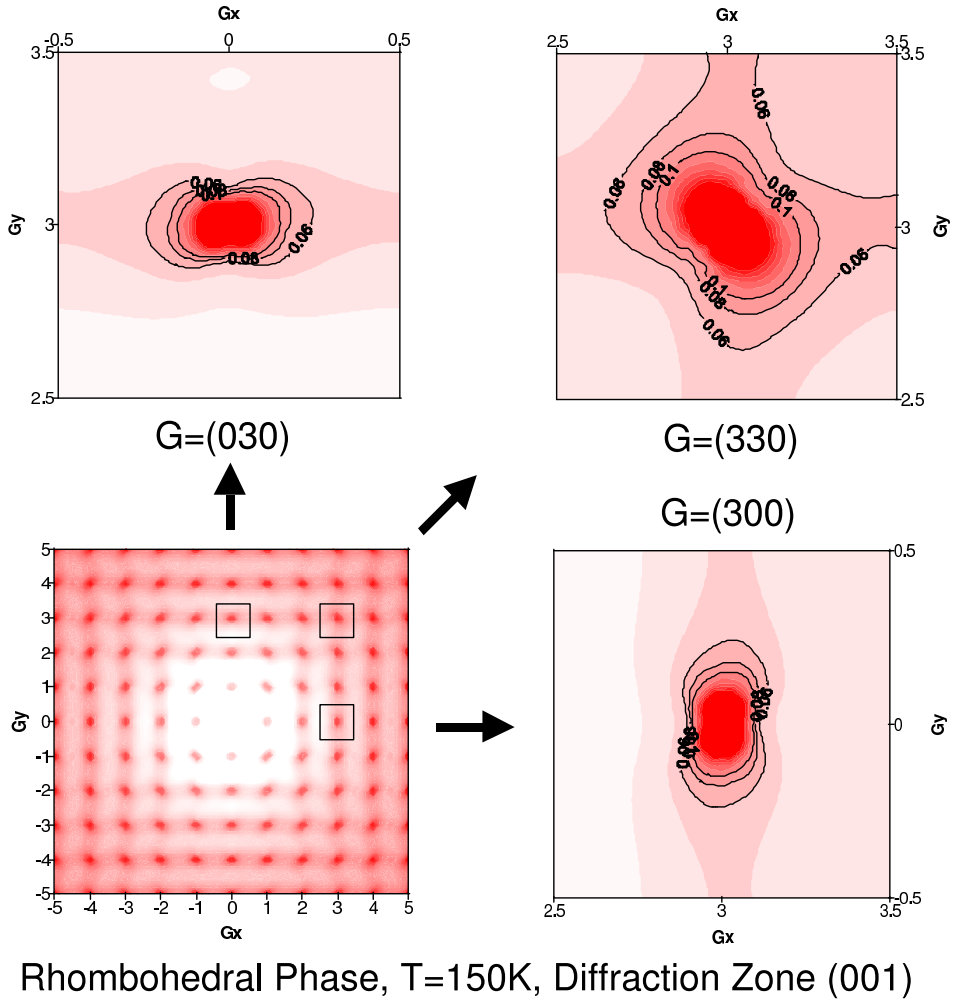

Figure 3.13: Coherent inelastic scattering function of $BaTiO_3$ rhombohedral phase.

Table 3.5: Optical phonon modes at Γ for the four phases in the displacive model. For simplicity, splitting due to long-range force is ignored.

Phase	Mode(Degeneracy)	No.	IR	Raman
$Pm3m$	$F_{1u}(3)$	3	Active	
	$F_{2u}(3)$	1		
$P4mm$	$A_1(1)$	3	Active	Active
	$B_1(1)$	1		Active
	$E(2)(2)$	4	Active	Active
$Amm2$	$A_1(1)$	4	Active	Active
	$A_2(1)$	1		Active
	$B_1(1)$	3	Active	Active
	$B_2(1)$	4	Active	Active
$R3m$	$A_1(1)$	3	Active	Active
	$A_2(1)$	1		
	$E(2)$	4	Active	Active

3.7 Discussion

A major difference from the order-disorder model is that the latter has to assume a certain correlation chain length and chain disorder to explain the small entropy change during phase transitions [15]. We found that is unnecessary; the entropy change during transition can be recovered by the vibrational phonon softening.

Because the inversion symmetry breaks in $I-43m$ group, the phonon are Raman active, which is confirmed by intense Raman spectrum [61] in the cubic phase. The displacive model, in which the cubic phase ($Pm3m$) has a inversion symmetry, contradicts this experiment.

In the tetragonal phase, the vector from the center of oxygen octahedral to the Ti atom, **d** is displaced 5.63 ° from $\langle 111 \rangle$ to $\langle 001 \rangle$ (Fig. 3.14). This is confirmed by the EXAFS experiment [63], where the vector rotates 11.7° in the same direction.

As discussed in section 3.4, with mean field of the remaining sites of a chain, a single site does not have double potential as usually mentioned in ferroelectrics. The double well potential picture should be applied to each chain, corresponding two

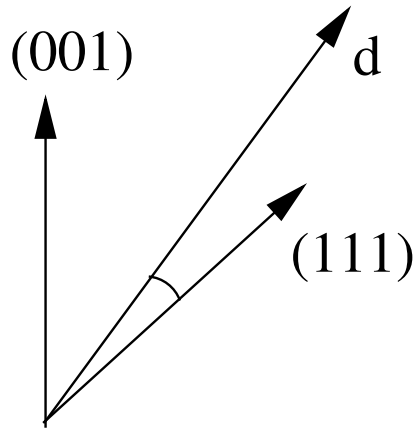

Figure 3.14: The displacement of vector **d** from $\langle 111 \rangle$ to $\langle 001 \rangle$ in the tetragonal phase.

possible polar directions.

3.8 Conclusion

From the observed phonon instability of $BaTiO_3$, we have proposed FE-AFE phase structures of $BaTiO_3$. Each phase transition corresponds to an FE to AFE transition in one crystal direction. We find that the AFE configuration has lower ZPE and higher vibrational entropy than the FE configuration. The long correlation length along AFE chains keeps the AFE in order. The phase sequence, transition temperatures, local and dynamic structures agree with experiments.

These AFE phase structures should help us understand structures of domains, oxygen vacancies and surface. The application of the above approach should also be applicable to ABO_3 perovskite materials like $KNbO_3$.

Chapter 4

Domain Walls

4.1 Introduction

$BaTiO_3$ tetragonal phase is stable at room temperature. In this phase, 180° and 90° domain walls (Fig. 4.1) were observed by Kay and Louden [40], Forebear [24], Merz [53, 55], and Little [49]. These domain walls attract great interest in technological applications. The switching of the 180° domain is used in ferroelectric memory to store information [2], and the 90° domain switching is used to achieve large displacement.

These domain walls also draw a lot of attention since they are related to the properties in applications. $BaTiO_3$ subjects to long-term effects,

- fatigue, the decrease of the ferroelectric polarization upon continuous large-

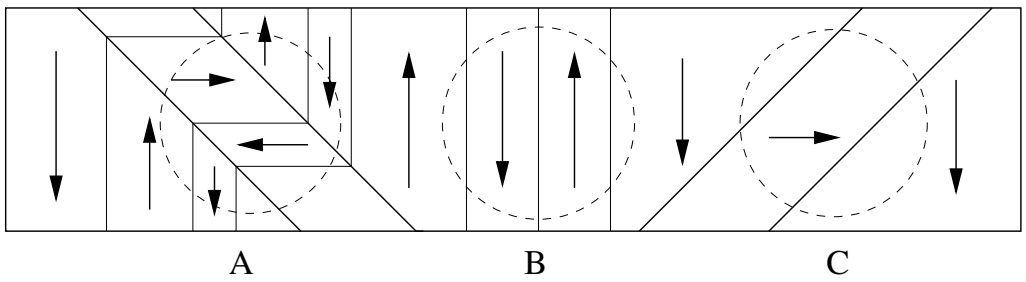

Figure 4.1: Domain walls in $BaTiO_3$ tetragonal phase. (a) A mixture of 90° and 180° domain walls; (b) 180° domain wall; (c) 90° domain wall .

signal cycling,

- retention loss, the decrease of the remnant polarization with time,
- imprint, the preference of on polarization state over the other,
- aging, the polarized material trying to relax to its prey-poled state.

Generally, these long-term effects are considered major failure mechanisms. It is argued that the domain wall pinning by charged defects within the bulk of the crystal attributes to such effects.

The energy and thickness of $BaTiO_3$ 180° domain walls were studied with various methods. Merz [55] modified the well-known model of the Bloch wall in ferromagnet's for the case of $BaTiO_3$. He found a the 180° domain wall to be one lattice constant wide and 7 erg/cm^2. Kinase *et al.* [42, 43] did dipole field calculations and estimate that the energy of $BaTiO_3$ 180° domain wall is about 1.4 erg/cm^2. Padilla *et al.* applied the Monte Carlo method with effective Hamiltonian to $BaTiO_3$ 180° domain wall, and reported an energy of 15 to 17 erg/cm^2. They gave an thickness of 1.4 unit cell [58]. In all of the above calculations, a detailed atomic structure is missing. Besides, the two walls in the effective Hamiltonian [58] calculation are separated by only 8 nm, which is too small.

A molecular treatment of the 90° wall is not available to date. The problem is much more complicated than for the 180° wall because the lattice distortion at the wall involves a noticeable contribution of elastic energy. Moreover, the spontaneous polarization may change its direction gradually. In experiments, Little [49] estimated the thickness of 0.4 um from his direct optical observation. However such a visual estimation may easily be affected by the reflection of the light at the boundary.

In this paper, we study the two types of domain walls with the P-QEq force field. The force field describe charge transfer and electronic polarization in an self-consistent way. Parameters are optimized from a first-principles DFT/GGA calculation. We find

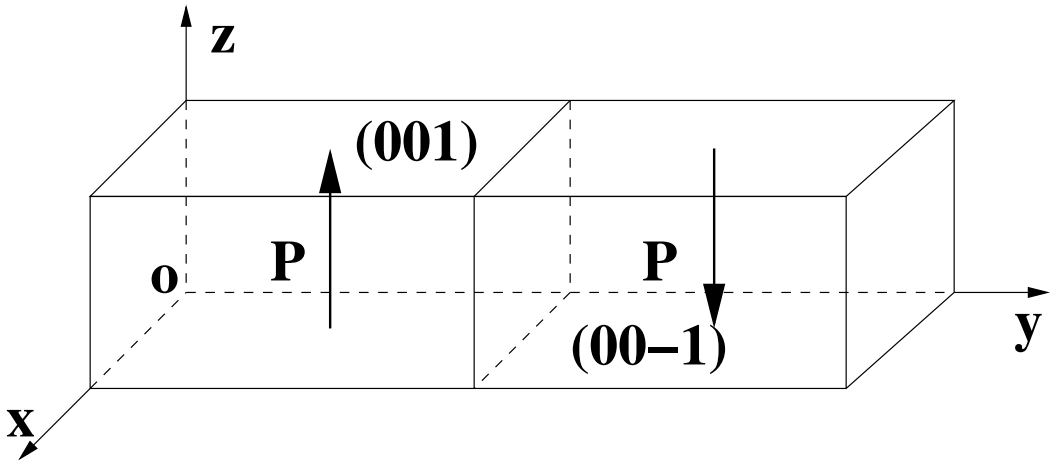

Figure 4.2: 180° domain wall.

that there are layered structures in both walls and the 90° domain wall is strongly charged.

4.2 180° Domain Wall

A $2 \times L \times 2$ super cell of tetragonal phase is used in this calculation. In the right half of the super cell, the z component polarization is flipped by moving Ti atoms downward (Fig. 4.2). The forces and stresses of the super cell are minimized to obtain a stable 180° domain wall.

The domain structures and energies σ are studied as a function of domain modulation period L, where $L = 2^m$ and $m = 1, 2 \ldots 10$. For $64 \leq L \leq 1024$, the domain wall has three layers from the wall center to the domain center (Fig. 4.4):

- Wall center: polarization and displacements switch abruptly on the wall. The atomic displacements are antisymmetric to the center Ba atom.

- Transition layer: polarization converges quickly from the wall center to domain, whereas the atomic displacements take a long distance to relax. In this layer, the regions close to wall center are slightly expanded in y direction while the

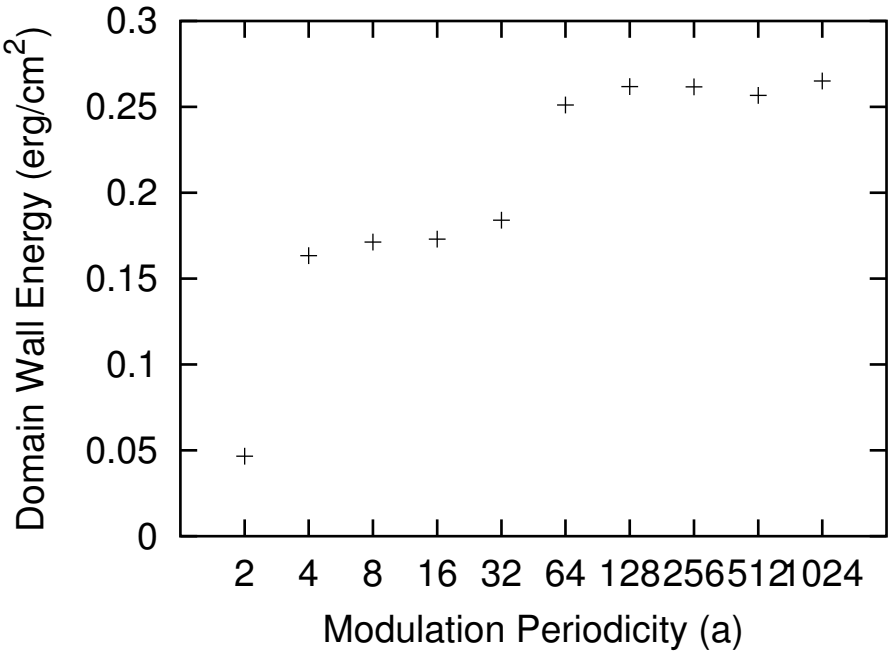

Figure 4.3: $BaTiO_3$ 180° domain wall energies.

remaining regions are slightly contracted in that direction. This layer is about 6 nm for L=512. This means that the domain size is too small in the effective Hamiltonian calculation [58].

- Domain structure: both polarization and atomic displacements are converged and constant.

For $4 \leq L \leq 32$, only the wall center and the transition layers appear. For $L = 2$, we can see polarization switching between neighboring unit cells. This is in fact an antiferroelectric structure in the modulation direction.

The domain wall energies also show such transitions. In the Fig. 4.3 there are three segments corresponding to the above three types. The three types of domain structures have domain wall energies of 0.05, 0.17 to 0.19, and 0.26 to 0.30 erg/cm^2.

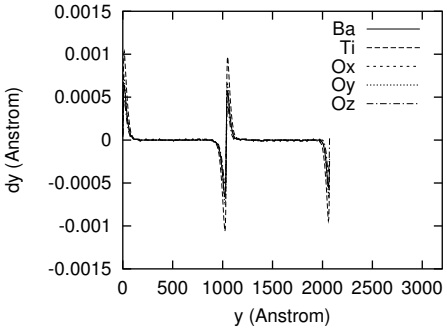

(a) Atomic displacement dY.

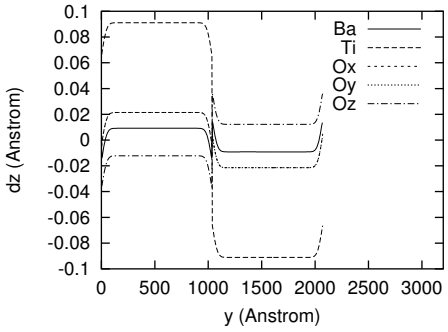

(b) Atomic displacement dZ

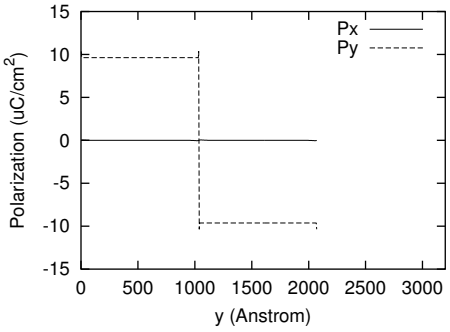

(c) Polarization P_y and P_z.

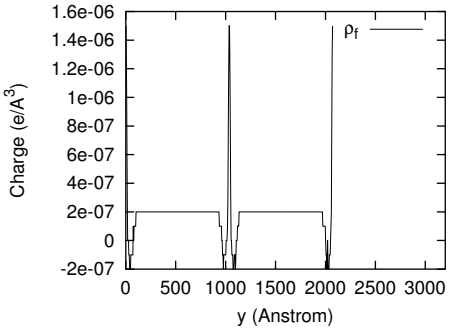

(d) Free charge density ρ_f.

Figure 4.4: Structure of the $BaTiO_3$ 180° domain wall with $L = 512$.

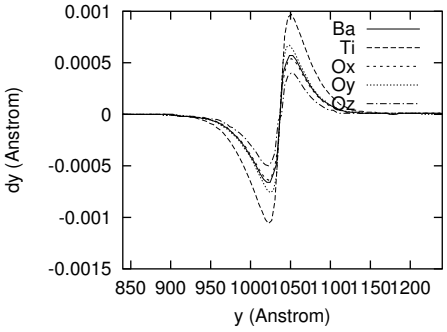

(a) Atomic displacement dY.

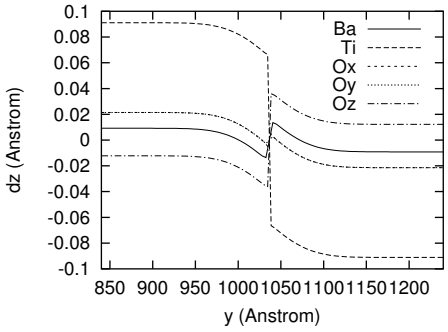

(b) Atomic displacement dZ

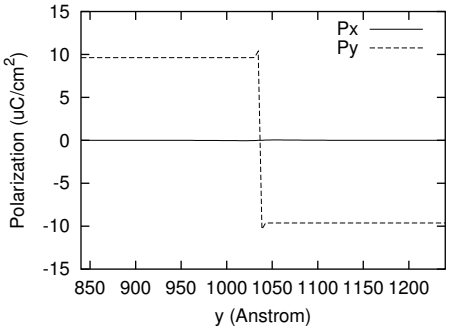

(c) Polarization P_y and P_z.

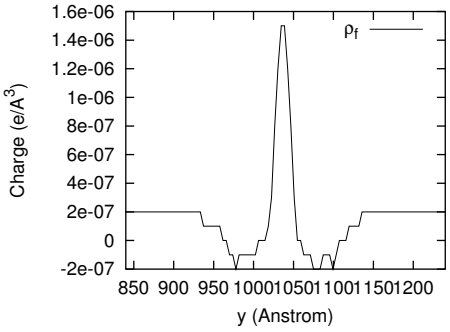

(d) Free charge density ρ_f.

Figure 4.5: Local structure around the $BaTiO_3$ 180° domain wall with $L = 512$.

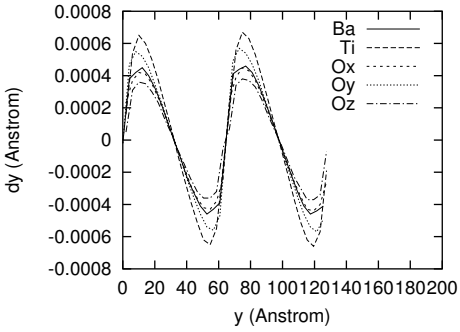

(a) Atomic displacement dY.

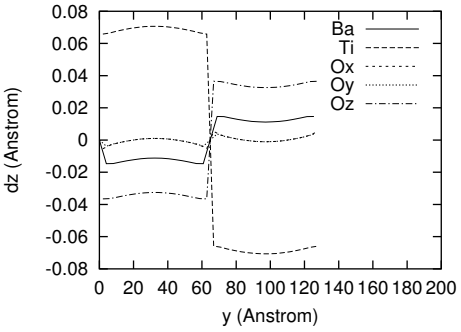

(b) Atomic displacement dZ

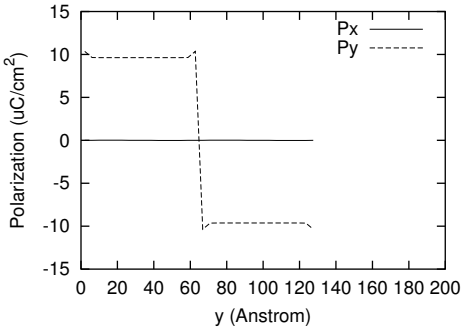

(c) Polarization P_y and P_z.

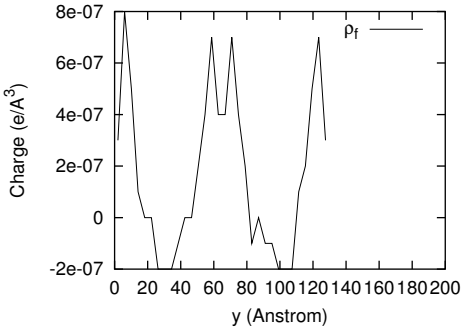

(d) Free charge density ρ_f.

Figure 4.6: Structure of the $BaTiO_3$ 180° domain wall with $L = 32$.

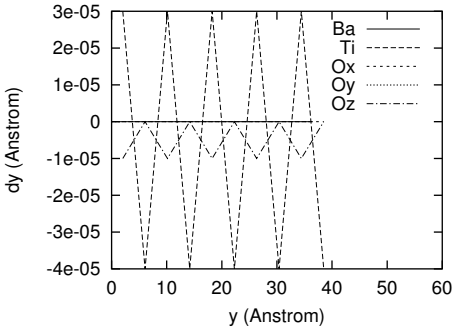

(a) Atomic displacement dY.

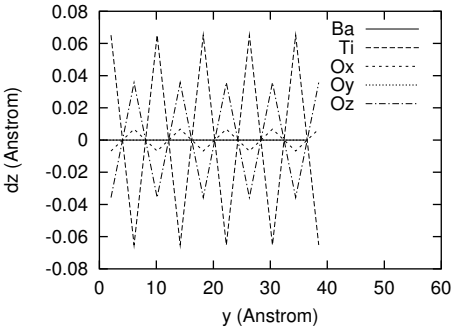

(b) Atomic displacement dZ

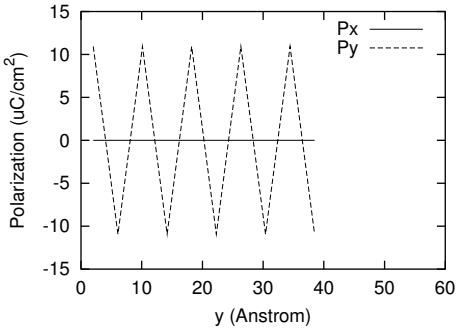

(c) Polarization P_y and P_z.

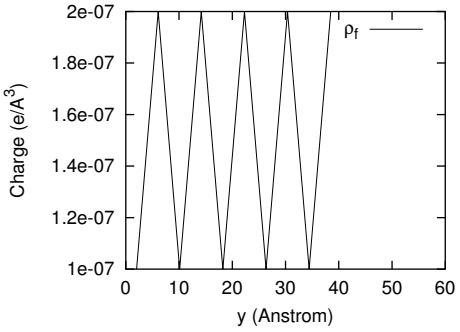

(d) Free charge density ρ_f.

Figure 4.7: Structure of the $BaTiO_3$ 180° domain wall with $L = 2$.

4.3 90° Domain Wall

Polarization change across the domain wall induces polarization charge,

$$\nabla \mathbf{P} = \rho.$$

Thus the configuration of 90° domain usually form a head-to-tail structure in order to avoid discontinuities in the polarization at the domain boundary.

We start from a cubic phase super cell of $2 \times 2L \times 2L$ and switch the polarization in y-z plane in an zig-zag pattern (Fig. 4.8). Then we redefine the super cell along $\langle 100 \rangle$, $\langle 011 \rangle$ and $\langle 0\bar{1}1 \rangle$ and rotate it anti-clockwise for 90°. The new defined super cell has a small size of $2 \times \sqrt{2}L \times 2\sqrt{2}$. In the new defined super cell, the polarizations are along $\langle 010 \rangle$ and $\langle 0\bar{1}0 \rangle$ in the left and right part, respectively. A 90° domain wall structure is obtained by fully minimizing the forces and stresses of the super cell.

For $L < 64$, the super cell changes into an orthogonal phase during minimization; the 90° domain wall is stable only for $L > 64$. Fig. 4.9 shows a layered structure of the 90° domain wall with L=128. The corresponding domain wall energy is about 0.67 erg/cm^2. The wall center layer is about 2 nm with a structure similar to the orthogonal phase. The polarization aligned to $\langle 0\bar{1}1 \rangle$ crystal direction. Besides the center layer there are two opposite charged transition layers of about 5 nm. These transition layers bridge the tetragonal structure in the domain and the orthogonal structure at the wall center. The center and the transition layers have a larger lattice spacing in the direction perpendicular to the wall than the domain.

4.4 Polarization Charge and Free Charge

The polarization change cause macroscopic charge, i.e., polarization charge. Beside, there is free charge transfer between atoms. We found both effects in the 180° and 90°

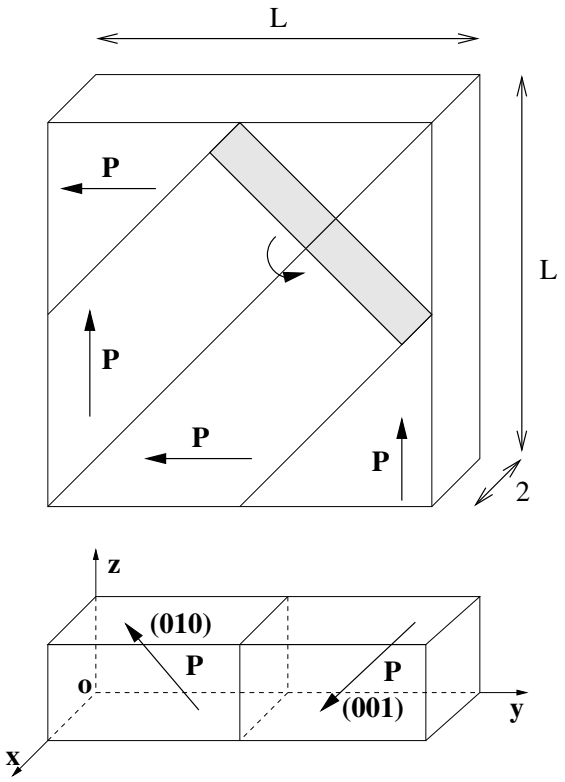

Figure 4.8: 90° domain wall.

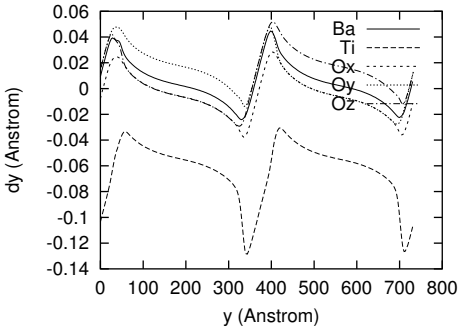

(a) Atomic displacements dY

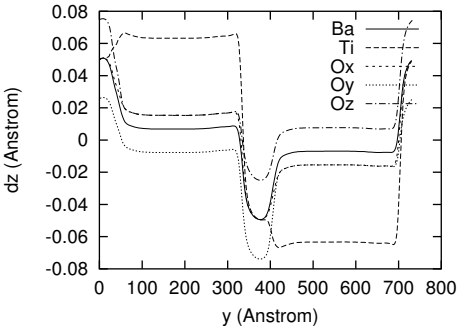

(b) Atomic displacement dZ.

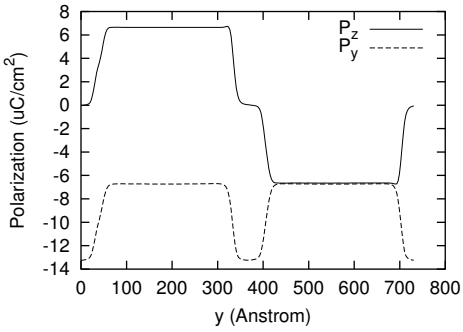

(c) Polarizations P_y and P_z

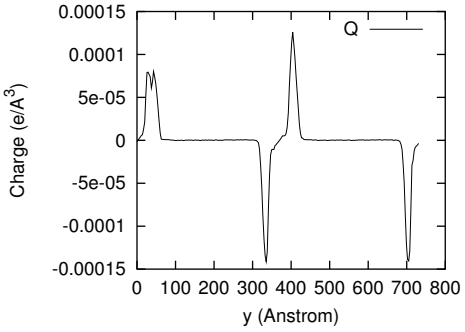

(d) Free charge density ρ.

Figure 4.9: Structure of the $BaTiO_3$ 90° domain wall.

domain wall structures. We found that free charge transfers in both wall structures to compensate the heterogeneous polarization charge.

In the 180° domain wall (Fig. 4.4), the polarization charge and free charge have symmetric structures about the domain wall center. Polarization charge is negative at wall center and positive in the transition layers. After partial neutralization from charge transfer, the center is slightly negative charged.

The charge density has an antisymmetric structure in the 90° domain wall (Fig. 4.9). The center of 90 ° domain wall has a structure similar to the orthogonal phase. Since the orthogonal phase has a much larger polarization component along the ⟨011⟩ direction than the tetragonal phase, large free charge redistribution is observed in the 90° domain wall.

Both the polarization change density ρ_p and free charge density ρ_f contribute to the macroscopic electric fields.

Under the periodic boundary condition, the electrostatic potential U of the $BaTiO_3$ 90° domain wall is a function of y. Thus the general 3-D problem is reduced to the following 1-D equation set,

$$\frac{d^2U}{dy^2} = -\frac{\rho}{\epsilon_o}, \tag{4.1}$$

$$\rho = \rho_p + \rho_f, \tag{4.2}$$

$$\frac{dP}{dy} = -\rho_p, \tag{4.3}$$

with the boundary condition $U(0) = U(\sqrt{2}L)$. Here, the first equation is the Poisson's equation. The solution to Eq. (4.1) is

$$U(y) = \frac{1}{\epsilon_o}\left(\int_0^y P(\xi)d\xi - \int_0^y \int_0^\xi \rho_f(\eta)d\eta d\xi\right) + Cy, \tag{4.4}$$

where C is a constant to match the periodic boundary condition. The solution is

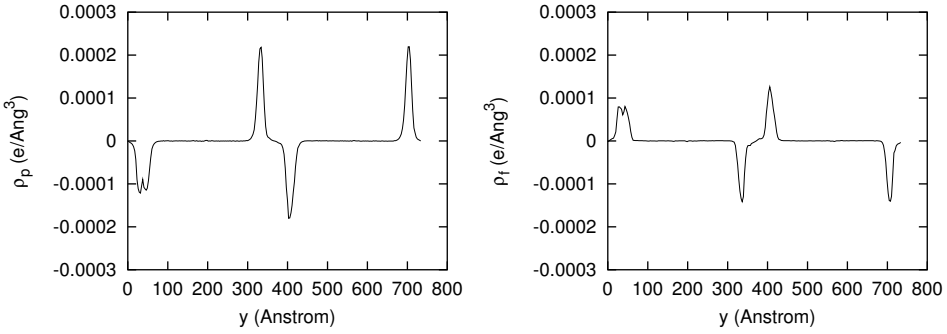

(a) Polarization charge density ρ_P.

(b) Free charge density ρ_f.

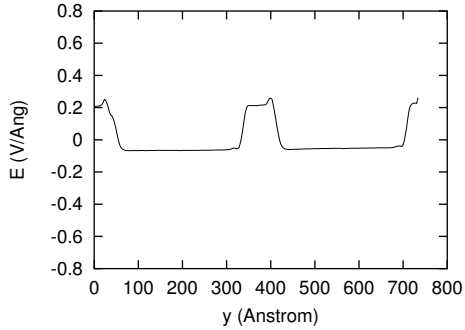

(c) Electric Field E

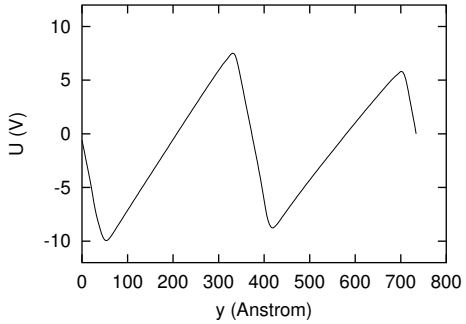

(d) electric potential U.

Figure 4.10: Polarization and free charges at the $BaTiO_3$ 90° domain wall.

shown in Fig. 4.10.

The transition layers have strong polarization charge density due to the polarization difference between the wall center and the domain. However a free charge transfer in the opposite direction cancels most of this polarization charge. This effect cause a strong bipolar structure around the wall, which attracts and traps charged defects at the transition layers (Fig. 4.10). A relative smaller effects is also found in the 180 ° domain wall.

Fig. 4.10 shows that a strong bipolar structure at the 90° domain wall, with the electric field of about 0.2 V/Å. These strong local fields can cause redistribution of charged point defects. It can be a possible reason for the retention loss, imprint and

aging. During cycling, the domain walls transport point defects while sweeping the crystal. These point defects further reduce the mobility of the domain walls, causing electric fatigue.

4.5 Discussion

The domain wall energies and structures of $BaTiO_3$ are quite different from those of $PbTiO_3$ calculated by Meyer *et al.* [56]. They reported a larger domain wall energy for the 180° wall than for the 90° domain wall. Furthermore, they found a decrease of polarization perpendicular to the domain wall at the wall center. One possible reason for the differences is that the structure and energy difference between cubic and tetragonal phases in $PbTiO_3$ are much larger than in $BaTiO_3$. The 180° domain wall can be treated as a mixture of the two phase, thus the 180° domain wall has a much larger wall energy and width in the former. As for the 90° domain wall, $BaTiO_3$ has a stable orthogonal phase in its phase sequence, so the domain wall takes a transition layer similar to orthogonal phase. In the orthogonal phase, polarization perpendicular to the wall is larger that the polarization component of the tetragonal phase. In $PbTiO_3$, such an orthogonal phase is not stable and does not appear in its phase diagram. Thus a direct polarization transition is favored in $PbTiO_3$.

4.6 Conclusion

In this chapter, we analyzed the structures of both 180° and 90° domain walls of $BaTiO_3$. The 180° domain wall is symmetrically charged with wall center being negatively charged. The 90° domain wall is antisymmetrically charged with opposite charges in the transition layers besides the center. These charged structures are important to understand the deterioration of the ferroelectric properties.

Chapter 5

Oxygen Vacancies

5.1 Introduction

Ferroelectric perovskites are promising materials for nonvolatile memory applications. Ferroelectric memories have comparable read and write access-time with the most fast flash memories, and their overall energy efficiency is one thousand times higher [67] than flash memories. A major problem in commercialization of ferroelectric memories is polarization fatigue, the decrease of switchable polarization during normal operation conditions.

The polarization fatigue is attributed to the accumulation of defects in the materials. A lot experiments have been carried out to study the mechanism of this process. One proposed mechanism is near-by-electrode charge injection [57], where electrons and holes injected from the electrodes into the ferroelectric film are trapped at deep levels in a so-called passive layer and cause a simple charged defect. The existence of such passive layers have been confirmed via the size effect of thin films in experiments [70]. However the fatigue process given by such mechanism is not plausible [69].

Another popular mechanism [22, 17, 18] is the oxygen vacancy redistribution mechanism. This mechanism attribute the reduction of switchable polarization to the oxygen vacancy concentration. It is supported by the positive donor doping ef-

fects [9], improved polarization fatigue by oxide electrode [1], and observed oxygen redistribution by Auger analysis [65]. Dukie *et al.* [22] modeled this mechanism by Monte Carlo simulation. The model predicts three regimes of fatigue - a rapid decay to equilibrium (about 10^6 cycles), followed by a long plateau of constant P_s (about 10^8 cycles), and finally a logarithmic or more rapid degradation. Besides it also predicts the frequently observed shorting. The oxygen vacancy mechanism was later generalized into an analytic expression by Dawber *et al.* [17, 18]. He *et al.* found a favorable pinning energy of oxygen vacancy to the 180° domain wall in $PbTiO_3$ by a density functional theory calculation.

However, there are unclear physics in the above oxygen vacancy models. The first is the transition barrier for the oxygen vacancy diffusion. This determine the kinetics of polarization fatigue and are important in applications. The second is the interaction between these oxygen vacancies. Such interactions are simplified in the Duke's model [22] without a proof. In this paper, we address the two questions in $BaTiO_3$.

5.2 Vacancy Energy and Transition Barrier

Oxygen vacancies in $BaTiO_3$ tetragonal phases can occupy two types of oxygen positions, where two neighboring Ti atoms are perpendicular or parallel to the polarization direction z, respectively. The two types are refereed as V_x (V_y) and V_z in this paper. Correspondingly the transition states between two neighboring V_x and V_y states, and neighboring V_x and V_z are called TS_{xy} and TS_{xz}, respectively.

We calculated all these states with P-QEq force field within a $4 \times 4 \times 4$ super cell. V_x, V_y and V_z are fully minimized with both forces and stresses. Transition states are found by a local Hessian method, with zero forces and stresses. Zero point energy and entropy effect are considerable small compared to the barrier. They are ignored

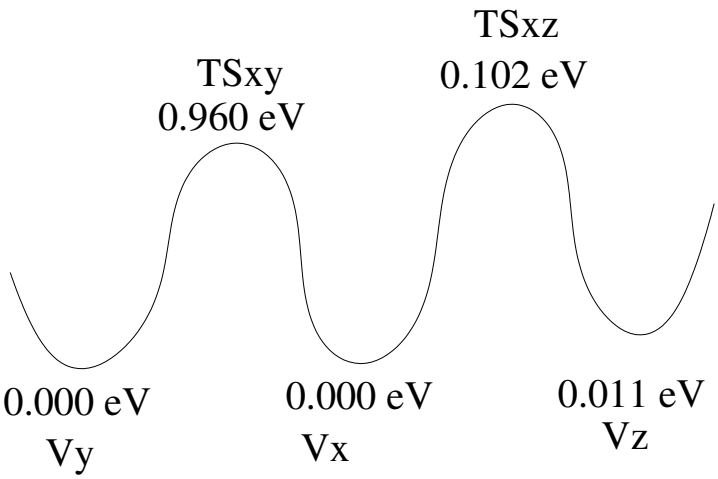

Figure 5.1: Energy profile of oxygen vacancy in $BaTiO_3$ tetragonal phase.

in the calculations.

The calculations (Fig. 5.1) showed that oxygen vacancies prefer the V_x and V_y sites over V_z sites by 0.01 eV. The transition barriers ΔE between two neighboring V_x states is 0.96 eV. This barrier is close to the oxygen vacancy barrier 1 eV in $SrTiO_3$ [74].

For the diffusivity, here we consider a simple case of random walk in the x-y plane. The diffusivity is given by

$$D = \frac{\gamma_o a^2}{2} \exp(-\frac{\Delta E}{k_B T}),$$

where γ_o is the attempt-to-jump frequency and a is the lattice parameter. In $BaTiO_3$, γ_o is between 3 to 20 THz. We take the value of 10 THz. The mobility is given by the Einstein relationship,

$$\mu = \frac{Dq^*}{k_B T},$$

where q^* is the charge of oxygen atom (-1.30 from P-QEq).

Figs. 5.2 and 5.3 show the calculated diffusivity and mobility. At $T = 300$ K, oxygen vacancies are almost frozen with a diffusivity of 6.3×10^{-3} $Å^2$/s and a mobility of 0.3 $Å^2$/sV. Around the Curie temperature (393K), D and μ increase by 10^4, the

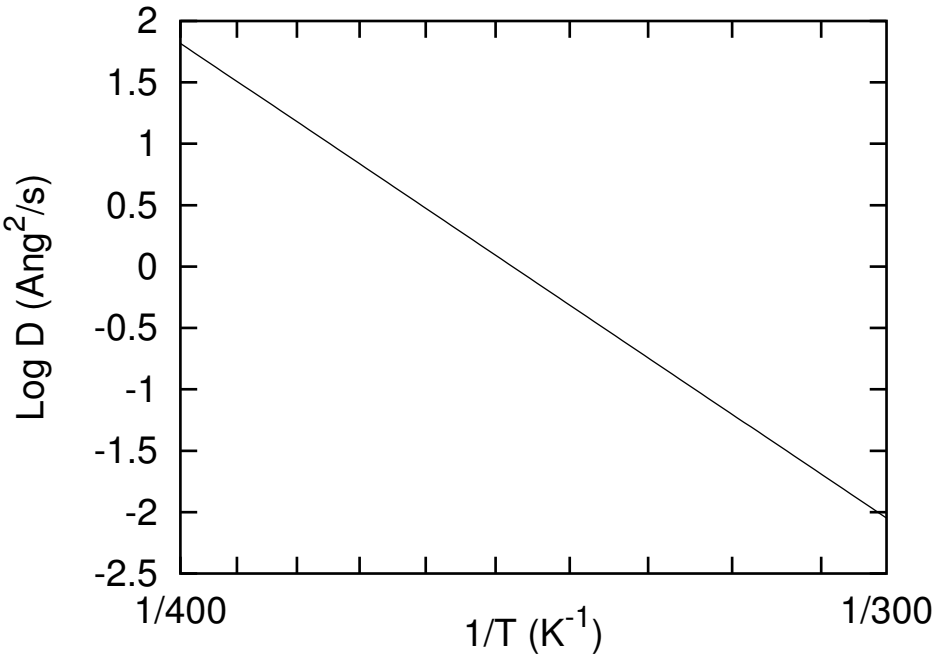

Figure 5.2: Oxygen vacancy diffusivity (d) in $BaTiO_3$ tetragonal phase.

oxygen vacancies are mobile. This is consistent with the fast aging effect just below the transition temperature [64].

The oxygen vacancy is accompanied by large relaxations of local forces and stresses. Here we minimize a perfect crystal with forces and stresses, remove a oxygen atoms, and calculate the energy E_1. Then we relax both forces and stresses of that structure and calculate the energy E_2. The energy difference, $E_1 - E_2$, is defined as relaxation energy ΔE_{rlx}. The relaxed structure is shown in Fig. 5.4. The polarization of the lower part of the chain switches. Short and long bonds in the lower part change to their opposite. The local relaxation causes two neighboring Ti atoms move backward and the distance between them changes from 4.05 Å to 4.44 Å; the polarization along the broken chain switches from head-to-tail to the tail-to-tail configuration at the oxygen vacancy position. A large relaxation energy, 1.52 eV, makes the chain difficult to switch.

The polarization reduction due to the oxygen vacancy is calculated. We calculated

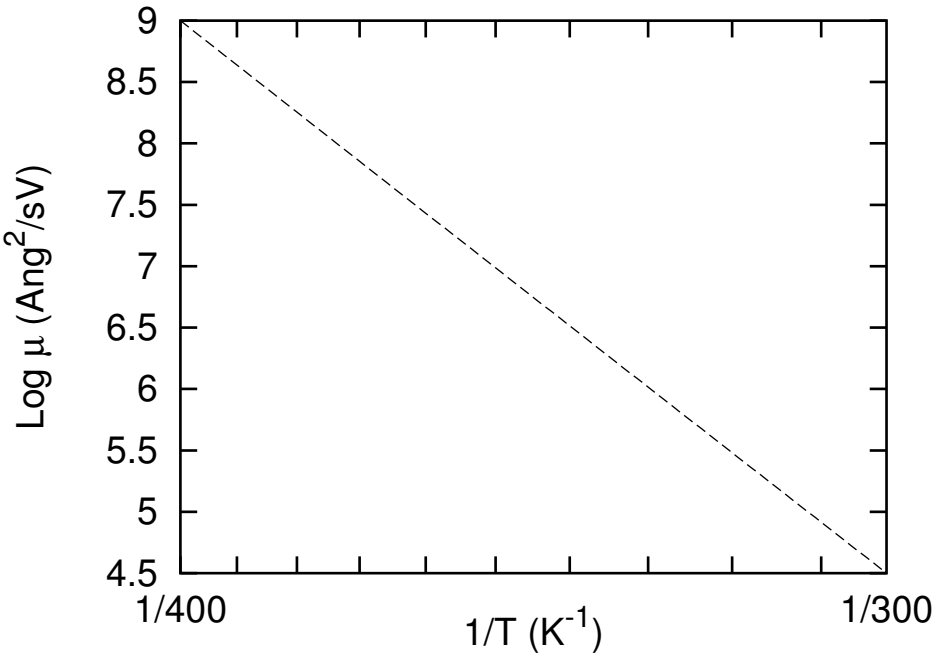

(a) Mobility

Figure 5.3: Oxygen vacancy mobility (μ) in $BaTiO_3$ tetragonal phase.

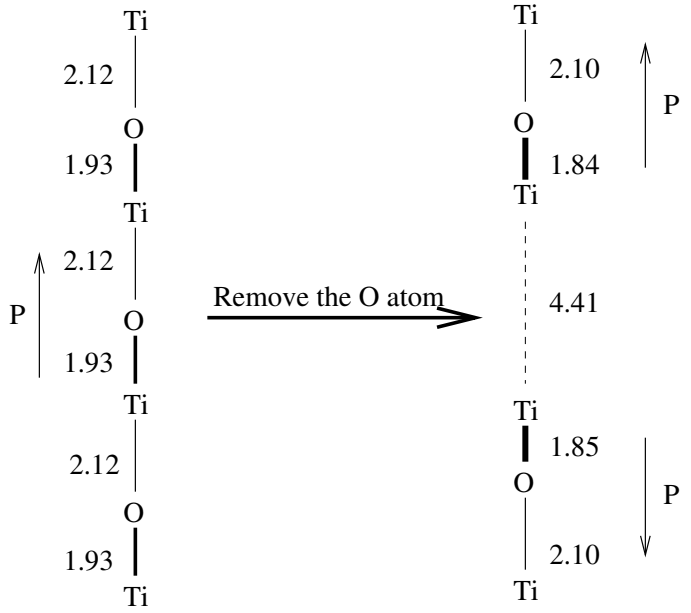

Figure 5.4: Oxygen vacancy structure (unit Å).

the polarization difference between two opposite polarization state (up and down) for the V_z vacancy within a super cell of $4 \times 4 \times 4$. The vacancy causes a reduction of 7.07% in the switchable polarization: the broken chain among 16 chains is frozen and not switchable.

5.3 Oxygen Vacancy Pair

The oxygen vacancies are positively charged. However during cycling, these defects can be concentrated by electric field or domain wall switching. At higher concentrations, the defects have a preference to associate with each other to minimize the lattice energy. The network is thus rearranged.

We first analyze the interaction energy of a oxygen vacancy pair. The distance from Vacancy 1 (V_1) to Vacancy 2 (V_2) is referred by the vector ($dX,\ dY,\ dZ$) in units of lattice parameters, as is shown in Fig. 5.5, where V_1 is fixed at a V_x site. The interaction between a V_x and a V_y in an (001) plane is calculated in a $8 \times 8 \times 4$ super cell. Table 5.1 gives the interaction energy of vacancy pairs. The reference state is (4,4,0), where all vacancies distributed evenly. The highest two energy configurations are $(1,\ 0,\ 0)$ and $(2,\ 0,\ 0)$, where two vacancies align in one chain. The next two high energy configurations are $(\frac{1}{2},\ \frac{1}{2},\ 0)$ and $(\frac{1}{2},\ 0,\ \frac{1}{2})$, where two vacancies share a Ti atom.

It is interesting to find that configuration $(0,\ 1,\ 0)$ is of very low energy (Fig. 5.6). This is a configuration of two V_x vacancies separated by a in the y direction. Further, $E(0,\ 1,\ 0) < E(0,\ 2,\ 0) < E(0,\ 3,\ 0)$ and it means that such two V_x vacancies are attractive along (010) direction. Thus a divacancy structure with broken chains aligned parallel is stable. This stability is helped by a large local energy relaxation (Table 5.2). The single and double $Ti - O$ bond in $O = Ti(OH)_2$ are 1.83 Å and 1.62 Å, respectively. The average $Ti - O$ bond in $BaTiO_3$ is about 2 Å. Thus removing

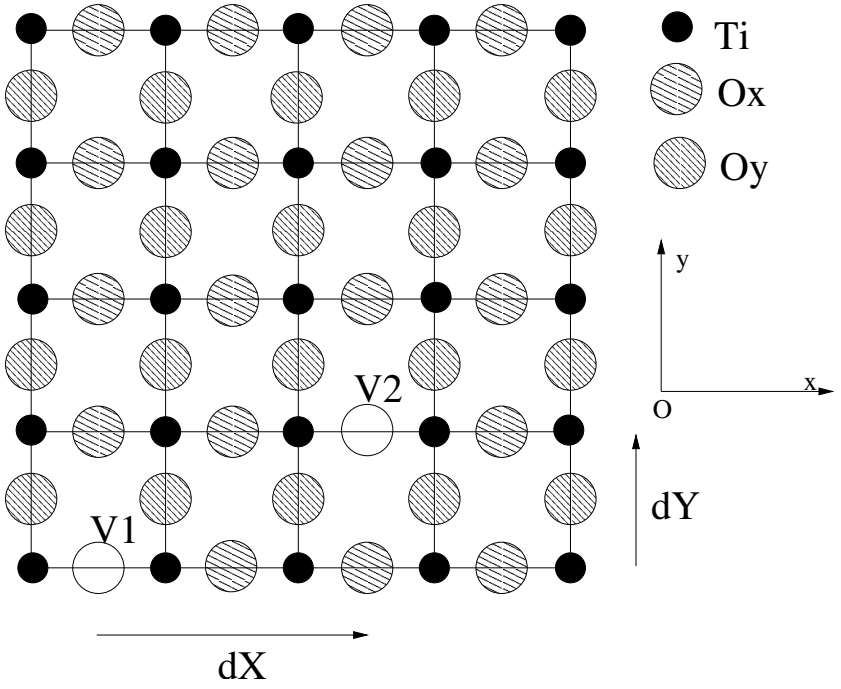

Figure 5.5: Schematic diagram of an oxygen vacancy pair in the x-y plane.

an O atom from the $-\mathrm{Ti}-\mathrm{O}-\mathrm{Ti}-$ chain relaxes the neighing $\mathrm{Ti}-\mathrm{O}$ bonds. This relaxation energy is 1.52 eV for single vacancy in this study. For two vacancies, this energy is much relaxed if we remove the two neighboring O atoms in the same plane perpendicular to these chains.

5.4 Oxygen Vacancy Cluster

Sec. 5.3 shows that the oxygen vacancy pair has a stable structure in the plane perpendicular to the broken chains. When more vacancies join the pair to form clusters, there are two possible structures: 1-D (Fig. 5.7) or 2-D (Fig. 5.8) clusters. Direct electron bombardment experiment by Bursill and Lin [8] clearly showed that oxygen vacancies can form a 1-D dendritic structure. This 1-D dendritic structure plays an important role in the development of electric fatigue. It is also related to current leakage, causing material failure. In this 1-D cluster, most vacancies have

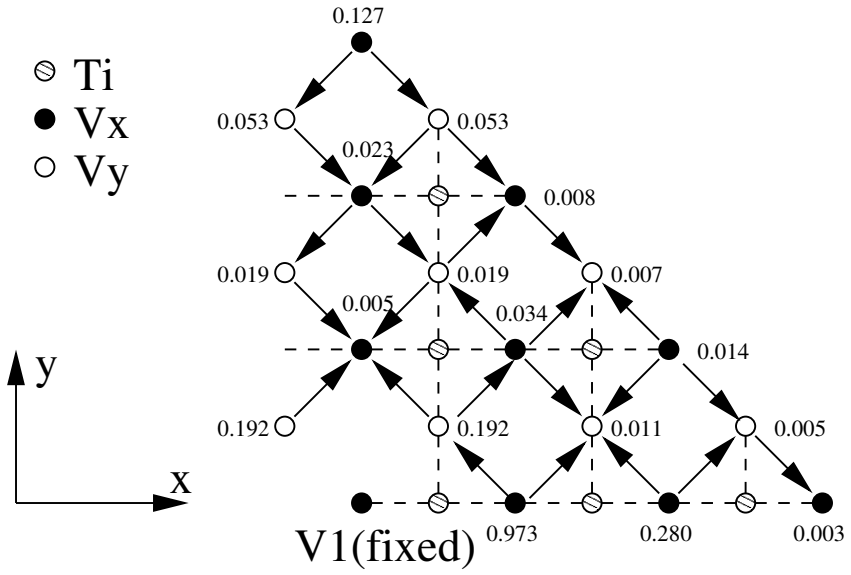

Figure 5.6: Energies of two vacancies in the x-y plane. V_1 is fixed and V_2 is allowed at different positions. Ti atoms are not shown and energy is in eV.

Table 5.1: Divacancy interaction energy (eV) in $BaTiO_3$ tetragonal phase.

$V_x - V_x$		$V_x - V_y$		$V_x - V_z$	
$(dX,\ dY,\ dZ)$	E	$(dX,\ dY,\ dZ)$	E	$(dX,\ dY,\ dZ)$	E
(0, 1, 0)	0.005	(0.5, 0.5, 0)	0.192	(0.5, 0, 0.5)	0.191
(0, 2, 0)	0.023	(0.5, 1.5, 0)	0.019	(0.5, 0, 1.5)	0.022
(0, 3, 0)	0.127	(0.5, 2.5, 0)	0.005	(0.5, 0, 2.5)	0.012
(1, 0, 0)	0.973	(1.5, 0.5, 0)	0.011	(1.5, 0, 0.5)	0.021
(1, 1, 0)	0.034	(1.5, 1.5, 0)	0.007	(1.5, 0, 1.5)	0.017
(1, 2, 0)	0.007	(1.5, 2.5, 0)	-0.003	(1.5, 0, 2.5)	0.008
(2, 0, 0)	0.280	(2.5, 0.5, 0)	0.005	(2.5, 0, 0.5)	0.012
(2, 1, 0)	0.014	(2.5, 1.5, 0)	-0.003	(2.5, 0, 1.5)	0.010
(2, 2, 0)	0.007	(2.5, 2.5, 0)	-0.002	(2.5, 0, 2.5)	0.009
(3, 0, 0)	0.003				

Table 5.2: Divacancy relaxation energy (eV) in $BaTiO_3$ tetragonal phase.

$V_x - V_x$		$V_x - V_y$		$V_x - V_z$	
$(dX,\ dY,\ dZ)$	ΔE_{rlx}	$(dX,\ dY,\ dZ)$	ΔE_{rlx}	$(dX,\ dY,\ dZ)$	ΔE_{rlx}
(0, 1, 0)	3.230	(0.5, 0.5, 0)	3.735	(0.5, 0, 0.5)	3.672
(0, 2, 0)	3.030	(0.5, 1.5, 0)	3.108	(0.5, 0, 1.5)	3.123
(0, 3, 0)	2.914	(0.5, 2.5, 0)	3.038	(0.5, 0, 2.5)	3.046
(1, 0, 0)	2.798	(1.5, 0.5, 0)	3.120	(1.5, 0, 0.5)	3.139
(1, 1, 0)	3.098	(1.5, 1.5, 0)	3.046	(1.5, 0, 1.5)	3.053
(1, 2, 0)	3.050	(1.5, 2.5, 0)	3.037	(1.5, 0, 2.5)	3.050
(2, 0, 0)	2.844	(2.5, 0.5, 0)	3.060	(2.5, 0, 0.5)	3.044
(2, 1, 0)	3.053	(2.5, 1.5, 0)	3.161	(2.5, 0, 1.5)	3.165
(2, 2, 0)	3.026	(2.5, 2.5, 0)	3.053	(2.5, 0, 2.5)	3.036
(3, 0, 0)	3.030				

two neighbors. The ending vacancies have one neighbor and the sites which has three neighbors create new branches. Such 1-D cluster has a large perimeter, thus corresponds to large relaxation region. In the 2-D cluster, the internal vacancies have four neighbors and more repulsion from each other. It has smaller perimeter and gives relatively small relaxation region. So the 1-D cluster should be more stable than the 2-D cluster. Such a preference is confirmed by the following interaction energy calculations.

We constructed linear, branchy and planar V_x clusters in (100) plane in $10\times10\times10$ super cells (Fig. 5.9). Each cluster has 9 oxygen vacancies in different configurations and are fully minimized. It is found that the linear clusters (Fig. 5.9a and 5.9b) have the lowest energies. The chain slightly prefers the direction along (001) over (010) by 0.025 eV. The planar clusters (Fig. 5.9g) has the highest energies. Linear structures with branches (Fig. 5.9c, 5.9d, 5.9e and 5.9f) have energies higher than the linear clusters but much lower than the planar clusters. So during oxygen vacancy growth, the linear clusters with/without branches will dominate and cause a final dendritic structure.

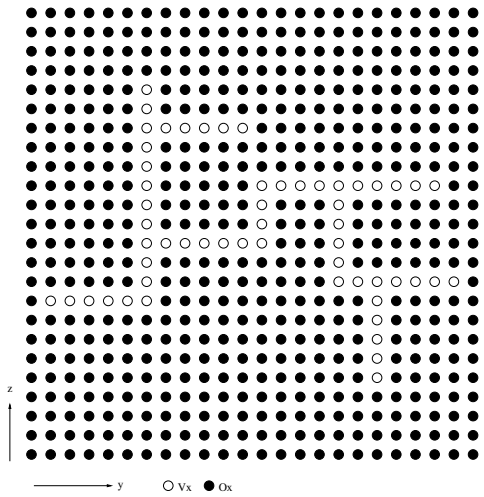

Figure 5.7: Schematic of a 1-D clusters.

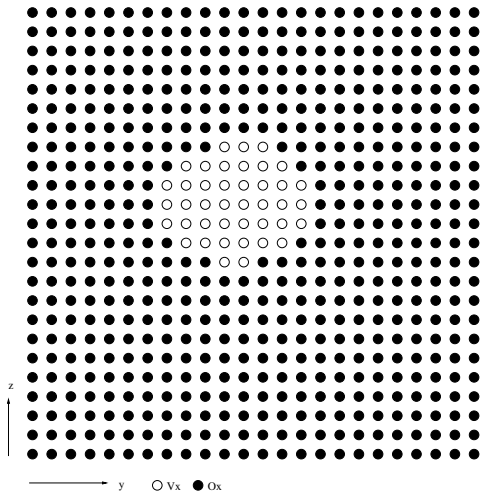

Figure 5.8: Schematic of a 2-D clusters.

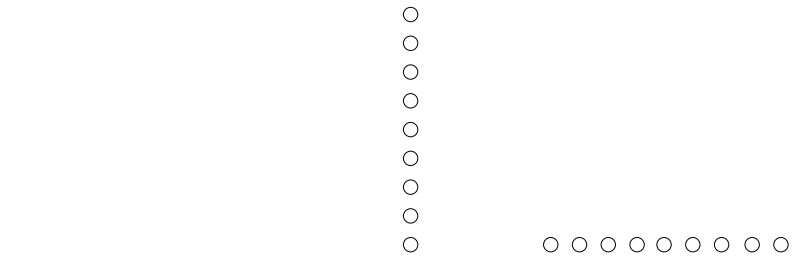

(a) 0.335 eV (b) 0.360 eV

(c) 0.456 eV (d) 0.636 eV (e) 0.669 eV (f) 0.650 eV

(g) 1.878 eV

Figure 5.9: Schematic of oxygen vacancy clusters.

5.5 Discussion

In Section 5.2 we show that the mobility of oxygen vacancy is very low. However during cycling and near the electrode, where polarization change cause a large local field, the oxygen vacancies are activated. The 1-D chains may develop branches to form a dendritic structure during its growth. Such oxygen-deficient dendritic structures (trees) were observed in $LiTaO_3$ experiment [8]. When the dendritic trees are developed, the domains around the trees are pinned and a polarization reduction will be observed.

These dendritic structure has three effects on the properties of $BaTiO_3$.

- The local relaxation cause Ti atoms move backward, the local polarization of the chain is tail-tail. This chain is unswitchable and it cause the polarization fatigue.

- In oxide crystal, an oxygen vacancy leaves two electrons in which is usually called F-center. The dendritic structure is conductive due to these excess electrons. When two dendritic trees from the two electrode meet in the middle of a thin film, a large leakage current appear.

- Stress concentration forms around such dendritic trees, which cause the mechanic failure.

By using oxide electrodes on the films, we can reduce the concentration of oxygen vacancies and prevent the formation of the dendritic structures.

5.6 Conclusion

The oxygen vacancy energies and transition barriers in $BaTiO_3$ are calculated. Diffusivity and mobility of oxygen vacancies increase 10^4 from room temperature to the

Curie temperature. Oxygen vacancy interaction energies are calculated. We found that these oxygen vacancies preferred 1-D cluster due to large relaxation energy. During growth, possible branches give the dendritic structures. These dendritic structures can cause polarization fatigue, leakage current and mechanic failure.

Chapter 6

Future Work

6.1 Density Functional Theory

The P-QEq is optimized with DFT calculations on the phase energy and Mulliken Charges. So the quality of such calculation plays an key role to affects the P-QEq result.

In the density functional theory [35, 44], the many electron effect is replaced by a potential. The major result of density functional theory is that there exists a form of this potential, depending only on the electron density $n(\mathbf{r})$, which yields the exact ground state energy and density. Unfortunately, such an exact form is not known and there exist several approximations to it. Often, this functional is taken to depend on the local value of the density only, which leads to the local density approximation (LDA). Other methods take the density gradient into functional with various form, which are usually called general gradient approximation (GGA).

LDA and GGA usually gives a smaller and larger lattice parameter than the experiments respectively. In ferroelectrics, such error can not be ignored. For the case of $BaTiO_3$, LDA gives a lattice parameter of 3.95 Å for cubic phase [14] while the experiment at 300 K give a value of 4.012. This correspond to a pressure of 5 GPa in experiment. GGA with PW91 functional [60] gives 4.007 Å for the cubic phase [72], but the c/a ratio is 1.0375, much larger than the observed value of 1.01.

In this study, we optimized the P-QEq to the GGA/PW91 calculation. The c/a ratio was taken from experimental value of 1.01.

The recent development in hybrid methods [3] of DFT and Hatree-Fock achieved a lot of successes in non periodic calculations. It would be interesting to test such a method in the periodic system for ferroelectrics.

6.2 Anharmonic Effects

In this thesis, we calculate the ZPE and entropies of $BaTiO_3$ within the harmonic approximation. This method is appliable as long as anharmonic effects can be ignored. At high temperature, these effects could be corrected by two possible approaches.

One approach is the velocity autocorrelation method. In this method, a long time molecular dynamics of a large system is performed. If the MD trajectory is close to a canonical ensemble, then the phonon density of states can be reconstructed from the velocity autocorrelation (VAC) function and thermodynamic functions can be obtained within quasiharmonic approximation. However, there are some theoretical and technique challenges to apply this method to ferroelectrics.

- The VAC is a semi-classical approach, in that the density of states is calculated in the simulation classically, but the thermodynamic functions are then calculated with quantum mechanics. It is expected that when anharmonic effects are not very large, the quantum corrections to DOS will be negligibly small.

- The VAC is a quasi-harmonic approach; DOS are calculated at each temperature and fit to an model where each mode is harmonic.

- The entropy change during phase transition of $BaTiO_3$ are about 0.5 % and this is usually beyond accuracy of the VAC method. In our test of this method, we found that much errors come from rescaling DOS from VAC function. The

rescaling procedure usually overestimate low frequency DOS and the big fluctuation of this overestimation is random. For the case of $BaTiO_3$, the fluctuation itself results in an error of 3 to 5 % of the total entropy.

- The phase structures of ferroelectrics are close to each other and sensitive to stress and temperature. So keeping a phase structure in MD for enough time is challenging. During MD, an unstable phase develops low frequency diffusion modes, which mix with vibrational modes and overestimate entropy. Recently, a two-phase method has been developed by Lin *et al.* [47] to separates these two types of modes. An application of this method may solve this problem.

Another candidate is the so-called self-consistent phonon approximation (SPA) [75], where a trial Hamiltonian of harmonic form is introduced to construct the density matrix. The trial Hamiltonian is determined variationally to obtained the free energy based on this density matrix and the Hamiltonian of the crystal. This method include all even derivatives of the interatomic potential. An generalization including odd derivatives is the improved self-consistent phonon approximation (ISPA) [32]. Application of ISPA to Argon gas gives good expansivity, heat capacity and bulk modulus.

SPA and ISPA provide a systematical approach to include anharmonic effects. However, the computation is much more expensive than the harmonic lattice dynamics since an thermodynamic average of the second derivatives are required. It is even worse for many-body potentials, where the analytic form of third derivatives are complicated.

With the development of more powerful computer and parallelization algorithm, this approach seems to be feasible in the future.

Bibliography

[1] H. N. AlShareef, B. A. Tuttle, W. L. Warren, T. J. Headley, D. Dimos, J. A. Voigt, and R. D. Nasby. Effect of B-site Cation Stoichiometry on Electrical Fatigue of $RuO_2/Pb(Zr_xTi_{1-x})O_3/RuO_2$ Capacitors. *J. Appl. Phys.*, 79(2):1013, 1996.

[2] O. Auciello, J. F. Scott, and R. Ramesh. The Physics of Ferroelectric Memories. *Phys. Today*, 51(7):22, 1998.

[3] A. D. Becke. Density-Functional Thermochemistry. 3. The Role of Exact Exchange. *J. Chem. Phys.*, 98(7):5648, 1993.

[4] I. B. Bersuker. On Origin of Ferroelectricity in Perovskite-Type Crystals. *Physics Letters*, 20(6):589, 1966.

[5] I. B. Bersuker and B. G. Vekhter. Interband Interaction and Sponteneous Polarization of a Crystal Lattice. *Soviet Physics Solid State,Ussr*, 9(9):2084, 1968.

[6] M. Born and K. Huang. *Dynamical Theory of Crystal Lattices*. Oxford University Press, 1954.

[7] S. F. Boys. Electronic Wave Functions .1. A General Method of Calculation for the Stationary States of Any Molecular System. *Proceedings of the Royal Society of London Series a- Mathematical and Physical Sciences*, 200(1063):542, 1950.

[8] L. A. Bursill and P. J. Lin. Electron-Microscopic Studies of Ferroelectric-Crystals. *Ferroelectrics*, 70(3-4):191, 1986.

[9] J. Chen, M. P. Harmer, and D. M. Smyth. Polarization Fatigue in Perovskite Ferroelectric Ceramics and Thin-Films. In *Proceedings of the IEEE 8th International Symposium on Applications of Ferroelectrics*, page 111, Piscataway, NJ, 1992.

[10] W. Cochran. Crystal Stability and the Theory of Ferroelectricity. *Phys. Rev. Lett.*, 3(9):412, 1959.

[11] W. Cochran. Crystal Stability and the Theory of Ferroelectricity. *Adv. Phys.*, 9(36):387, 1960.

[12] W. Cochran and R. A. Cowley. Dielectric Constants and Lattice Vibrations. *J. Phys. Chem. Solids*, 23(MAY):447, 1962.

[13] R. E. Cohen. Origin of Ferroelectricity in Perovskite Oxides. *Nature*, 358(6382):136, 1992.

[14] R. E. Cohen and H. Krakauer. Lattice-Dynamics and Origin of Ferroelectricity in $BaTiO_3$ - Linearized-Augmented-Plane-Wave Total-Energy Calculations. *Phys. Rev. B*, 42(10):6416, 1990.

[15] R. Comes, M. Lambert, and A. Guinier. Chain Structure of $BaTiO_3$ and $KNbO_3$. *Solid State Commun.*, 6(10):715, 1968.

[16] R. Comes, M. Lambert, and A. Guinier. Linear Disorder in Crystals (Silicon, Quartz and Ferroelectric Perovskites). *Acta Crystallographica Section a-Crystal Physics Diffraction Theoretical and General Crystallography*, A 26:244, 1970.

[17] M. Dawber and J. F. Scott. A Model for Fatigue in Ferroelectric Perovskite Thin Films. *Appl. Phys. Lett.*, 76(8):1060, 2000.

[18] M. Dawber and J. F. Scott. A Model for Fatigue in Ferroelectric Perovskite Thin Films. *Appl. Phys. Lett.*, 76(24):3655, 2000.

[19] T. P. Dougherty, G. P. Weiderrecht, K. A. Nelson, M. H. Garrett, H. P. Jenssen, and C. Warde. Femtosecond Time-Resolved Spectroscopy of Soft Modes in Structural Phase-Transitions of Perovskites. *Phys. Rev. B*, 50(13):8996, 1994.

[20] T. P. Dougherty, G. P. Wiederrecht, K. A. Nelson, M. H. Garrett, H. P. Jensen, and C. Warde. Femtosecond Resolution of Soft Mode-Dynamics in Structural Phase-Transitions. *Science*, 258(5083):770, 1992.

[21] M. T. Dove. *Introduction to Lattice Dynamics.* Cambridge University Press, 1993.

[22] H. M. Duiker, P. D. Beale, J. F. Scott, C. A. P. Dearaujo, B. M. Melnick, J. D. Cuchiaro, and L. D. McMillan. Fatigue and Switching in Ferroelectric Memories - Theory and Experiment. *J. Appl. Phys.*, 68(11):5783, 1990.

[23] P. Ewald. *Ann. Phys.*, 64:253, 1921.

[24] P. W. Forsbergh. Domain Structures and Phase Transitions in Barium Titanate. *Physical Review*, 76(8):1187, 1949.

[25] H. X. Fu and R. E. Cohen. Polarization Rotation Mechanism for Ultrahigh Electromechanical Response in Single-Crystal Piezoelectrics. *Nature*, 403(6767):281, 2000.

[26] F. Gervais. Displacive - Order-Disorder Crossover in Ferroelectrics. *Ferroelectrics*, 53(1-4):91, 1984.

[27] P. Ghosez, X. Gonze, and J. P. Michenaud. Ab Initio Phonon Dispersion Curves and Interatomic Force Constants of Barium Titanate. *Ferroelectrics*, 206(1-4):205, 1998.

[28] P. Ghosez, J. P. Michenaud, and X. Gonze. Dynamical Atomic Charges: The Case of ABO_3 Compounds. *Phys. Rev. B*, 58(10):6224, 1998.

[29] P. Ghosez and K. M. Rabe. Microscopic model of ferroelectricity in stress-free $PbTiO_3$ ultrathin films. *Appl. Phys. Lett.*, 76(19):2767, 2000.

[30] P. Giannozzi, S. Degironcoli, P. Pavone, and S. Baroni. Abinitio Calculation of Phonon Dispersions in Semiconductors. *Phys. Rev. B*, 43(9):7231, 1991.

[31] W. A. Goddard, Q. Zhang, M. Uludogan, A. Strachan, and T. Cagin. The ReaxFF Polarizable Reactive Force Fields for Molecular Dynamics Simulation of Ferroelectrics. In *American Institute of Physics Conference*, volume 626, page 45, 2002.

[32] V. V. Goldman, G. K. Horton, and M. L. Klein. An Improved Self-Consistent Phonon Approximation. *Phys. Rev. Lett.*, 21(22):1527, 1968.

[33] J. Harada, J. D. Axe, and G. Shirane. Neutron-Scattering Studyof Soft Modes in Cubic $BaTiO_3$. *Phys. Rev. B*, 4(1):155, 1971.

[34] J. Harada and G. Honjo. X-Ray Studies of Lattice Vibration in Tetragonal Barium Titanate. *J. Phys. Soc. Jpn.*, 22(1):45, 1967.

[35] P. Hohenberg and W. Kohn. Inhomogeneous Electron Gas. *Physical Review*, 136(3B):864, 1964.

[36] G. Honjo, S. Kodera, and N. Kitamura. Diffuse Streak Diffraction Patterns from Single Crystals .I. General Discussion + Aspects of Electron Diffraction Diffuse Streak Patterns. *J. Phys. Soc. Jpn.*, 19(3):351, 1964.

[37] A. Huller. Displacement Correlation and Anomalous X-Ray Scattering in $BaTiO_3$. *Solid State Commun.*, 7(8):589, 1969.

[38] J. Iniguez and D. Vanderbilt. First-Principles Study of the Temperature-Pressure Phase Diagram of $BaTiO_3$. *Phys. Rev. Lett.*, 89(11):art. no., 2002.

[39] H. A. Jahn and E. Teller. Stability of Polyatomic Molecules in Degenerate Electronic States. I - Orbital Degeneracy. *Proceedings of the Royal Society of London Series A- Mathematical and Physical Sciences*, 161:220, 1937.

[40] H. F. Kay and P. Vousden. Symmetry Changes in Barium Titanate at Low Temperatures and Their Relation to Its Ferroelectric Properties. *Philosophical Magazine*, 40(309):1019, 1949.

[41] D. Khatib, R. Migoni, G. E. Kugel, and L. Godefroy. Lattice-Dynamics of $BaTiO_3$ in the Cubic Phase. *J. Phys.-Condes. Matter*, 1(49):9811, 1989.

[42] W. Kinase. On Interactions among Ions of a Batio3 Crystal and on Its 180-Degrees and 90-Degrees Type Domain Boundaries. *Prog. Theor. Phys.*, 13(5):529, 1955.

[43] W. Kinase and H. Takahasi. On the 180-Degrees-Type Domain Wall of $BaTiO_3$ Crystal. *J. Phys. Soc. Jpn.*, 12(5):464, 1957.

[44] W. Kohn and L. J. Sham. Self-Consistent Equations Including Exchange and Correlation Effects. *Physical Review*, 140(4A):1133, 1965.

[45] G. H. Kwei, A. C. Lawson, S. J. L. Billinge, and S. W. Cheong. Structures of the Ferroelectric Phases of Barium-Titanate. *J. Phys. Chem.*, 97(10):2368, 1993.

[46] G. V. Lewis and C. R. A. Catlow. Defect Studies of Doped and Undoped Barium-Titanate Using Computer-Simulation Techniques. *J. Phys. Chem. Solids*, 47(1):89, 1986.

[47] S. T. Lin, M. Blanco, and W. A. Goddard. The Two-Phase Model for Calculating Thermodynamic Properties of Liquids from Molecular Dynamics: Validation for the Phase Diagram of Lennard-Jones Fluids. *J. Chem. Phys.*, 119(22):11792, 2003.

[48] M. E. Lines and A. M. Glass. *Principles and applications of ferroelectrics and related materials*. Oxford University Press, 2001.

[49] E. A. Little. Dynamic Behavior of Domain Walls in Barium Titanate. *Physical Review*, 98(4):978, 1955.

[50] S. W. Lovesey and T. Springer. Dynamics of Solids and Liquids by Neutron Scattering. 3, 1977.

[51] Y. Luspin, J. L. Servoin, and F. Gervais. Soft Mode Spectroscopy in Barium-Titanate. *Journal of Physics C-Solid State Physics*, 13(19):3761, 1980.

[52] W. J. Merz. The Electric and Optical Behavior of $BaTiO_3$ Single-Domain Crystals. *Physical Review*, 76(8):1221, 1949.

[53] W. J. Merz. Domain Properties in $BaTiO_3$. *Physical Review*, 88(2):421, 1952.

[54] W. J. Merz. Double Hysteresis Loop of $BaTiO_3$ at the Curie Point. *Physical Review*, 91(3):513, 1953.

[55] W. J. Merz. Domain Formation and Domain Wall Motions in Ferroelectric $BaTiO_3$ Single Crystals. *Physical Review*, 95(3):690, 1954.

[56] B. Meyer and D. Vanderbilt. Ab initio study of ferroelectric domain walls in $PbTiO_3$. *Phys. Rev. B*, 65(10):art. no., 2002.

[57] T. Mihara, H. Watanabe, and C. A. P. Dearaujo. Polarization Fatigue Characteristics of Sol-Gel Ferroelectric $Pb(Zr_{0.4}Ti_{0.6})O_3$ Thin-Film Capacitors. *Jpn. J. Appl. Phys. Part 1—Regul. Pap. Short Notes Rev. Pap.*, 33(7A):3996, 1994.

[58] J. Padilla, W. Zhong, and D. Vanderbilt. First-Principles Investigation of 180 Degrees Domain Walls in $BaTiO_3$. *Phys. Rev. B*, 53(10):R5969, 1996.

[59] J. P. Perdew, K. Burke, and M. Ernzerhof. Generalized gradient approximation made simple. *Phys. Rev. Lett.*, 77(18):3865, 1996.

[60] J. P. Perdew and W. Yue. Accurate and Simple Density Functional for the Electronic Exchange Energy—Generalized Gradient Approximation. *Phys. Rev. B*, 33(12):8800, 1986.

[61] A. M. Quittet and M. Lambert. Temperature-Dependence of Raman Cross-Section and Light- Absorption in Cubic $BaTiO_3$. *Solid State Commun.*, 12(10):1053, 1973.

[62] A. K. Rappe and W. A. Goddard. Charge Equilibration for Molecular-Dynamics Simulations. *J. Phys. Chem.*, 95(8):3358, 1991.

[63] B. Ravel, E. A. Stern, R. I. Vedrinskii, and V. Kraizman. Local structure and the phase transitions of $BaTiO_3$. *Ferroelectrics*, 206(1-4):407, 1998.

[64] X. B. Ren. Large electric-field-induced strain in ferroelectric crystals by point-defect-mediated reversible domain switching. *Nat. Mater.*, 3(2):91, 2004.

[65] J. F. Scott, C. A. Araujo, B. M. Melnick, L. D. McMillan, and R. Zuleeg. Quantitative Measurement of Space-Charge Effects in Lead Zirconate-Titanate Memories. *J. Appl. Phys.*, 70(1):382, 1991.

[66] M. Sepliarsky, S. R. Phillpot, D. Wolf, M. G. Stachiotti, and R. L. Migoni. Atomic-Level Simulation of Ferroelectricity in Perovskite Solid Solutions. *Appl. Phys. Lett.*, 76(26):3986, 2000.

[67] A. Sheikholeslami and P. G. Gulak. A Survey of Circuit Innovations in Ferroelectric Random-Access Memories. *Proc. IEEE*, 88(5):667, 2000.

[68] G. Shirane and A. Takeda. Transition Energy and Volume Change at 3 Transitions in Barium Titanate. *J. Phys. Soc. Jpn.*, 7(1):1, 1952.

[69] A. K. Tagantsev, I. Stolichnov, E. L. Colla, and N. Setter. Polarization fatigue in ferroelectric films: Basic experimental findings, phenomenological scenarios, and microscopic features. *J. Appl. Phys.*, 90(3):1387, 2001.

[70] A. K. Tagantsev and I. A. Stolichnov. Injection-Controlled Size Effect on Switching of Ferroelectric Thin Films. *Appl. Phys. Lett.*, 74(9):1326, 1999.

[71] S. Tinte, M. G. Stachiotti, M. Sepliarsky, R. L. Migoni, and C. O. Rodriguez. Atomistic Modelling of $BaTiO_3$ Based on First-Principles Calculations. *J. Phys.-Condes. Matter*, 11(48):9679, 1999.

[72] M. Uludogan, T. Cagin, and W. A. Goddard. Ab Initio Studies on Phase Behavior of Barium Titanate. In *Materials Research Society Proceedings*, volume 718, page D10.11, 2002.

[73] K. A. Vangenechten, W. J. Mortier, and P. Geerlings. Intrinsic Framework Electronegativity—a Novel Concept in Solid-State Chemistry. *J. Chem. Phys.*, 86(9):5063, 1987.

[74] R. Waser. Bulk Conductivity and Defect Chemistry of Acceptor-Doped Strontium-Titanate in the Quenched State. *J. Am. Ceram. Soc.*, 74(8):1934, 1991.

[75] Werthame.Nr. Self-Consistent Phonon Formulation of Anharmonic Lattice Dynamics. *Phys. Rev. B*, 1(2):572, 1970.

[76] K. H. Weyrich and R. Siems. Deformation Charge-Distribution and Total Energy for Perovskites. *Zeitschrift Fur Physik B—Condensed Matter*, 61(1):63, 1985.

[77] H. H. Wieder. Electrical Behavior of Barium Titanate Single Crystals at Low Temperatures. *Physical Review*, 99(4):1161, 1955.

[78] Y. Yamada, G. Shirane, and A. Linz. Study of Critical Fluctuations in $BaTiO_3$ by Neutron Scattering. *Physical Review*, 177(2):848, 1969.

[79] R. Yu and H. Krakauer. First-Principles Determination of Chain-Structure Instability in $KNbO_3$. *Phys. Rev. Lett.*, 74(20):4067, 1995.

[80] W. Zhong, R. D. Kingsmith, and D. Vanderbilt. Giant LO-TO Splitting Sin Perovskite Ferroelectrics. *Phys. Rev. Lett.*, 72(22):3618, 1994.

[81] W. Zhong and D. Vanderbilt. Competing Structural Instabilities in Cubic Perovskites. *Phys. Rev. Lett.*, 74(13):2587, 1995.

[82] W. Zhong, D. Vanderbilt, and K. M. Rabe. Phase-Transitions in $BaTiO_3$ from First Principles. *Phys. Rev. Lett.*, 73(13):1861, 1994.

[83] W. Zhong, D. Vanderbilt, and K. M. Rabe. First-Principles Theory of Ferroelectric Phase-Transitions for Perovskites—the Case of $BaTiO_3$. *Phys. Rev. B*, 52(9):6301, 1995.

Appendix A

Charge Equilibration

A.1 Derivatives of Basic Coupling Function $j_{ik,jl}$

First we summarize the derivatives of the basic coupling function $j_{ik,jl}$, which is a component of the coupling function $J_{ik,jl}$. For simplification, we define

$$c_{ik,jl} \equiv \sqrt{\frac{\alpha_{ik}\alpha_{jl}}{\alpha_{ik}+\alpha_{jl}}}, \tag{A.1}$$

$$t_{ik,jl} \equiv c_{ik,jl} r_{ik,jl}. \tag{A.2}$$

So, the first and second derivatives of $j_{ik,jl}$ *w.r.t.* the distance $r_{ik,jl}$ can be written as

$$\frac{\partial j_{ik,jl}}{\partial r_{ik,jl}} = \begin{cases} -\frac{4}{3\sqrt{\pi}} c_{ik,jl}^3 r_{ik,jl}, & r_{ik,jl} \to 0; \\ \frac{1}{r_{ik,jl}^2}\left(\frac{2t_{ik,jl}\exp(-t_{ik,jl}^2)}{\sqrt{\pi}} - erf(t_{ik,jl})\right), & \text{else}, \end{cases} \tag{A.3}$$

and

$$\frac{\partial^2 j_{ik,jl}}{\partial r_{ik,jl}^2} = \begin{cases} -\frac{4}{3\sqrt{\pi}} c_{ik,jl}^3, & r_{ik,jl} \to 0; \\ \frac{1}{r_{ik,jl}^3}\left(-\frac{4}{\sqrt{\pi}} t_{ik,jl}\exp(-t_{ik,jl}^2)(1+t_{ik,jl}^2) + 2erf(t_{ik,jl})\right), & \text{else}, \end{cases} \tag{A.4}$$

So the first and second derivatives of $j_{ik,jl}$ *w.r.t.* the Cartesian coordinates and strains are

$$\frac{\partial j_{ik,jl}}{\partial r_{ikx}} = \begin{cases} -\frac{4}{3\sqrt{\pi}} c_{ik,jl}^3 r_{ikx,jlx}, & r_{ik,jl} \to 0; \\ \frac{r_{ikx,jlx}}{r_{ik,jl}} \frac{\partial j_{ik,jl}}{\partial r_{ik,jl}}, & \text{else}, \end{cases} \tag{A.5}$$

$$\frac{\partial^2 j_{ik,jl}}{\partial r_{ikx} \partial r_{iky}} = \begin{cases} -\frac{4}{3\sqrt{\pi}} c_{ik,jl}^3, & r_{ik,jl} \to 0 \text{ and } x = y; \\ \frac{8}{5\sqrt{\pi}} c_{ik,jl}^5 r_{ikx,jlx} r_{iky,jly}, & r_{ik,jl} \to 0 \text{ and } x \neq y; \\ \frac{r_{ikx,jlx}}{r_{ik,jl}} \frac{r_{iky,jly}}{r_{ik,jl}} \frac{\partial^2 j_{ik,jl}}{\partial r_{ik,jl}^2} & \\ + \frac{1}{r_{ik,jl}^3} \left(\delta_{xy} r_{ik,jl}^2 - r_{ikx,jlx} r_{iky,jly} \right) \frac{\partial j_{ik,jl}}{\partial r_{ik,jl}}, & \text{else}, \end{cases} \tag{A.6}$$

$$\frac{\partial j_{ik,jl}}{\partial \epsilon_{xy}} = \frac{\partial j_{ik,jl}}{\partial r_{ik,jl}} \frac{\partial r_{ik,jl}}{\partial \epsilon_{xy}} \tag{A.7}$$

and

$$\frac{\partial^2 j_{ik,jl}}{\partial \epsilon_{xy} \partial \epsilon_{zw}} = \frac{\partial^2 j_{ik,jl}}{\partial r_{ik,jl}^2} \frac{\partial r_{ik,jl}}{\partial \epsilon_{xy}} \frac{\partial r_{ik,jl}}{\partial \epsilon_{zw}} + \frac{\partial j_{ik,jl}}{\partial r_{ik,jl}} \frac{\partial^2 r_{ik,jl}}{\partial \epsilon_{xy} \partial \epsilon_{zw}}. \tag{A.8}$$

A.2 Derivatives of Coupling Constants $J_{ik,jl}$

The derivatives of $J_{ik,jl}$ plays an important role in application of the model.

A.2.1 Non-periodic System

From Eq. (2.14), we get

$$\frac{\partial J_{ik,jl}}{\partial r_{ikx}} = \begin{cases} 0, & ik = jl; \\ \frac{\partial j_{ik,jl}}{\partial r_{ikx}}, & ik \neq jl. \end{cases} \tag{A.9}$$

$$\frac{\partial^2 J_{ik,jl}}{\partial r_{ikx} \partial r_{iky}} = \begin{cases} 0, & ik = jl; \\ \frac{\partial^2 j_{ik,jl}}{\partial r_{ikx} \partial r_{iky}}, & ik \neq jl. \end{cases} \tag{A.10}$$

A.2.2 3D-periodic System

From Eq. (2.15), the first and second derivatives of $J_{ik,jl}$ *w.r.t.* the Cartesian coordinates and strains are

$$\begin{aligned}\frac{\partial J_{ik,jl}}{\partial r_{ikx}} &= \frac{4\pi}{V}\sum_{\mathbf{G}\neq 0} iG_x G^{-2}\exp(-\frac{G^2}{4\alpha_{ew}}-\frac{G^2}{4\alpha_{jl}})\exp(i\mathbf{G}\cdot\mathbf{r}_{ik,jl}) \\ &\quad +\sum_{\mathbf{L}}\left(\frac{\partial j_{ik,jl}(\mathbf{r}_{ik,jl}+\mathbf{L})}{\partial r_{ikx}}-\frac{\partial j_{ik,ew}(\mathbf{r}_{ik,jl}+\mathbf{L})}{\partial r_{ikx}}\right), \qquad \text{(A.11)}\end{aligned}$$

$$\begin{aligned}\frac{\partial^2 J_{ik,jl}}{\partial r_{ikx}\partial r_{iky}} &= -\frac{4\pi}{V}\sum_{\mathbf{G}\neq 0} G_x G_y G^{-2}\exp(-\frac{G^2}{4\alpha_{ew}}-\frac{G^2}{4\alpha_{jl}})\exp(i\mathbf{G}\cdot\mathbf{r}_{ik,jl}) \\ &\quad +\sum_{\mathbf{L}}\left(\frac{\partial^2 j_{ik,jl}(\mathbf{r}_{ik,jl}+\mathbf{L})}{\partial r_{ikx}\partial r_{iky}}-\frac{\partial^2 j_{ik,ew}(\mathbf{r}_{ik,jl}+\mathbf{L})}{\partial r_{ikx}\partial r_{iky}}\right), \qquad \text{(A.12)}\end{aligned}$$

$$\begin{aligned}\frac{\partial J_{ik,jl}}{\partial \epsilon_{xy}} &= -\frac{4\pi}{V}\sum_{\mathbf{G}\neq 0} \beta_1 G^{-2}\exp(-\frac{G^2}{4\alpha_{ew}}-\frac{G^2}{4\alpha_{jl}})\exp(i\mathbf{G}\cdot\mathbf{r}_{ik,jl}) \\ &\quad +\sum_{\mathbf{L}}\left(\frac{\partial j_{ik,jl}(\mathbf{r}_{ik,jl}+\mathbf{L})}{\partial \epsilon_{xy}}-\frac{\partial j_{ik,ew}(\mathbf{r}_{ik,jl}+\mathbf{L})}{\partial \epsilon_{xy}}\right) \\ &\quad -\delta_{xy}\frac{\pi}{2V}(\frac{1}{\alpha_{ik}}-\frac{1}{\alpha_{jl}}), \qquad \text{(A.13)}\end{aligned}$$

and

$$\begin{aligned}\frac{\partial^2 J_{ik,jl}}{\partial \epsilon_{xy}\partial \epsilon_{zw}} &= \frac{4\pi}{V}\sum_{\mathbf{G}\neq 0} \beta_2 G^{-2}\exp(-\frac{G^2}{4\alpha_{ew}}-\frac{G^2}{4\alpha_{jl}})\exp(i\mathbf{G}\cdot\mathbf{r}_{ik,jl}) \\ &\quad +\sum_{\mathbf{L}}\left(\frac{\partial^2 j_{ik,jl}(\mathbf{r}_{ik,jl}+\mathbf{L})}{\partial \epsilon_{xy}\partial \epsilon_{zw}}-\frac{\partial^2 j_{ik,ew}(\mathbf{r}_{ik,jl}+\mathbf{L})}{\partial \epsilon_{xy}\partial \epsilon_{zw}}\right) \\ &\quad +\delta_{xy}\delta_{zw}\frac{\pi}{2V}(\frac{1}{\alpha_{ik}}-\frac{1}{\alpha_{jl}}), \qquad \text{(A.14)}\end{aligned}$$

where

$$\beta_1 \equiv \left(\delta_{xy} + \left(\frac{1}{4\alpha_{ew}} + \frac{1}{4\alpha_{jl}} + \frac{1}{G^2}\right)\frac{\partial G^2}{\partial \epsilon_{xy}}\right),$$

and

$$\begin{aligned}\beta_2 \equiv & \left(\delta_{xy} + \left(\frac{1}{4\alpha_{ew}} + \frac{1}{4\alpha_{jl}} + \frac{1}{G^2}\right)\frac{\partial G^2}{\partial \epsilon_{xy}}\right) \\ & \times \left(\delta_{z,w} + \left(\frac{1}{4\alpha_{ew}} + \frac{1}{4\alpha_{jl}} + \frac{1}{G^2}\right)\frac{\partial G^2}{\partial \epsilon_{zw}}\right) \\ & - \left(\frac{1}{4\alpha_{ew}} + \frac{1}{4\alpha_{jl}} + \frac{1}{G^2}\right)\frac{\partial^2 G^2}{\partial \epsilon_{xy}\partial \epsilon_{zw}} \\ & + \frac{\partial G^2}{\partial \epsilon_{xy}}\frac{\partial G^2}{\partial \epsilon_{zw}} G^{-4}. \end{aligned} \tag{A.15}$$

A.3 First derivatives of Charges

A.3.1 First Derivatives to Coordinates

We take the derivatives of both sides of Eq. (2.18) to $r_{mn,x}$. Then for $i = 1 \ldots N$,

$$\sum_j (J_{is,js} + \delta_{ij} J_i^o)\frac{\partial q_{js}}{\partial r_{mnx}} - \frac{\partial \chi}{\partial r_{mnx}} = -\sum_{jl} \frac{\partial J_{is,jl}}{\partial r_{mnx}} q_{jl}. \tag{A.16}$$

i.e.,

$$\sum_j (J_{is,js} + \delta_{ij} J_i^o)\frac{\partial q_{js}}{\partial r_{mnx}} - \frac{\partial \chi}{\partial r_{mnx}} = -\frac{\partial J_{mn,is}}{\partial r_{mnx}} q_{mn} - \delta_{m,i}\delta_{n,s} \sum_{jl \neq mn} \frac{\partial J_{jl,is}}{\partial r_{jlx}} q_{jl}. \tag{A.17}$$

From the condition of charge conservation Eq. (2.19), we get

$$\sum_i -\frac{\partial q_{is}}{\partial r_{mnx}} = 0. \tag{A.18}$$

With Eqs. (A.17) and (A.18), we get

$$C\begin{pmatrix} \frac{\partial q_{1s}}{\partial r_{mnx}} \\ \frac{\partial q_{2s}}{\partial r_{mnx}} \\ \dots \\ \frac{\partial q_{Ns}}{\partial r_{mnx}} \\ \frac{\partial \chi}{\partial r_{mnx}} \end{pmatrix} = \begin{pmatrix} -\frac{\partial J_{mn,1s}}{\partial r_{mnx}} q_{mn} - \delta_{m,1}\delta_{n,s} \sum_{jl \neq mn} \frac{\partial J_{jl,1s}}{\partial r_{jlx}} q_{jl} \\ -\frac{\partial J_{mn,2s}}{\partial r_{mnx}} q_{mn} - \delta_{m,2}\delta_{n,s} \sum_{jl \neq mn} \frac{\partial J_{jl,2s}}{\partial r_{jlx}} q_{jl} \\ \dots \\ -\frac{\partial J_{mn,Ns}}{\partial r_{mnx}} q_{mn} - \delta_{m,N}\delta_{n,s} \sum_{jl \neq mn} \frac{\partial J_{jl,Ns}}{\partial r_{jlx}} q_{jl} \\ 0 \end{pmatrix}, \tag{A.19}$$

where C is the electrostatic coupling matrix defined in Eq. (2.21).

A.3.2 First Derivatives to Strain

We take the derivatives of both sides of Eq. (2.18) to ϵ_{xy}. Then for $i = 1 \dots N$,

$$\sum_j (J_{is,js} + \delta_{ij} J_i^o) \frac{\partial q_{js}}{\partial \epsilon_{xy}} - \frac{\partial \chi}{\partial \epsilon_{xy}} = -\sum_{jl} \frac{\partial J_{is,jl}}{\partial \epsilon_{xy}} q_{jl}. \tag{A.20}$$

From the condition of charge conservation Eq. (2.19), we get

$$\sum_i -\frac{\partial q_{is}}{\partial \epsilon_{xy}} = 0. \tag{A.21}$$

With Eqs. (A.20) and (A.21), we get

$$C\begin{pmatrix} \frac{\partial q_{1s}}{\partial \epsilon_{xy}} \\ \frac{\partial q_{2s}}{\partial \epsilon_{xy}} \\ \dots \\ \frac{\partial q_{Ns}}{\partial \epsilon_{xy}} \\ \frac{\partial \chi}{\partial \epsilon_{xy}} \end{pmatrix} = \begin{pmatrix} -\sum_{jl} \frac{\partial J_{1s,jl}}{\partial \epsilon_{xy}} q_{jl} \\ -\sum_{jl} \frac{\partial J_{2s,jl}}{\partial \epsilon_{xy}} q_{jl} \\ \dots \\ -\sum_{jl} \frac{\partial J_{Ns,jl}}{\partial \epsilon_{xy}} q_{jl} \\ 0 \end{pmatrix}, \tag{A.22}$$

where C is the electrostatic coupling matrix defined by Eq. (2.21).

A.4 Derivatives of Electrostatic Energy

A.4.1 Force

The force due to electrostatic part of interaction is

$$f_{ikm}^{ES} \equiv -\frac{\partial E^{ES}}{\partial r_{ikm}} = -\sum_{jl} \frac{\partial J_{ik,jl}}{\partial r_{ikm}} q_{ik} q_{jl} - \sum_{j} \frac{\partial E^{ES}}{\partial q_{js}} \frac{\partial q_{js}}{\partial r_{ikm}}. \tag{A.23}$$

Considering the charge equilibrium condition, the last term vanishes:

$$\sum_{j} \frac{\partial E^{ES}}{\partial q_{js}} \frac{\partial q_{js}}{\partial r_{ikm}} = \chi \sum_{j} \frac{\partial q_{js}}{\partial r_{ikm}} = \chi \frac{\partial \sum_j q_{js}}{\partial r_{ikm}} = 0. \tag{A.24}$$

Therefore,

$$f_{ikm}^{ES} = -\sum_{jl} \frac{\partial J_{ik,jl}}{\partial r_{ikm}} q_{ik} q_{jl}. \tag{A.25}$$

In a non-periodic system, substituting Eq. (2.14) into Eq. (A.25), we get the force on the item k (core or shell) of atom i in direction m,

$$f_{ikm}^{ES} = -\sum_{jl \neq ik} \frac{\partial j_{ik,jl}(\mathbf{r}_{ik,jl})}{\partial r_{ikm}} q_{ik} q_{jl}, \tag{A.26}$$

where $\frac{\partial j_{ik,jl}(\mathbf{r}_{ik,jl})}{\partial r_{ikm}}$ has the analytic form in Appendix A.1.

In a periodic system, substituting Eq. (A.11) into Eq. (A.25), we get the force

$$
\begin{aligned}
f_{ikm}^{ES} &= -\frac{1}{2}\frac{4\pi i}{V}\sum_{\mathbf{G}\neq 0} G^{-2} G_m q_{ik} \exp(-\frac{G^2}{4\alpha_{ew}}) \exp(i\mathbf{G}\cdot\mathbf{r}_{ik}) \\
&\quad \times \sum_{jl} q_{jl} \exp(-\frac{G^2}{4\alpha_{jl}}) \exp(-i\mathbf{G}\cdot\mathbf{r}_{ik}) \\
&\quad + \frac{1}{2}\frac{4\pi i}{V}\sum_{\mathbf{G}\neq 0} G^{-2} G_m q_{ik} \exp(-\frac{G^2}{4\alpha_{ik}}) \exp(-i\mathbf{G}\cdot\mathbf{r}_{ik}) \\
&\quad \times \sum_{jl} q_{jl} \exp(-\frac{G^2}{4\alpha_{ew}}) \exp(i\mathbf{G}\cdot\mathbf{r}_{jl}) \\
&\quad -\frac{1}{2} q_{ik} \sum_{jl}\sum_{\mathbf{L}} q_{jl} \\
&\quad \times \left(2\frac{\partial j_{ik,jl}(\mathbf{r}_{ik,jl}+\mathbf{L})}{\partial r_{ikm}} - \frac{\partial j_{ik,ew}(\mathbf{r}_{ik,jl}+\mathbf{L})}{\partial r_{ikm}} - \frac{\partial j_{jl,ew}(\mathbf{r}_{ik,jl}+\mathbf{L})}{\partial r_{ikm}} \right)
\end{aligned} \tag{A.27}
$$

A.4.2 Stress

In periodic system,

$$
\sigma_{xy}^{ES} \equiv \frac{1}{V}\frac{\partial E^{ES}}{\partial \epsilon_{xy}} = \frac{1}{V}\left(\frac{1}{2}\sum_{ik}\sum_{jl} \frac{\partial J_{ik,jl}}{\partial \epsilon_{xy}} q_{ik} q_{jl} + \sum_i \frac{\partial E^{ES}}{\partial q_{is}}\frac{\partial q_{is}}{\partial \epsilon_{xy}} \right). \tag{A.28}
$$

Using the charge equilibrium condition, the last term vanishes,

$$
\sum_i \frac{\partial E^{ES}}{\partial q_{is}}\frac{\partial q_{is}}{\partial \epsilon_{xy}} = \chi \sum_i \frac{\partial q_{is}}{\partial \epsilon_{xy}} = \chi \frac{\partial \sum_i q_{is}}{\partial \epsilon_{xy}} = 0. \tag{A.29}
$$

Therefore we get

$$
\sigma_{xy}^{ES} = \frac{1}{V}\left(\frac{1}{2}\sum_{ik}\sum_{jl} \frac{\partial J_{ik,jl}}{\partial \epsilon_{xy}} q_{ik} q_{jl} \right). \tag{A.30}
$$

Substitute Eq. (2.15) into Eq. (A.28), we get

$$
\begin{aligned}
\sigma_{xy}^{ES} &= -\frac{2\pi}{V^2}\sum_{\mathbf{G}\neq 0} G^{-2}\left(\delta_{ik,jl} + (G^{-2}+\frac{1}{4\alpha})\frac{\partial G^2}{\partial \epsilon_{xy}}\right) \\
&\times \sum_{ik} q_{ik}\exp(-\frac{G^2}{4\alpha_{ew}})\exp(i\mathbf{G}\cdot\mathbf{r}_{ik})\sum_{jl} q_{jl}\exp(-\frac{G^2}{4\alpha_{jl}})\exp(i\mathbf{G}\cdot\mathbf{r}_{ik}) \\
&-\frac{2\pi}{V^2}\sum_{\mathbf{G}\neq 0} G^{-2}\frac{\partial G^2}{\partial \epsilon_{xy}}\sum_{ik} q_{ik}\exp(-\frac{G^2}{4\alpha_{ew}})\exp(i\mathbf{G}\cdot\mathbf{r}_{ik}) \\
&\times \sum_{jl}\frac{q_{jl}}{4\alpha_{jl}}\exp(-\frac{G^2}{4\alpha_{jl}})\exp(i\mathbf{G}\cdot\mathbf{r}_{ik}) \\
&+\frac{q_{ik}}{2V}\sum_{jl}\sum_{\mathbf{L}} q_{jl} \\
&\times \left(2\frac{\partial j_{ik,jl}(\mathbf{r}_{ik,jl}+\mathbf{L})}{\partial \epsilon_{xy}} - \frac{\partial j_{ik,ew}(\mathbf{r}_{ik,jl}+\mathbf{L})}{\partial \epsilon_{xy}} - \frac{\partial j_{jl,ew}(\mathbf{r}_{ik,jl}+\mathbf{L})}{\partial \epsilon_{xy}}\right) \qquad \text{(A.31)}
\end{aligned}
$$

See Appendix A for the derivatives in Eq. (A.31).

A.4.3 Hessian

In order to calculate phonon structure, we need Hessians to construct the dynamic matrix. The Hessians can be obtain by,

$$
\begin{aligned}
H_{ikx,jly}^{ES} &\equiv \frac{\partial^2 E^{ES}}{\partial r_{ikx}\partial r_{jly}} \\
&= \sum_{mn}\frac{\partial^2 J_{ik,mn}}{\partial r_{ikx}\partial r_{jly}} q_{mn} q_{ik} \\
&\quad + \sum_{mn}\frac{\partial J_{ik,mn}}{\partial r_{ikx}}\frac{\partial q_{mn}}{\partial r_{jly}} q_{ik} \\
&\quad + \sum_{mn}\frac{\partial J_{ik,mn}}{\partial r_{ikx}} q_{mn}\frac{\partial q_{ik}}{\partial r_{jly}}. \qquad \text{(A.32)}
\end{aligned}
$$

$$
\frac{\partial^2 J_{ik,mn}}{\partial r_{ikx}\partial r_{jly}} = \delta_{i,m}\delta_{k,n}(\delta_{j,i}\delta_{l,k} - \delta_{j,m}\delta_{l,n})\frac{\partial^2 J_{ik,jl}}{\partial r_{ikx}\partial r_{iky}}. \qquad \text{(A.33)}
$$

The derivatives of J and q to coordinates, $\frac{\partial^2 J_{ik,mn}}{\partial r_{ikx}\partial r_{jly}}$, $\frac{\partial J_{ik,mn}}{\partial r_{ikx}}$ and $\frac{\partial q_{mn}}{\partial r_{jly}}$, are summarized in Appendix A.2 and Appendix A.3.

A.4.4 Strain-Strain Second Derivative

This matrix is required to calculated elastic constants and bulk modulus.

$$\begin{aligned}\frac{\partial E^{ES}}{\partial\epsilon_{xy}\partial\epsilon_{zw}} &= \frac{1}{2}\sum_{ik,jl}\frac{\partial^2 J_{ik,jl}}{\partial\epsilon_{xy}\partial\epsilon_{zw}}q_{ik}q_{jl} \\ &+\frac{1}{2}\sum_{ik,jl}\frac{\partial J_{ik,jl}}{\partial\epsilon_{xy}}\frac{\partial q_{ik}}{\partial\epsilon_{zw}}q_{jl} \\ &+\frac{1}{2}\sum_{ik,jl}\frac{\partial J_{ik,jl}}{\partial\epsilon_{xy}}\frac{\partial q_{jl}}{\partial\epsilon_{zw}}q_{ik}. \end{aligned} \tag{A.34}$$

See also Appendix A.2 and Appendix A.3 for the derivatives of J and q to strains, $\frac{\partial^2 J_{ik,jl}}{\partial\epsilon_{xy}\partial\epsilon_{zw}}$, $\frac{\partial J_{ik,jl}}{\partial\epsilon_{xy}}$, and $\frac{\partial q_{ik}}{\partial\epsilon_{zw}}$.

A.5 First Derivatives of Displacements

Sometime we wish to know the displacements of shell due to some core displacements. Based on the rule of force equilibrium, for $i = 1\ldots N$ and $x = 1\ldots 3$, we have

$$\sum_{jy}\frac{\partial^2 E^P}{\partial r_{isx}\partial r_{jsy}}dr_{jsy} + \frac{\partial^2 E^P}{\partial r_{isx}\partial r_{kcz}}dr_{kcz} = 0. \tag{A.35}$$

In other words,

$$\sum_{jy}\frac{\partial^2 E^P}{\partial r_{isx}\partial r_{jsy}}\frac{\partial r_{jsy}}{\partial r_{kcz}} = -\frac{\partial^2 E^P}{\partial r_{isx}\partial r_{kcz}}. \tag{A.36}$$

In the language of matrix, Eq. (A.36) is written as

$$\begin{pmatrix} \frac{\partial^2 E^P}{\partial r_{1s1}\partial r_{1s1}} & \frac{\partial^2 E^P}{\partial r_{1s1}\partial r_{1s2}} & \cdots & \frac{\partial^2 E^P}{\partial r_{1s1}\partial r_{Ns3}} \\ \frac{\partial^2 E^P}{\partial r_{1s2}\partial r_{1s1}} & \frac{\partial^2 E^P}{\partial r_{1s2}\partial r_{1s2}} & \cdots & \frac{\partial^2 E^P}{\partial r_{1s2}\partial r_{Ns3}} \\ \cdots & \cdots & \cdots & \cdots \\ \frac{\partial^2 E^P}{\partial r_{Ns3}\partial r_{1s1}} & \frac{\partial^2 E^P}{\partial r_{Ns3}\partial r_{1s2}} & \cdots & \frac{\partial^2 E^P}{\partial r_{Ns3}\partial r_{Ns3}} \end{pmatrix} \begin{pmatrix} \frac{\partial r_{1s1}}{\partial r_{kcz}} \\ \frac{\partial r_{1s2}}{\partial r_{kcz}} \\ \cdots \\ \frac{\partial r_{Ns3}}{\partial r_{kcz}} \end{pmatrix} = \begin{pmatrix} \frac{\partial^2 E^P}{\partial r_{1s1}\partial r_{kcz}} \\ \frac{\partial^2 E^P}{\partial r_{1s2}\partial r_{kcz}} \\ \cdots \\ \frac{\partial^2 E^P}{\partial r_{Ns3}\partial r_{kcz}} \end{pmatrix}. \tag{A.37}$$

A.6 Polarizability

The dipole moment of the system is given by

$$\mu_i = q_{ic}\mathbf{r}_{ic} + q_{is}(\{\mathbf{r}_{jl}\}, E)\mathbf{r}_{is}. \tag{A.38}$$

Under electric field in y direction, the change of the dipole moment is

$$d\mu = \sum_i d\mu_i = \sum_{ik} q_{ik} d\mathbf{r}_{ik} + \sum_i \mathbf{r}_{is} \sum_{jl}\sum_z \frac{\partial q_{is}}{\partial r_{jlz}} dr_{jlz} + \sum_i \mathbf{r}_{is} \sum_z \frac{\partial q_{is}}{\partial E_y} dE_y. \tag{A.39}$$

The change in x direction is

$$d\mu_x = \sum_{ik} q_{ik} dr_{ikx} + \sum_i r_{isx} \sum_{jl}\sum_z \frac{\partial q_{is}}{\partial r_{jlz}} dr_{jlz} + \sum_i r_{isx} \sum_z \frac{\partial q_{is}}{\partial E_z} dE_z. \tag{A.40}$$

Therefore the static polarizability is

$$\alpha^o_{xy} \equiv \frac{\partial \mu_x}{\partial E_y} = \sum_{ik} q_{ik} \frac{\partial r_{ikx}}{\partial E_y} + \sum_i r_{isx} \sum_{jl}\sum_z \frac{\partial q_{is}}{\partial r_{jlz}} \frac{\partial r_{jlz}}{\partial E_y} + \sum_i r_{isx} \frac{\partial q_{is}}{\partial E_y}. \tag{A.41}$$

Consider the force equilibrium condition,

$$q_{jl} dE_y = -df_{jly} = \sum_{ikx} H_{ikx,jly} dr_{ikx}, \tag{A.42}$$

i.e.,

$$\frac{\partial r_{ikx}}{\partial E_y} = \sum_{jl} H^{-1}_{ikx,jly} q_{jl}. \tag{A.43}$$

Plug Eq. (A.43) to Eq. (A.41) and we get Eq. (2.28). If we froze all core coordinates in Eq. (A.41), we can get the static polarizability as Eq. (2.29).